

Tesis Doctoral

# Estudios fundamentales de reacción de electrorreducción de oxígeno en electrolitos no acuosos para el desarrollo de tecnología de batería de Litio-aire

Mozhzhukhina, Nataliia

2017-12-06

Este documento forma parte de la colección de tesis doctorales y de maestría de la Biblioteca Central Dr. Luis Federico Leloir, disponible en [digital.bl.fcen.uba.ar](http://digital.bl.fcen.uba.ar). Su utilización debe ser acompañada por la cita bibliográfica con reconocimiento de la fuente.

This document is part of the doctoral theses collection of the Central Library Dr. Luis Federico Leloir, available in [digital.bl.fcen.uba.ar](http://digital.bl.fcen.uba.ar). It should be used accompanied by the corresponding citation acknowledging the source.

Cita tipo APA:

Mozhzhukhina, Nataliia. (2017-12-06). Estudios fundamentales de reacción de electrorreducción de oxígeno en electrolitos no acuosos para el desarrollo de tecnología de batería de Litio-aire. Facultad de Ciencias Exactas y Naturales. Universidad de Buenos Aires.

Cita tipo Chicago:

Mozhzhukhina, Nataliia. "Estudios fundamentales de reacción de electrorreducción de oxígeno en electrolitos no acuosos para el desarrollo de tecnología de batería de Litio-aire". Facultad de Ciencias Exactas y Naturales. Universidad de Buenos Aires. 2017-12-06.

**EXACTAS** UBA

Facultad de Ciencias Exactas y Naturales



**UBA**

Universidad de Buenos Aires



**Universidad de Buenos Aires**

Facultad de Ciencias Exactas y Naturales

Departamento de Química Inorgánica, Analítica y Química Física

**Estudios fundamentales de reacción de electroreducción de oxígeno en electrolitos no acuosos para el desarrollo de tecnología de batería de Litio-aire**

Tesis presentada para optar por el título de Doctora de la Universidad de Buenos Aires en el área de Química Inorgánica, Química Analítica y Química Física

**Nataliia Mozzhukhina**

Director de tesis: Ernesto J. Calvo.

Consejero de Estudios: Martin Negri.

Lugar de Trabajo: INQUIMAE.

Buenos Aires, 2017.

*As with all such potentially game-changing ideas,  
they begin with over-hyped expectation,  
followed by the inevitable disillusionment,  
and thereafter equilibrium is often established;  
Li–O<sub>2</sub> is now in this third phase”.*

Aurbach, D., B. D. McCloskey, et al. (2016). "Advances in understanding mechanisms underpinning lithium–air batteries." Nature Energy **1**: **16128**.

**Título:** Estudios fundamentales de reacción de electroreducción de oxígeno en electrolitos no acuosos para el desarrollo de tecnología de batería de Litio-aire.

**Resumen.**

En la búsqueda de las baterías de gran densidad energética, la atención mundial fue atraída por las baterías de Li-aire y su potencial de competir con los combustibles fósiles para las aplicaciones automotrices. Esta batería consiste de un ánodo de litio metálico y un cátodo poroso de matriz conductora, donde los iones litio se encuentran con el oxígeno del aire para formar el peróxido de litio. A pesar de las grandes promesas, la batería de Litio-aire posee muchos desafíos por enfrentar para que sea posible su comercialización. Sin embargo uno de los problemas más grandes es la inestabilidad del cátodo y del electrolito, que resulta en una baja retención de ciclos carga-descarga. Para superar esos desafíos fue necesario adquirir una comprensión más profunda de las reacciones que ocurren en el cátodo.

En 2012, cuando inicio esta tesis doctoral, se conocía muy poco sobre la reacción de reducción de oxígeno (ORR) en solventes no acuosos. Pero durante los siguientes cinco años de gran esfuerzo mundial, fue elaborado un modelo más completo de ORR en esos medios.

En este manuscrito reflejaremos nuestra contribución al progreso en la comprensión del mecanismo de ORR y sus implicaciones para el funcionamiento de la batería de Litio-aire. También se discutirá en detalle la importancia de la solvatación del ión litio y el efecto de la solvatación preferencial en los solventes mixtos. Finalmente se explicarán las reacciones de descomposición del solvente con el uso de las técnicas espectroelectroquímicas.

Los estudios realizados son de gran valor para el desarrollo de la tecnología de batería de Litio-aire y han contribuido al estado del arte actual en el campo.

**Palabras claves:** batería de litio-aire; electroreducción de oxígeno; electrolitos no acuosos; superóxido; peróxido de litio; solvatación de ion litio.

**Title:** Fundamental studies of oxygen electroreduction reaction in non-aqueous electrolytes for the development of Lithium-air battery technology.

**Abstract.**

In search of high energy density batteries, the worldwide attention has been captured by Li-air batteries and their potential to compete with fossil fuels for electromotive applications. This battery consists of a Li metal anode and a “breathing” conducting matrix cathode, where the lithium ions combined with oxygen from the air form lithium peroxide. Despite demonstrating great promise, the Li-air battery possesses many challenges that have to be solved in order to make possible its commercialization. One of the biggest problems is the cathode and electrolyte instabilities in the presence of reactive oxygen species, which result in low cycle retention. To overcome those challenges, a more profound understanding of the cathode reactions was required.

In 2012, at the beginning of this doctoral thesis research, very little was known about the oxygen reduction reaction (ORR) in non-aqueous solvents. However during the next five years following enormous research effort worldwide, the comprehensive model of ORR in those media was elaborated.

In this manuscript we will demonstrate our contribution to the progress in the understanding of the ORR mechanism and its implications for the Li-air battery cycling. We will also discuss in great detail the importance of  $\text{Li}^+$  ion solvation and the effect of the preferential solvation in the mixed solvents. Finally we will explain the solvent decomposition reaction with the use of spectroelectrochemical techniques.

The performed studies are of great value for the development of Li-air battery technology, and have contributed to the current state-of-the-art in this field.

**Key words:** lithium-air battery; oxygen electroreduction; non-aqueous electrolytes; superoxide; lithium peroxide; solvation of lithium ion.

# Agradecimientos

En primer lugar, me gustaría agradecer a mi director de tesis Ernesto Julio Calvo por supervisar mi trabajo durante los cinco años y por todo el conocimiento y experiencia compartidos conmigo.

A Martin Negri le agradezco también por su participación como consejero de estudios.

A Federico Williams por las discusiones científicas.

A Lucila Méndez de Leo por enseñarme y colaborar en las medidas de SNIFTIRS, también por su gran ayuda en la escritura de las publicaciones logradas.

A Paula Longinotti y Horacio Corti por enseñarme y colaborar con las medidas de transporte; también por la ayuda en escritura del manuscrito sobre la conductividad.

A los profesores de las materias que he cursado durante esta tesis doctoral: Horacio Corti, Ernesto Calvo, Ernesto Marceca, Roberto Etchenique, Lydia Galagovsky y Miguel Katz.

A Rocío Semino, Gervasio Zaldívar y Daniel Laria por los estudios de dinámica molecular que resultaron ser un buen complemento a las medidas de transporte que hice en colaboración con P. Longinotti y H. Corti.

Agradezco al proyecto FONARSEC por financiar mis primeros años de carrera doctoral y a CONICET por otorgarme una beca doctoral.

Agradezco a la Universidad de Buenos Aires por la formación gratuita y de calidad, y al INQUIMAE por ser mi espacio de desarrollo científico y personal.

A todos los becarios doctorales del grupo de Electroquímica Molecular: Matias Villalba, Florencia Marchini, Walter Torres, Santiago Herrera, Federico Davia y Valeria Romero. A todos los post-docs del grupo de electroquímica molecular: Romain Clarenc, Alvaro Tesio, María del Pozo, Catherine Adam. También extendo mi agradecimiento al resto de los integrantes del grupo de Electroquímica quienes nos han acompañado a lo largo de estos años: Nestor Filieil, Matias Villarreal, Leandro Missoni, Walter Peverini, Franco Ojeda, Daniela Putrino, Matteo Grattieri.

A los compañeros de oficina y de todo el INQUIMAE, Giselle Ferreyroa, Maira Tosato, Andrea Montenegro, Sergio Dabrowski, Cynthia Fernández, Nico García Saggion, Juan Romero, Nahuel Cuba, Matias Lanus, Rocio Torres, Rocio Semino, Gabriela Horwitz, Mariano Ruiz, Leila Saleh, Daniel Wechsler, Nicolas Gonzalez Bardeci, Marcos Orellana, Romina Landa, Federico dos Reis Copello.

A la secretaria por su gran trabajo administrativo: Andrea Atias, Liliana Bayares, Claudia, Cintia, Mariana y por supuesto a Alejandra.

Al tornero Pedro por hacernos el set up experimental y a Leonardo Cantoni por su gran conocimiento en electrónica y su amabilidad en el momento de arreglar nuestros equipos.

Es muy importante también agradecer a los jurados de tesis, tanto titulares, como suplentes: Dr. Doron Aurbach, Dr. Roberto Carlos Salvarezza, Dr. Ezequiel Leiva, Dra. Victoria Flexer y Dr. Fernando Battaglini, por el tiempo que le han dedicado a la lectura y evaluación de esta tesis y por supuesto por la evaluación de la defensa de la tesis.

Además, me gustaría expresar mi sincero agradecimiento al Prof. Doron Aurbach, quien ha viajado en varias oportunidades a Argentina y dio unas charlas muy educativas e inspiradoras.

Por otro lado, quiero decirle muchas gracias a mi familia por estar siempre presente y apoyándome en este gran camino: a mi abuelo Eduard y mi abuela Violeta, a mi papá Dmitriy y a mi mamá Svetlana, mi hermana Olga, mi tía Nataliya y a su pareja John, a mi querida prima Luba, y por supuesto no me puedo olvidar de mi compañero de vida Luis y nuestro pequeño sol Oliver.

# Abbreviations

ACN	Acetonitrile
AN	Acceptor Number
CE	Counter Electrode
CV	Cyclic Voltametry
DEMS	Differential Electrochemical Mass Spectroscopy
DMC	Dimethyl carbonate
DMDMB	2,3-dimethyl-2,3-dimethoxybutane
DME	Dimethoxyethane
DMF	Dimethylformamide
DMSO	Dimethyl sulfoxide
DMSO <sub>2</sub>	Dimethyl sulfone
DN	Donor Number
EC	Ethylene carbonate
EtV	Ethyl viologen ditriflate
EQCM	Electrochemical Quartz Crystal Microbalance
FHFP	Fuoss–Hsia–Fernandez Prini
FTIR	Fourier Transform Infrared Spectroscopy
GC	glassy carbon
GC/MS	Gas Chromatography/Mass Spectroscopy
HC	Hard Carbon
HSAB	Hard Soft Acid Base
IL	Ionic Liquid
IR	Infrared
KF	Karl Fischer
LLTO	Lithiated lithium titanate oxide
LTO	Lithium titanate oxide
NHE	Normal Hydrogen Electrode
NMP	1-Methyl-2-pyrrolidinone

NMR	Nuclear Magnetic Resonance
OCP	Open Circuit Potential
OCV	Open Circuit Voltage
OER	Oxygen Evolution Reaction
ORR	Oxygen Reduction Reaction
PC	Propylene carbonate
PTFE	Polytetrafluoroethylene
PVDF	Poly(vinylidene fluoride)
PYR <sub>14</sub> TFSI	N-butyl-N-methylpyrrolidinium bis(trifluoromethylsulfonyl)imide
RE	Reference Electrode
RRDE	Rotating Ring Disc Electrode
SEI	Solid Electrolyte Interphase
SERS	Surface Enhanced Raman Spectroscopy
SNIRTIRS	Subtractively Normalized Interfacial Fourier Transform Infrared Spectroscopy
SS	Stainless steel
TBA	Tetrabutylammonium
TDPA	Tris(4-(diethylamino)phenyl)amine
TEA	Tetraethylammonium
TEGDME	Tetraethylene glycol dimethyl ether
TEMPO	2,2,6,6-tetramethylpiperidinyloxy
TTF	Tetrathiafulvalene
UME	Ultramicroelectrode
WE	Working Electrode
XPS	X-ray Photoelectron Spectroscopy
XRD	X-ray Diffraction

# Content

## Chapter 1. Introduction.

1.1. Motivation.....	12
1.2. The world's energy demand and environmental concerns: necessity for new energy storage and conversion devices.....	13
1.3. Batteries: from Galvani-Volta dispute to modern day Li-ion powered electronics and future Li-air run electric vehicles.....	15
1.4. Li-air battery fundamentals and history: from discovery to present promises and challenges.....	18
1.5. Scope of thesis.....	27
1.6. Resumen en castellano del capítulo 1. Introducción.....	29

## Chapter 2. Experimental details.

2.1. Chemicals and solutions.....	31
2.2. MBraun glove box use and maintenance.....	33
2.3. Karl Fisher water determination.....	35
2.4. On the reference electrode in Li-air studies.....	37
2.5. Electrochemical experiments.....	41
2.6. Infrared experiments.....	44
2.7. Differential electrochemical mass spectrometry (DEMS).....	46
2.8. Viscosity and conductivity measurements in organic solvents.....	47
2.9. Electrochemical quartz crystal microbalance (EQCM).....	50
2.10. Resumen en castellano del capítulo 2. Detalles experimentales.....	55

## Chapter 3. Li-air battery prototype testing: the visualization of the problem.

3.1. Introduction.....	56
3.2. Substitution of Li metal anode and Li-air battery charge-discharge experiments.....	58
3.3. Conclusions.....	63

3.4. Resumen en castellano del capítulo 3. Pruebas del prototipo de batería de Litio-aire: visualización del problema.....	64
--	----

**Chapter 4. Cathode reaction: mechanistic insights into the oxygen electroreduction and evolution reactions.**

4.1. Introduction.....	66
4.2. ORR in non aqueous organic solvents without Li <sup>+</sup> .....	67
4.3. ORR and OER in non aqueous organic solvents in the presence of Li <sup>+</sup> .....	72
4.4. Lithium ion concentration effect in PYR <sub>14</sub> TFSI ionic liquid for Li-O <sub>2</sub> battery cathodes. ....	80
4.5. Surface versus solution mechanism: new understanding of ORR. ....	88
4.6. Conclusions.....	90
4.7. Resumen en castellano del capítulo 4. Reacción de cátodo: detalles del mecanismo de electroreducción y evolución de oxígeno.....	92

**Chapter 5. The exploration of mixed electrolyte systems for the Li-air battery and the effect of Li<sup>+</sup> solvation.**

5.1. Introduction. ....	94
5.2. The RRDE evidence of Li <sup>+</sup> preferential solvation.....	95
5.3. Redox potential of the Li/Li <sup>+</sup> electrode in different media.....	98
5.4. A conductivity study of preferential solvation of lithium ion in acetonitrile-dimethyl sulfoxide mixtures.....	103
5.5. Microelectrode study of oxygen diffusivity and solubility in mixed solvents.....	111
5.6. Conclusions.....	122
5.7. Resumen en castellano del capítulo 5. La exploración	

de los sistemas de electrolitos mixtos para la batería de Litio-aire y el efecto de la solvatación del ion $\text{Li}^+$ .....	123
---	-----

**Chapter 6. Investigation of the solvent's instability in the Li-air battery.**

6.1. Introduction.....	125
6.2. Infrared spectroscopy studies on the stability of dimethyl sulfoxide for application in a Li-air battery.....	127
6.3. In situ Infrared spectroscopy study of $\text{PYR}_{14}\text{TFSI}$ ionic liquid stability for Li- $\text{O}_2$ battery.....	141
6.4 Conclusions.....	150
6.5. Resumen en castellano del capítulo 6. Estudios de la inestabilidad del solvente en la batería de Litio-aire. ....	152

**Chapter 7. Conclusions and final remarks.**

7.1. Thesis summary and conclusions. ....	154
7.2. Future work.....	158
7.3. Conclusiones de la tesis en castellano.....	159

<b>List of publications.....</b>	<b>162</b>
----------------------------------	------------

<b>References.....</b>	<b>163</b>
------------------------	------------

# Chapter 1. Introduction

## 1.1. Motivation.

Energy storage is one of the greatest challenges of the 21st century, and worldwide attention is captured by Li-based batteries technologies and their potential role for transport electrification. Li-ion batteries have proven to be an efficient solution for the portable electronic devices. However, their energy density is too low for application in electric vehicles, and the current challenge for scientific society is to go beyond the Li-ion by developing new battery technologies possessing higher energy densities that could compete and replace the internal combustion engine.

Rechargeable Li-air is a new and upcoming battery chemistry that uses lithium metal as an anode material and reduces oxygen from the air at the cathode during discharge. It is a promising candidate to meet the energy challenge because of its high theoretical gravimetric energy density. However in practice, Li-air batteries have a variety of drawbacks that have prevented them from commercial use, together with the lack of understanding of the fundamental chemistry behind it. The main problems with Li-air batteries are high overpotential for charge reaction, parasitic reactions with air components such as water and carbon dioxide, dendrite growth on the lithium anode, temperature dependence, low cycle retention, limited operational current densities, occlusion of catalyst and active material during discharge due to accumulation of insoluble  $\text{Li}_2\text{O}_2$ , and the most challenging, electrolyte and cathode material instabilities towards reduced oxygen species. Along with the solving of technical problems, a deeper understanding of the basic Li-air battery electrochemistry is essential, such as the mechanisms of Oxygen Reduction Reaction (ORR) during discharge and Oxygen Evolution Reaction (OER) during charge.

The Li-air battery is a field in a very nascent stage, with very fast evolving picture, plenty of unsolved issues and several uncertainties on the battery chemistry. Numerous reviews have been published in recent years reflecting a rapidly evolving picture of promises and challenges facing Li-air battery (1-15).

## **1.2. The world's energy demand and environmental concerns: necessity for new energy storage and conversion devices.**

In the last century our world has experienced an enormous population growth. The world population reached the 1 billion milestone for the first time in human history in 1804, in a little more than a century later this number doubled and reached 2 billion in 1927. In the XXI century rapid growth of the world's population has risen to 7 billion habitants, with further growth predicted in the future (17, 18).

Total world primary energy consumption has also grown and according to the BP statistical review of world energy in June 2016, the world energy consumption (including coal, renewable, hydroelectricity, nuclear energy, natural gas and oil) has grown from around 8,000 in 1990 to more than 13,000 million tons of oil equivalent in 2015. In 2014 the total energy supply was comprised of 31% oil, 29% coal, 21% natural gas, 10% biofuels, 5% nuclear, 2% hydro and 2% other. Therefore, fossil fuel accounted for 81% of the total world energy supply. Thus it is clear that world energy supply is based on no renewable sources and while our planet's population and energy consumption grow, its dimensions and resources remain the same. This inevitably results in ecological problems and resource depletion. This makes clear the assertion that energy storage and conversion are some of the great challenge of the 21st century.

According to NASA, 97% of climate scientists agree that climate warming trends over the last century are very likely caused by human activities. An increase in human-produced greenhouse gases such as carbon dioxide, methane and nitrous oxide, are related to the increased "green house effect" is believed to be main cause of the increased global temperatures. According to the data extracted from atmospheric samples contained in ice core, carbon dioxide levels over the last 400 000 years have never been above 280 ppm, however it reached 400 ppm currently. This rise in CO<sub>2</sub> level is believed to be caused by the increased burning of fossil fuel by humans since the beginning of the Industrial Revolution. Considering this widely accepted human-produced climate change, new climate policies advocate for the reducing of greenhouse emissions and a shift to renewable energies from fossil fuels.

According to the International Energy Agency, in 2014 the total final energy consumption by sector was distributed as follows: industry 37%, transport 28%, residential 23%, commerce and

public services 8%, agriculture/forestry 2% and other 2%. Taking into consideration that transportation accounts for almost a third of world energy consumption, the creation of new technologies, such as electric vehicles driven on batteries, is of paramount importance.

While the development of more efficient and cost-effective renewable energy conversion technology is absolutely necessary (solar panels, wind turbines, hydroelectric plants, solar thermal plants, geothermal power stations etc.), their major inconvenience is that they fluctuate independently from demand. Therefore the importance of energy storage devices should not be overlooked. Efficient energy storage management should allow storing the produced energy during low demand and its release during high demand (so called “peak shaving”), coping with supply-demand imbalance and the avoidance of energy waste. Some of the widely used energy storage systems today are: batteries (conventional batteries or flow batteries), fuel cells, flywheels, compressed air, thermal and pumped hydro-power(23).

To conclude, in light of the short supply and negative ecological implications of using fossil fuels, the development of renewable and alternative energy storage and conversion technologies is absolutely essential. Batteries are a reliable and highly versatile energy storage technology which can be used to store the energy generated by renewable sources or to drive an electric vehicle.

### **1.3. Batteries: from Galvani-Volta dispute to modern day Li-ion powered electronics and future Li-air run electric vehicles.**

The history of electrochemistry and creation of first battery goes back to Italy in the end of XVIII – beginning of the XIX centuries. It all has started when Italian scientist Luigi Galvani in 1781 touched with iron scalpel a dissected frog attached to brass hooks and saw that frog's legs started to contract. However he wrongly attributed those dead animal movements to “animal electricity”. Another Italian scientist, Alessandro Volta in 1800 to dismiss his theory created a first battery in the world, formed by an alternating sequence of zinc and copper or silver disks separated by a cloth soaked in a salt solution, which is now known as voltaic pile and was the progenitor of modern batteries. He claimed that frog's contractions discovered by Galvani, indeed were the result of a current flowing between two different metals (brass and iron) connected by moist flesh of a frog's leg(25).

Shortly after that in 1802 a German scientist Johann Wilhelm Ritter built the first dry cell battery that consisted of 50 copper discs separated by cardboard disks moistened with a salt solution. In 1829 a French scientist Antoine Becquerel developed the Constant Current Cell; however only few years later the English chemist John Daniell developed an almost identical cell, but unfortunately Becquerel did not receive any recognition in England during his life time. Daniell cell consisted of copper in copper sulfate solution and zinc in sulfuric acid. At nearly the same time another English scientist William Robert Grove developed the nitric cell consisting of zinc in dilute sulfuric acid and platinum in concentrated nitric acid. It happened that Daniell's and Grove's research on the constant current cells coincided with the development of commercial telegraph systems in late 1830's. Early American telegraph had used first Grove's cell, however it had a big disadvantage, i.e. evolution of toxic nitric dioxide gas during operation, and therefore was later replaced by the Daniell cell .

In the same XIX century some of today's widely spread batteries were discovered. For example, the lead-acid battery, commonly used for an ignition of a car combustion engine, was invented in 1859 by the French scientist Gaston Planté (almost 30 years before the discovery of the electron as the elementary negative particle in 1897 by J.J. Thomson). And another broadly exploited battery, the so called Leclanché cell, based on zinc and manganese oxide, was invented in 1866 by the French engineer Georges-Lionel Leclanché. It is quite notable that those highly functional

cells were created before the electron was discovered and reaction mechanism could be understood. Also the Nickel-Cadmium rechargeable battery was invented in 1901 by the Swedish engineer Waldmar Jungner(25).

Then it was not until the 1970, than a new demand for portable energy (consumer electronics and implantable medical devices) again shaped the battery research, mostly in lithium and hydride-based rechargeable batteries. While initial research was focused on the lithium metal anode, in the late 1970's, the new idea of using two lithium intercalation compounds for both electrodes resulted in the concept of the "lithium rocking chair battery". Almost two decades of research in possible rechargeable batteries finally lead to the first practical applications: the Nickel-metal hydride battery was commercialized in 1989, and two years after a Li-ion battery was introduced by Sony. This battery would revolutionize the consumer electronic market and our way of life.

However, in XXI century our society faces a new demand: the replacement of the polluting internal combustion cars with battery-driven electric vehicles. Electric vehicles that are able to function exclusively on batteries could be a promising solution for the energy crisis in terms of oil depletion and environmental concerns. However current commercial Li-ion batteries only reach a gravimetric energy density of 160 Wh/kg, and even if their characteristics could be improved, the energy density of today's Li-ion batteries is limited to a theoretical value of 387 Wh/kg. Those values are efficient enough for the Li-ion to be used in portable electronics, but are too low for application in the electric vehicles.

Recently the scientific community's great interest was attracted by a Li-air battery with high theoretical energy density that is comparable to the theoretical energy density of gasoline and one order of magnitude higher than that of Li-ion batteries.

Metal-air batteries are a very attractive technology; they are generally cheaper than other types of batteries and have a common unique feature: they use oxygen from air at the positive electrode (cathode). With lithium being the lightest metal in the world, the Li-air batteries possess the highest energy density of most metal-air batteries. In the table 1.1, theoretical energy densities and voltages of different metal-air batteries are shown. Values of theoretical specific capacity for Li-O<sub>2</sub> couple vary in literature, depending on whether Li<sub>2</sub>O<sub>2</sub> or Li<sub>2</sub>O is taken a final product, and also depending on whether specific capacity calculated per kg of Li or corresponding lithium

oxidation product (oxide or peroxide). All those possible results are depicted in the table 1.1, however it is worth noticing that major discharge product of Li-air is lithium peroxide, while no lithium oxide is normally detected. On the other hand, if ideal reaction  $\text{Li} + \text{O}_2 = \text{Li}_2\text{O}_2$  occurs; oxygen should be included to the calculation, that would correspond to the specific capacity of battery after discharge. Considering all factors mentioned above, it is most appropriate to use the value of 3390 Wh/kg as a theoretical specific capacity of Li-air battery, which is still much higher than that of majority of other metal-air batteries.

**Table 1.1. Characteristics of the common metal-air batteries.**

<b>Metal-air battery</b>	<b>Calculated OCV (V)</b>	<b>Theoretical specific capacity Wh/kg (including O<sub>2</sub>)</b>	<b>Theoretical specific capacity Wh/kg (NOT including O<sub>2</sub>)</b>
<b>Li-O<sub>2</sub> (Li<sub>2</sub>O as final product)</b>	2.91	5200	11150
<b>Li-O<sub>2</sub> (Li<sub>2</sub>O<sub>2</sub> as final product)</b>	2.96	3390	11150
<b>Al-O<sub>2</sub></b>	2.73	4300	8130
<b>Na-O<sub>2</sub></b>	1.94	1677	2260
<b>Ca-O<sub>2</sub></b>	3.12	2990	4180
<b>Mg-O<sub>2</sub></b>	2.93	2789	6462
<b>Zn-O<sub>2</sub></b>	1.65	1090	1350

#### **1.4. Li-air battery fundamentals and history: from discovery to the present promises and challenges.**

**Definition and terminology.** It is important to mention that very few studies have focused on real “lithium-air” battery and have used AIR as an active cathode material (26-28), while in most of the work published, pure oxygen and not the air was used. Therefore it is technically more correct to refer to “lithium-oxygen” and not “lithium-air” battery, however both of these names are found in the literature. It became very common among scientists to use terminology “lithium-air”, even if pure oxygen is used and therefore in this thesis the “lithium-air” will be used as a commonly employed terminology.

Four different kinds of architecture for Li-air batteries have been reported, they include three types of cells with liquid electrolyte: aprotic using organic solvents and ionic liquids (the majority of published work), aqueous (29) and mixed aqueous-protic (30) and all solid-state battery with solid electrolyte (31-33). The main difference between Li-air cells based on aqueous and aprotic electrolytes is in electrochemistry of reaction occurring on the cathode (formation of  $\text{Li}_2\text{O}_2$  in aprotic and solid electrolytes and  $\text{LiOH}$  in aqueous electrolytes), while anode reaction remains the same (dissolution of Li metal). But in aqueous solution the anode must be protected by a lithium ion conducting membrane.

All solid-state battery with polymer based electrolyte supposedly has the same battery chemistry as a non-aqueous lithium air battery with electrolyte based on the organic solvents.

The most effort has been put to investigate a non-aqueous Li-air cell based on liquid aprotic electrolyte, mostly organic solvents: carbonates, ethers, DMSO etc. This research preference occurred due to the belief that this cell configuration was the only reversible one.

The non-aqueous lithium air battery consists of lithium metal anode, electrolyte ( $\text{Li}^+$  salts dissolved in organic solvents, ionic liquids or solid state polymer electrolytes), and air cathode where ORR and OER take place at discharge and charge cycles respectively. The air cathode is a challenging part of the Li-air cell that is shown to directly limit the possible discharge capacity. Typically, the air cathode in Li-air battery consists of: electron conductor (conductive carbon, Au, TiC etc. with pores for the  $\text{O}_2$  diffusion and  $\text{Li}_2\text{O}_2$  deposition), sometimes catalyst (transition metals or metal oxides) that is believed to catalyze  $\text{Li}_2\text{O}_2$  formation and decomposition reactions;

and optionally a binder (e.g. PVDF).. The schematic representation of non-aqueous Li-air cell is shown on the figure 1.1.

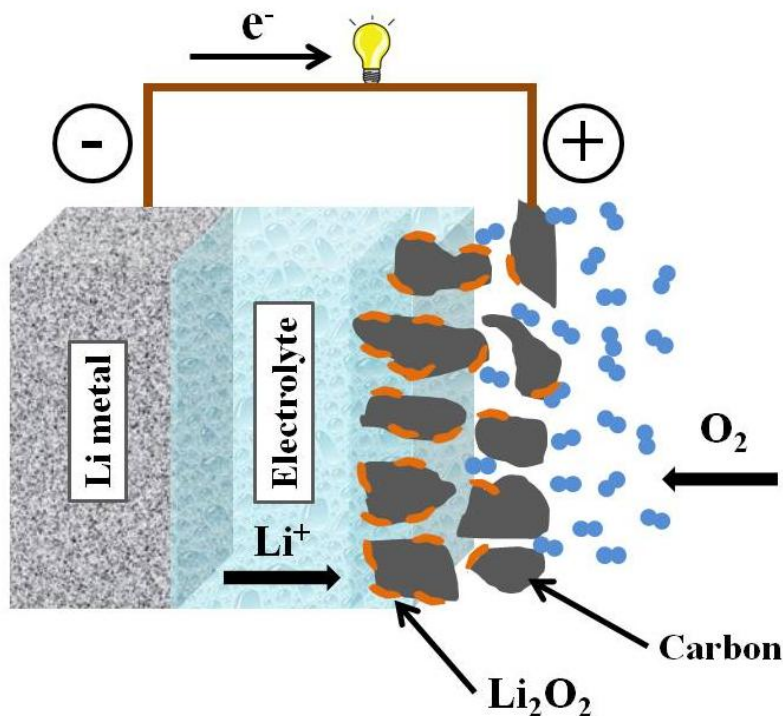


**Figure 1.1. Schematic representation of aprotic Li-air battery (discharge process).**

The reaction occurring at the anode during discharge is dissolution of lithium metal:



And formation of lithium peroxide with the oxygen from atmosphere at the cathode:



With the following overall reaction:



$\text{Li}_2\text{O}_2$  (not  $\text{LiO}_2$  or  $\text{Li}_2\text{O}$ ) was found to be the main discharge product of the non-aqueous Li-air cells. This has been confirmed by various techniques:

- Qualitative analysis based on the reaction  $\text{MnO}_4^- + \text{H}_2\text{O}_2 \rightarrow \text{O}_2 + \text{MnO}_2$  in neutral solution (31)
- Raman spectrometry (31, 34)
- XRD (34-36)
- FTIR and SERS (36)

In the case of operation of Li-air battery in ambient air, other discharge products, namely LiOH and  $\text{Li}_2\text{CO}_3$  are possible, due to the reaction with  $\text{H}_2\text{O}$  and  $\text{CO}_2$  (27, 28).

**Discovery and early research on Li-air.** The rechargeable non-aqueous Li-air battery was reported in 1996 by Abraham and Jiang (31). Abraham later indicated that he did not intend to invent rechargeable Li-air, but that a discovery has been serendipitous(37). He and his team were investigating the electrochemical properties of a Li/graphite cell with the polymer electrolyte based on polyacrylonitrile, ethylene and propylene carbonates and  $\text{LiPF}_6$ . They performed in situ IR analysis on the cell to analyze gases produced at different stages of discharge, using a gas syringe to withdraw gases from the plastic-sealed Li/C cell. After this manipulation the author saw that the cell open circuit potential (OCP) always increased to 2,5 V and delivered small capacity at 2,3 V. The only conclusion was that they accidentally were introducing small amounts of oxygen into the cell. Realizing the importance of this accidental result, Abraham built a Li-air battery which found to be rechargeable. He found that the main discharge product of the cell without a catalyst was  $\text{Li}_2\text{O}_2$  and that in the presence of the transition metal catalyst oxygen reduction can proceed to  $\text{Li}_2\text{O}$ . They used cobalt as a catalyst and suggested that the catalyst is necessary to lower the recharge overvoltage and increase the coulombic efficiency of the Li-air battery.

For the next 10 years that followed Abraham's discovery, there has been quite a modest interest in Li-air battery technology. Read had investigated different electrolyte and cathode formulations and its implications on discharge capacity (38-40). Worth mentioning here is that all the early work on Li-air battery was mainly performed by scientists coming from Li-ion battery field, and therefore they started to use the same electrolytes as in Li-ion technology, such as alkyl carbonates: EC, PC and DMC. However no research was done to evaluate the suitability of those electrolytes in new system and it took more than a decade to discover their instability.

In 2006, Bruce demonstrated by in situ mass spectrometry that  $\text{Li}_2\text{O}_2$  formed on discharge could be decomposed to Li and  $\text{O}_2$  on the recharge, thus proving the rechargeability of Li-air battery, either with or without a catalyst(35). They stated that battery charging did not involve electrolyte decomposition. Several years later it was demonstrated that this statement was wrong and the electrolyte decomposition does occur, but back in 2006 the evidence of rechargeable  $\text{Li}_2\text{O}_2$  cathode had sparked an enormous interest in scientific community and starting from 2006, there has been an increasing number of publications each year on Li-air battery. The results obtained from Scopus network by searching “Li- $\text{O}_2$  or Li-air” in article title, abstract and keywords, are presented on the figure 1.2.

Works published in between 2006 and 2010 were mainly focused on obtaining large discharge capacity, sometimes only for the first discharge, by varying operation conditions(26), cathode architecture (33, 41, 42), catalyst(43, 44), electrolyte(45), electrolyte-filling status and discharge current density(46) etc., using frequently the same electrolytes that proved to work for Li-ion battery. High capacities were reached, however cycle ability of such batteries appeared to be really poor due to electrolyte instability. It was shown later that organic carbonates are unfit to be used in Li-air battery.

In 2009 many companies and research institutions became interested in the Li-air battery for automotive applications, among them IBM launched an ambitious Battery 500 Project, aiming to developing improved Li-air battery to power electric vehicles with a driving range of 500 miles per charge. The increased interest in this new technology resulted in even higher number of scientific publications in 2010-2012 (see figure 1.2), and a first review on Li-air battery was published in 2010 (6). After deeper insight into the Li-air battery chemistry it became clear that more fundamental studies on the ORR and OER were needed and that analytical tools had to be coupled to the battery charge-discharge experiments; and in turn that brought even more research groups in the field, leading to ever growing number of publications.

It is appropriate to cite here a review paper published in 2016, that states: “As with all such potentially game-changing ideas, they begin with over-hyped expectation, followed by the inevitable disillusionment, and thereafter equilibrium is often established; Li- $\text{O}_2$  is now in this third phase”.(13)

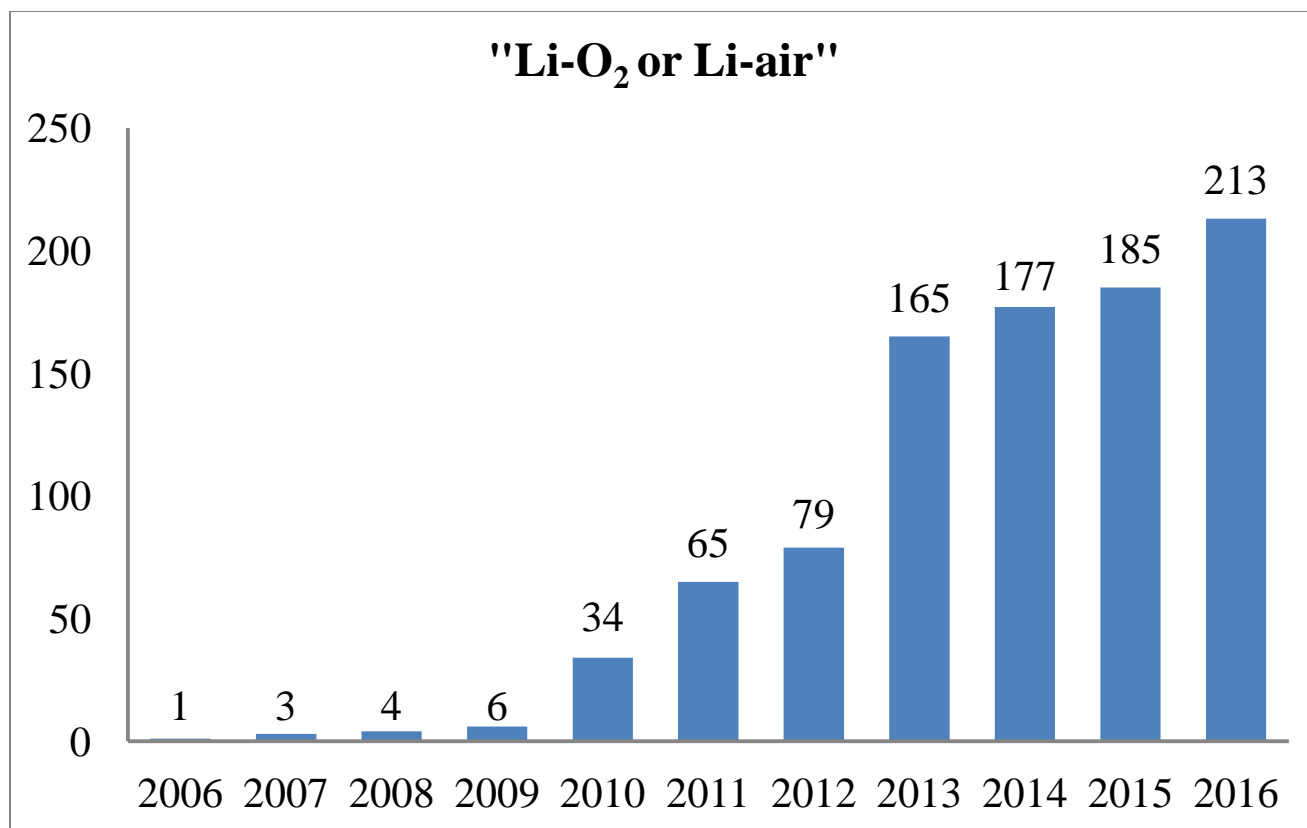


**Figure 1.2. Number of publications including “Li-O<sub>2</sub> or Li-air” in article title, abstract and keywords, between 2006 and 2016.**

**Electrolytes for Li-air battery.** In 2011, McCloskey et al. reported that organic carbonates, widely used as electrolyte for Li-air battery until that year, undergo decomposition to form Li<sub>2</sub>CO<sub>3</sub>, Li alkyl carbonates, while small amount of Li<sub>2</sub>O<sub>2</sub> was observed(34). It was then proved that organic carbonates, such as ethylene carbonate and propylene carbonate undergo decomposition during Li-air battery discharge, with decomposition products being the main discharge product: C<sub>3</sub>H<sub>6</sub>(OCO<sub>2</sub>Li)<sub>2</sub>, Li<sub>2</sub>CO<sub>3</sub>, HCO<sub>2</sub>Li, CH<sub>3</sub>CO<sub>2</sub>Li, CO<sub>2</sub>, H<sub>2</sub>O; while only very little or no Li<sub>2</sub>O<sub>2</sub> was formed (47). McCloskey et al. (34) have shown that during discharge, the number of electrons per O<sub>2</sub> molecule in organic carbonates is more than 2 (meaning that other than Li<sub>2</sub>O<sub>2</sub> formation discharge reaction takes place) and also mass spectrometry has shown that during charging CO<sub>2</sub> evolves rather than O<sub>2</sub>. Organic ethers such as DME and TEGDME(48) were then proposed to be more efficient and stable solvents for Li-air batteries. In DME-based electrolyte, discharge reaction involves 2.05±0.05 e/O<sub>2</sub>; however charging involves 3.2 e/O<sub>2</sub>, and that suggests that organic ethers are stable only during the first discharge. Although DME also

tends to decompose during charge and with an increase of cycle number, the main discharge product during testing Li-air cathodes was found to be  $\text{Li}_2\text{O}_2$  at least for the first discharge.

One study (49) presented a comparison of stability different types of electrolytes including: carbonate, glymes, sulfoxide, phosphate, nitrile and ionic liquid. The stability of electrolytes was evaluated with spectroscopic studies of discharged products by XRD, XPS and GC/MS. The study concludes that in all of the electrolytes  $\text{Li}_2\text{CO}_3$  is formed due to electrolyte decomposition; however glymes result in higher formation of  $\text{Li}_2\text{O}_2$  than other electrolytes.

The electrolyte stability was further recognized to be one of the major challenges, and the research interest shifted to the search for stable electrolytes and various solvents were tested in the Li-air cells. Several lessons were learned at that time, and the most important conclusion was that when using a new solvent in a new system, ORR and OER products had to be carefully identified by analytical techniques.

In 2012 appeared two reports about cells capable to perform up to 100 cycles with a high capacity retention : in DMSO (36) and TEGDME (50). However, very soon it was recognized that TEGDME, while being more stable than previously used carbonates, undergoes parasitic reactions and is not compatible for the use in the Li-air battery(51), however some controversy on the stability of organic ethers still remains. A promising approach for electrolyte design was reported by Adams et al., by substitution of the backbone protons on DME with methyl ( $-\text{CH}_3$ ) groups, which resulted in higher stability of synthesized 2,3-dimethyl-2,3-dimethoxybutane (DMDMB)(52).

Dimethyl sulfoxide (DMSO) has been suggested as a possible stable electrolyte due to the increased stability of the superoxide anion in this solvent (53); Li-air battery testing utilizing DMSO as a solvent have also shown an improved performance (36, 49). However, several studies later have questioned the stability of DMSO, reporting side products such as  $\text{LiOH}$ (54-56), dimethyl sulfone (54, 55, 57),  $\text{Li}_2\text{SO}_3$  (54, 56) and  $\text{Li}_2\text{SO}_4$  (54). While DMSO might not be a stable solvent, it does possess unique properties, such as stabilization of superoxide anion (53, 58, 59) and therefore is very interesting solvent from a fundamental point of view (in more details discussed in the chapter 4).

Ionic liquids (ILs) are organic salts that are liquid at room temperature and exhibit a set of unique properties: non volatility, high oxygen solubility, non flammability and high stability that make them promising candidates as electrolyte for metal-air, and particularly Li-air batteries (60, 61). One of the most available and widely investigated ILs for lithium batteries is N-butyl-N-methylpyrrolidinium bis(trifluoromethylsulfonyl)imide (possible abbreviations for the cation are: BMP<sup>+</sup>, C<sub>4</sub>mpyr<sup>+</sup>, PYR<sub>14</sub><sup>+</sup>, Pyr<sub>14</sub><sup>+</sup> and for the anion are: TFSI<sup>-</sup>, [NTf<sub>2</sub>]<sup>-</sup> or [N(SO<sub>2</sub>CF<sub>3</sub>)<sub>2</sub>]<sup>-</sup>). In this thesis we will use PYR<sub>14</sub>TFSI abbreviation.

Highly polar amide-based solvents were also proposed as candidates for electrolytes in Li-O<sub>2</sub> system(62-64). The main disadvantage of the amides is their high reactivity with metallic lithium, however Walker et al.(65) have reported that adding the LiNO<sub>3</sub> salt to the N,N-Dimethylacetamide stabilized the SEI on the lithium anode resulting in successful Li-O<sub>2</sub> cycling.

In 2013 Zhan and Zhou proposed a Li-air cell, replacing liquid electrolyte by solid Li-ion conductor and solid air cathode by gel cathode(27). The proposed battery sustained repeated cycling in ambient air for 100 cycles (78 days), with discharge capacity of 2,000mAhg<sup>-1</sup>. Interestingly, the recharging was based on Li<sub>2</sub>CO<sub>3</sub> that originates from Li<sub>2</sub>O<sub>2</sub> by reacting with CO<sub>2</sub> from ambient air.

**Cathode material and catalysts for Li-air battery.** Porous carbons (super P, Ketjen black, activated carbon, Vulcan XC-72 etc) with or without catalyst are used normally as cathode materials. However it has been shown that carbon cathodes as well as electrolytes can undergo decomposition in the presence of reactive reduced oxygen species (66, 67). Several other materials were explored as possible cathodes for Li-air batteries, and those include functional carbon materials (grapheme, mesoporous carbon, carbon nanotubes, carbon nanofibers and microfibers), N-doped carbon materials, etc. Metals and metal oxides were proposed either as a cathode material and/or catalyst; those include Au, Pt, Pd, Ir, manganese oxides, transitional metals and their oxides and perovskites. The employment of all those different cathode materials has been systematically analyzed and published in a review on cathode materials and structures by Zhong Ma et al.(68)

At the same time as the instabilities of most commonly used electrolytes have been discovered, doubts about efficiency of the catalyst surged. In 2011 McCloskey et al. suggested that catalyst

might be unnecessary and that in the studies done before, the catalyzed reaction with Au, Pt and MnO<sub>2</sub> was electrolyte decomposition in place of OER (69). Currently, the necessity of catalysts for reducing recharge overpotential still remains a debate in the Li-air field.

**Lithium anode.** While most of the research effort has been focused on the cathode reaction, the use of lithium metal anode still remains a challenge and poses high safety risks.

The lithium metal due to its highly reducing nature decomposes almost all known electrolytes. Some of the electrolytes (alkyl carbonates and ethers for example) form a stable film from decomposition products on the lithium surface. This film known as Solid Electrolyte Interface (SEI) is an electron insulator but it conducts Li ions. Those two qualities of SEI are of great importance and lay behind the successful functioning of the Li-ion batteries! It is widely recognized that a formation of SEI is essential for successful battery charge-discharge process, however still not all of the proposed and studied electrolyte systems can form stable SEI on lithium metal. For example, DMSO does not form stable SEI on lithium metal, and Bruce groups has used PC to protect the lithium metals prior cycling in DMSO-based electrolyte(36). Another promising approach is the use of LiNO<sub>3</sub> salt that was shown to form stable protective SEI layers on lithium anode in otherwise not stable solvents (70, 71).

The growth of dendrites on the recharge is another issue presenting safety hazard due to a possibility of short cuts.

The other possibility, widely considered by several investigators, is a replacement of lithium metal anode by other lithium ion containing material (such as LTO or lithiated hard carbons for example), however this would inevitably reduce the battery capacity.

**Additives and Impurities.** As it has been mentioned before, the majority of studies performed in Li-air battery used pure oxygen, rather than air. However if a Li-air battery is to be used with ambient air, introduction of the impurities to the cell is inevitable. These impurities, such as CO<sub>2</sub> and H<sub>2</sub>O can have a dramatic effect on the performance of Li-air battery (27, 28) . Water is an important source of protons that can readily react with oxygen reduced species that in turn accelerates degradation of electrolytes. However the addition of water can have a positive effect as well, such as increased discharge capacity(72). This effect has not been understood well at first, however later it was explained by increased solvation of superoxide anions by water

molecules and consequent formation of larger toroidal  $\text{Li}_2\text{O}_2$  particles, in comparison to thin  $\text{Li}_2\text{O}_2$  film in water-free cell (73).

An addition of redox mediator is a very promising way to improve cycling in Li- $\text{O}_2$  system (74-76). A redox mediator is an electroactive molecule that is oxidized at potential slightly above the equilibrium potential of lithium peroxide formation and can help to dissolve the solid discharge products. In the case of formation of large lithium peroxide toroids, the use of redox mediators seems the most efficient way for dissolving discharge products. Among the various redox mediators explored for Li-air battery there are TTF tetrathiafulvalene (75, 77, 78), TDPA tris(4-(diethylamino)phenyl)amine (79), TEMPO (2,2,6,6-tetramethylpiperidinyloxy) (80), LiI (81) and CsI (82), EtV ethyl viologen ditriflate (76), dimethylphenazine (83). However, as in the case with all the cell elements, more studies are necessary to find stable and efficient redox mediator.

However it is worth to mention that the importance and potential of Li-air battery technology was too optimistic in the beginning of the research. Even in the case that side reactions are fully mitigated, there will be issues of capacity limitations, use of air instead of oxygen, lower volumetric energy density that what would be anticipated, etc.

## 1.5. Scope of thesis

This thesis entitled: “Fundamental studies of oxygen electroreduction reaction in non-aqueous electrolytes for the development of Lithium-air battery technology” provides important fundamental insights into the cathode reactions occurring in the Li-air battery. The thesis consists of seven chapters.

In the chapter 1 the extensive introduction into the field is provided. The motivation behind the research, based on current world energy demand together with the statistics of energy sources and their impact on the environment, is given. The introduction chapter also includes brief history of the batteries with a special emphasis on metal-air batteries and Li-air battery. Then the history and principles of Li-air battery are given in much details in 1.4, highlighting the numerous challenges facing the technology.

Chapter 2 has aim to provide the reader with the detailed description of all the experimental procedures used during the PhD training, including the manipulation and storage of chemicals, special care with air and moisture sensitive chemicals description of the electrochemical cells and the equipment.

Finally in chapter 3 to 6, the experimental results and corresponding detailed discussions are given.

In chapter 3 we present Li-air battery prototype charge-discharge testing experiments employing the ionic liquid as an electrolyte system, with the emphasis on the battery’s fading performance. Therefore, this chapter contains the evidence for the need of further fundamental electrochemical studies of the Li-air system in order to explain the observed phenomena. Consequently, chapter 4 gives deep insight on the mechanism of ORR and OER based on the literature and the research conducted in our group and includes the experimental work performed with the use on organic solvents (DMSO and ACN) as electrolyte system, the relevant results to the use of ionic liquid as well.. Then, in the chapter 5 the mixed systems ACN-DMSO are discussed highlighting the preferential solvation of the  $\text{Li}^+$  cation. Chapter 6 deals with the decomposition reactions and provides the spectroelectrochemical studies on the instabilities of DMSO and ionic liquid  $\text{PYR}_{14}\text{TFSI}$ .

The chapter 7 is the conclusion and summaries section that gives the reader the relevant conclusions on all the research performed, as well as reflection on the future of Li-air battery system and its feasibility.

## 1.6. Resumen en castellano del capítulo 1. Introducción.

Durante el último siglo la población mundial y su demanda energética han crecido considerablemente. La mayor parte de esta energía proviene de combustibles fósiles y esto conlleva a varios problemas socio-ambientales, tales como el calentamiento global, el agotamiento de los recursos naturales y la contaminación del medio ambiente. Es por ello que resulta imperioso desarrollar nuevas tecnologías que empleen las energías renovables e implementar y estudiar nuevos métodos de almacenamiento de estas energías. Las baterías recargables de litio podrían servir a este propósito, tanto para almacenamiento de dicho tipo de energía, proveniente del sol o del viento, como también para ser usadas como reemplazo a los actuales motores de combustión interna en los automóviles.

Las baterías de ion-litio que están siendo empleadas prácticamente en toda la electrónica portátil han revolucionado nuestras vidas, pero su densidad energética no es suficiente para su uso en los vehículos eléctricos. Es por eso, que durante la última década la atención mundial se ha centrado en las baterías de Litio-aire, las cuales poseen una alta densidad energética teórica y de desarrollarse plenamente podrían llegar a competir con los combustibles fósiles. Pero existen muchísimos obstáculos que deberían solucionarse para su posible comercialización, tales como la baja retención de carga-descarga, bajas corrientes de funcionamiento, problemas relacionadas con el empleo de litio metálico el cual es muy reactivo, inestabilidad tanto del material de cátodo como el electrolito en presencia de las especies reactivas de oxígeno reducido, etc. Por eso, los estudios fundamentales de los mecanismos de las reacciones fisicoquímicas que ocurren en estas baterías son esenciales para poder superar dichos desafíos.

La batería no acuosa de litio-aire fue introducida en 1996 por Abraham (31) consistía de un ánodo de litio metálico y un cátodo poroso (carbón, oro, etc.) con o sin un catalizador, y un electrolito no acuoso. En el cátodo, el oxígeno del aire se reduce para formar peróxido de litio  $\text{Li}_2\text{O}_2$ . Durante la recarga de la batería ocurre la descomposición del peróxido de litio a iones  $\text{Li}^+$  y oxígeno acompañada por un alto sobrepotencial.

En los primeros diez años después de la publicación de Abraham, la batería de litio-aire no tuvo mucho interés por parte de la comunidad científica. A partir del año 2009 aproximadamente, el número de las publicaciones comenzó a aumentar significativamente.

Inicialmente, se empleaban los mismos electrolitos (carbonatos orgánicos) que se usó en las baterías de ion-litio, pero en poco tiempo se demostró que estos son altamente inestables en presencia de productos de reducción de oxígeno en el cátodo. Es ahí, que el foco de atención de la comunidad científica se centró en estudiar la estabilidad de diferentes sistemas para poder ser empleadas en estas baterías y también se comprendió la gran necesidad de llevar a cabo el estudio fundamental de las reacciones que ocurren en el cátodo de dicha batería.

## Chapter 2. Experimental details.

Handling of air-sensitive chemicals requires an additional training and extreme care at the time of solution preparation and experiment performance. We have employed an Argon-filled MBraun glovebox for the storage and manipulation of the chemicals, and vacuum drying and molecular sieves for the trace water elimination. We also have designed and manufactured numerous air-tight cells in order to perform electrochemical and spectroelectrochemical techniques, complemented with syringe-assisted solution transfer. The Karl Fisher titration was employed systematically to evaluate the trace water content and its evolution over the time in the samples. In this chapter we will describe the mentioned above essentials in handling air-sensitive materials and also the concrete details of the performed experiments.

### 2.1. Chemicals and solutions.

The following chemicals have been purchased for the research through the PhD training:

- Anhydrous dimethyl sulfoxide DMSO,  $\geq 99.9\%$  (276855 SIGMA-ALDRICH).
- Acetonitrile ACN anhydrous, 99.8% (271004 SIGMA-ALDRICH).
- Anhydrous N-butyl-N-methylpyrrolidinium bis(trifluoromethylsulfonyl)imide  $\text{PYR}_{14}\text{TFSI}$  (IL-0035-HP io-li-tec).
- Tetrabutylammonium hexafluorophosphate  $\text{TBAPF}_6$  for electrochemical analysis,  $\geq 99.0\%$  (86879 Fluka).
- Lithium hexafluorophosphate  $\text{LiPF}_6$  battery grade,  $\geq 99.99\%$  trace metals basis (450227 SIGMA-ALDRICH).
- Potassium dioxide  $\text{KO}_2$  (278904 SIGMA-ALDRICH).
- Lithium peroxide  $\text{Li}_2\text{O}_2$  technical grade, 90% (347043 SIGMA-ALDRICH).
- Lithium bis(trifluoromethane-sulfonyl) amide  $\text{LiTFSI}$  (544094 SIGMA-ALDRICH).
- Lithium metal wire, diam. 3.2 mm, 99.9% trace metals basis (220914 SIGMA-ALDRICH).
- Lithium titanate LTO, spinel nanopowder,  $<200$  nm particle size (BET),  $>99\%$  (702277 SIGMA-ALDRICH).

- 1-Methyl-2-pyrrolidinone NMP, ACS reagent,  $\geq 99.0\%$  (443778 SIGMA-ALDRICH).
- Poly(vinylidene fluoride) PVDF, average  $M_w \sim 180,000$  by GPC, average  $M_n \sim 71,000$ , beads or pellets (427152 SIGMA-ALDRICH).
- Lithium tetrafluoroborate  $\text{LiBF}_4$  ultra dry, powder, 99.99% trace metals basis (451622 SIGMA-ALDRICH).
- Molecular sieves, 3 Å beads, 4-8 mesh (208574 SIGMA-ALDRICH).
- Vulcan carbon X-72 (Cabbot Corp.).

All the water and oxygen-sensitive chemicals were stored in the argon-filled MBRAUN glove box with oxygen content  $\leq 0.1$  ppm and water content below 1 ppm.

Dimethyl sulfoxide and acetonitrile were dried for several days over 3 Å molecular sieves (208574 SIGMA-Aldrich). The lithium and alkylammonium salts, potassium dioxide and lithium peroxide were used as received. All solutions were prepared inside the glove box, and the water content was measured using the Karl Fisher 831 KF Coulometer (Metrohm).

Typically the high salt concentration solutions (around 0,1 M) based on organic solvents (DMSO and ACN) were found to contain around 50 ppm of water. It should be stressed that for RRDE experiments not only the initial concentration of water traces in organic solvent solutions was measured, but periodically during the experiments the amount of water was checked by Karl Fisher technique. In long term experiments of several hours we observed that in spite of all precautions and low humidity in the acrylic box, the amount of water measured in lithium containing DMSO electrolyte increased. Therefore, short term experiments with freshly prepared solutions and short exposure to dry air were preferred.

For the conductivity measurements, low salt concentrations were used and the solutions typically were found to contain less than 20 ppm of water at the beginning and less than 30 ppm of water at the end measurements.

Ionic liquid  $\text{PYR}_{14}\text{TFSI}$  and its mixture with  $\text{LiTFSI}$  were dried for several hours at  $80^\circ\text{C}$  under the vacuum and then transferred to the glove box.. The final water content was measured to be around 20 ppm.

## 2.2. MBraun glove box use and maintenance.

MBraun Labmaster SP/DP Argon filled glove box (figure 2.1) has been installed in the laboratory in the beginning of PhD training.



**Figure 2.1. MBraun Labmaster SP/DP glove box (at the manufacturer).**

The glove box was equipped with two antechambers (small and big), oxygen and water gas analyses and banana connections in order to perform electrochemical measurements inside the glove box. Only the experiments that did require neither water nor oxygen have been performed inside the glove box.

The slight positive overpressure was maintained inside the glove box (between 2 and 8 mbar overpressure over ambient pressure) in order to avoid contaminant diffusion inside the glove box.

The glassware was previously heated in the oven at 120°C with or without vacuum before introducing into the glovebox. The materials that could not be heated were flushed over with the dry nitrogen. Extremely hydrophilic materials were avoided. All the fluxes, bottles etc were

introduced opened in order to avoid ambient air capturing. When the small antechamber was used, at least three purges during 20 minutes in vacuum in between were performed. For the use of the bigger antechamber, at least five purges with the 60 minutes in vacuum in between were performed.

The water sensor was cleaned and moisture with new phosphoric acid every 90 days.

The glovebox was regenerated at regular intervals of about two-three months with the use of regeneration gas consisting of 95% Ar and 5% H<sub>2</sub>.

Typically the glove box contained less than 0.1 ppm oxygen and water values varying between 0.6 and 2.0 ppm.

The glove box was used routinely for the storage of air-sensitive chemicals, solution preparation, cell assembly, etc. The solutions were taken outside either in septum-sealed flasks, in syringes or assembled in the air-sealed electrochemical cells.

### 2.3. Karl Fisher water determination.

Karl Fisher water determination has been performed with the use of 831 KF Coulometer (Metrohm) that is shown on the figure 2.2.



**Figure 2.2. Metrohm 831 KF Coulometer.**

The Karl Fischer titration is based on the following reaction:



Iodine reacts quantitatively with water and this reaction is used to quantify water traces. In the Coulometric KF titration, the iodine is produced electrochemically, and the amount of produced iodine can be calculated precisely based on the electric charge. The endpoint is indicated volumetrically by applying an alternative current of constant strength to a double Pt indicator electrode, whose potential is very sensitive to the presence of minimal quantities to iodine in the solution. This allows the very exact determination of water traces in the solution of interest.

We have used the Coulometer with generator electrode with diaphragm, where anolyte and catholyte solutions are separated by a diaphragm. The Hydronal – Coulomat anolyte and catholyte solutions were purchased:

1) HYDRANAL - Coulomat AG, reagent for coulometric KF titration (anolyte solution), for cells with and without diaphragm (34836 Fluka)

2) HYDRANAL - Coulomat CG, reagent for coulometric KF titration (catholyte solution) (34840 Fluka).

Both catholyte and anolyte solutions were replaced periodically in the KF Coulometer.

All measurements were done after the initial titration drift was stable and less than 5  $\mu\text{g}/\text{min}$ . The measurements were done utilizing at least 1 ml of solution of interest, injected with the syringe, previously dried and rinsed with the solution of interest.

Whenever possible, the KF titration was performed at different stages of experiment: in pure solvents, after the drying with molecular sieves or vacuum, after solution preparation, during the cell filling, in the beginning and end of experiment, etc.

## 2.4. On the reference electrode in Li-air studies.

**Literature overview.** Unlike in aqueous electrochemistry where the normal hydrogen electrode potential is the reference electrode of choice, in the lithium battery community the electrode potentials are referred to the  $\text{Li}/\text{Li}^+$  system since in a lithium battery either the anode is Li metal or lithium intercalated in graphite with a redox potential very close to the metal  $\text{Li}/\text{Li}^+$  electrode.

Due to the strong solvation of the small lithium cation and the different electron donor capacity of different solvents, the electrode potential of  $\text{Li}/\text{Li}^+$  couple strongly depends on the solvent used and could it vary by as much as half of a volt between dimethyl sulfoxide and acetonitrile(84).

Furthermore, in many reports while the potential scale is referred versus the  $\text{Li}/\text{Li}^+$ , Li metal is not actually used as the reference electrode, but a different reference electrode such as  $\text{Ag}/\text{Ag}^+$  is employed and then converted into the  $\text{Li}/\text{Li}^+$  scale often without specifying how the was done.

Browsing through the Li-air literature we can find that in 2009 Laoire et al. used aqueous  $\text{Ag}/\text{AgCl}$  reference electrode and reported their data versus this reference. However they also indicated that  $\text{Ag}/\text{AgCl}$  gives a potential of 2.93 V versus  $\text{Li}/\text{Li}^+$ , as measured using a Li foil reference electrode in a  $\text{LiPF}_6$  solution in organic carbonates(85). This is an example of the very rare case in the Li-air literature, where the results were reported versus actual reference employed as we can see later since almost all the literature refer to the  $\text{Li}/\text{Li}^+$  scale. In 2010, the same authors used the Pt mesh as the reference electrode and reported their data versus  $\text{Li}/\text{Li}^+$ . They argued that the Pt electrode was calibrated with reference to the ferrocenium ion/ferrocene couple in each electrolyte studied, which in turn was calibrated to the  $\text{Li}/\text{Li}^+$  scale in ethylene carbonate/dimethyl carbonate based electrolyte(86). Allen et al.(87) reported their studies in ionic liquid and employed as reference an electrode that consisted of a silver wire immersed in a 0.1 M  $\text{AgCF}_3\text{SO}_3$  solution and converted the potentials to the  $\text{Li}/\text{Li}^+$  reference electrode by measuring the potential difference of the  $\text{Ag}/\text{Ag}^+$  electrode against a Li foil without specifying the solution. In 2013 Trahan et al. (53) reported studies of DMSO-based electrolyte for Li-air battery using a silver wire contained in a glass jacket filled with the working electrolyte plus a 10 mM addition of silver nitrate salt as a reference electrode. They reported a potential of 3.60 V versus  $\text{Li}/\text{Li}^+$  by calibrating their reference in the 1M  $\text{LiPF}_6/\text{DMSO}$  solution. Notably, the

Baltruschat's group have used the  $\text{Ag}/\text{Ag}^+$  reference electrode (silver wire immersed in a solution of 0.1M  $\text{AgNO}_3$  in the solvent used to prepare the electrolyte) and reported their values versus this reference (88, 89). Bruce's group, in turn, employed a reference electrode based on  $\text{LiFePO}_4$  and mentioned that the  $\text{Li}_x\text{FePO}_4$  reference potential was corrected to  $\text{Li}/\text{Li}^+$  by subtracting 3.45 V(90) (data found in the article's supplementary material). The group of Gasteiger reported studies with  $\text{PYR}_{14}\text{TFSI}$  ionic liquid using  $\text{Ag}/\text{Ag}^+$  reference electrode and calibrated versus  $\text{Li}/\text{Li}^+$  electrode (Li metal in  $\text{PYR}_{14}\text{TFSI}$  with 0.2 M  $\text{LiTFSI}$  with a value of  $3.160 \pm 0.002$  V (91)).

After extensive literature overview we can highlight some important aspects:

- 1) With very few exceptions (85, 88, 89) most of the Li-air literature refers the electrode potentials to the  $\text{Li}/\text{Li}^+$  potential scale.
- 2) In almost all the literature the  $\text{Li}/\text{Li}^+$  electrode has not been used as the actual reference electrode, but a variety of reference electrodes such as  $\text{Ag}/\text{AgCl}$ ,  $\text{Ag}/\text{Ag}^+$ , Ag wire, Pt mesh quasireference,  $\text{LiMn}_2\text{O}_4/\text{Li}_2\text{Mn}_2\text{O}_4$ , etc. have been employed.
- 3) The electrode potential measured vs. a reference electrode used in the experiment was later converted to  $\text{Li}/\text{Li}^+$  scale by measuring the potential between the reference and Li foil submerged in the same electrolyte used in the experiments (best case scenario) or a different solvent (for example organic carbonate), or without the indication of the solvent used at all.
- 4) Very often in the literature the  $\text{Li}^+$  concentration and solvent for  $\text{Li}/\text{Li}^+$  reference are not reported, thus indicating that many people in the field are not aware that the potential of  $\text{Li}/\text{Li}^+$  is highly dependent on the solvent of the lithium electrolyte.

**Reference electrodes preparation and use.** During this PhD thesis research, we have used either  $\text{Ag}/\text{Ag}^+$  or  $\text{Li}_2\text{Mn}_2\text{O}_4/\text{LiMn}_2\text{O}_4$  electrode as a non-aqueous reference

The reference  $\text{Li}_2\text{Mn}_2\text{O}_4/\text{LiMn}_2\text{O}_4$  electrode was prepared as described:

- 1)  $\text{LiMn}_2\text{O}_4$  synthesis:  $\text{Li}_2\text{CO}_3$  and  $\text{MnO}_2$  were mixed in a molar relation 0.51:2, grounded, pressed and heated at 350°C for 12 h and at 800 °C for 24 h.

2)  $\text{Li}_2\text{Mn}_2\text{O}_4$  synthesis: equimolar amounts of  $\text{LiMn}_2\text{O}_4$  and  $\text{LiI}$  were mixed and placed in a vacuum oven at  $80^\circ\text{C}$  overnight.

3) Equimolar quantities of  $\text{LiMn}_2\text{O}_4$  and  $\text{Li}_2\text{Mn}_2\text{O}_4$  were mixed with Carbon black (10% of total mixture weight) and PVDF binder (10% of total mixture weight) and dissolved in an appropriate organic solvent to make an ink.

4) A Pt wire was covered with the ink, and placed in a fritted glass compartment containing 1 M  $\text{LiPF}_6$  in DMSO solution.

A non aqueous  $\text{Ag}/\text{Ag}^+$  reference electrode was prepared by placing a silver wire in a fritted glass compartment filled with a 0.01  $\text{AgNO}_3$  solution in acetonitrile (0.1 M tetrabutylammonium hexafluorophosphate was added to the solution to increase conductivity).

Each reference electrode used has been calibrated with respect to  $\text{Li}/\text{Li}^+$  couple. Inside the argon glove box, a corresponding electrode and a Li wire were placed in a beaker filled with a solution of interest, and the cell potential was measured with a high-impedance voltmeter.

It is worth mentioning that while referring an electrode to the lithium wire, it should be taken into account that the potential of the  $\text{Li}/\text{Li}^+$  couple depends strongly on the electrolyte in which it measured since  $\text{Li}^+$  solvation energy depends on the solvent. For example potential measured between the same electrode and Li metal in a 0.1 M  $\text{LiPF}_6$  solution in acetonitrile was 0.47 V lower than that in DMSO solution. This difference is explained by an important  $\text{Li}^+$  solvation energy difference in DMSO and acetonitrile.

We also measured the  $\text{Li}/\text{Li}^+$  potential dependence on solvent composition in ACN–DMSO mixtures by resorting to the cell:



The liquid junction potential between the 1 M  $\text{LiPF}_6$  (DMSO) solutions and the 0.1 M  $\text{LiPF}_6$  solution in the studied ACN–DMSO mixture was calculated as:

$$E_j = (t_+ - t_-) \frac{RT}{F} \ln \left( \frac{a_1}{a_2} \right) \quad (2.2)$$

Where  $t_+$  and  $t_-$  are the transport numbers of the cation and anion, respectively and  $a_1$  and  $a_2$  the activities of the salt that form the liquid junction. We approximated the electrolytes activities with the concentration of the salt solutions considering this correction is minor. Based on conductivity studies (92-96), the transport numbers of  $\text{Li}^+$  in ACN and DMSO are 0.39 and 0.36, respectively. The calculated liquid junction potential varies between 0.013 V in ACN and 0.017 V in DMSO and can be neglected over all the range of ACN–DMSO compositions.

It should also be considered that the  $\text{Li}_2\text{Mn}_2\text{O}_4/\text{LiMn}_2\text{O}_4$  reversible reference electrode is immersed in DMSO, while the  $\text{Li}/\text{Li}^+$  electrode is in the ACN–DMSO mixture. Thus, an additional potential difference exists at the interface of DMSO with the corresponding ACN–DMSO mixture, due to the variation in the dielectric constant of the mixtures. In order to correct the measured potential due to the interface between the DMSO reference electrode and the ACN–DMSO mixture, we have also calibrated the  $\text{Li}_2\text{Mn}_2\text{O}_4/\text{LiMn}_2\text{O}_4$  reference electrode with the ferrocene  $\text{Fe}(\text{C}_5\text{H}_5)_2$  – ferrocenium couple for all the solutions of interest. The calibration was performed by measuring cyclic voltammograms in 0.1 M  $\text{LiPF}_6$  + 5 to 10 mM  $\text{Fe}(\text{C}_5\text{H}_5)_2$  in ACN–DMSO solutions, using a standard 3-electrode electrochemical cell with a Pt working electrode, a  $\text{Li}_2\text{Mn}_2\text{O}_4/\text{LiMn}_2\text{O}_4$  reference electrode and a carbon rod counter electrode.

## 2.5. Electrochemical experiments.

Electrochemical measurements were performed in standard 3-electrode air-tight glass or Teflon cells, with working electrode planar Au, Pt or glassy carbon GC (BASi) electrode, Platinum gauze 100 mesh (Aldrich cat. 298093) as counter electrode and the reference electrode as described in 2.4. For the oxygen diffusivity and solubility studies, the gold microelectrodes were used as working electrode. The gold microelectrodes were calibrated with ferrocene/ferrocenium couple and its radius determined as 12.4  $\mu\text{m}$  (will be described in more detail in chapter 5).

The RRDE electrochemical experiments were performed in an air-tight acrylic box filled with Ar and dried with phosphorous pentoxide keeping a positive pressure by a stream of dry oxygen (see figure 2.3). The motor controller, motor and disk and ring mercury contacts in the bearing block are located outside the air-tight acrylic box and sealed with a rubber ring with a permanent flow of dry oxygen in the box. The electrochemical cell and RRDE cylinder immersed in the aprotic electrolyte were kept inside the box. This box contained the four-electrode glass cell and the electrolyte was fed from bottles filled in the glove box by a system needles and Teflon tubes without contact with the atmosphere. Large area platinum gauze was used as counter electrode in a compartment separated from the main compartment by a fritted glass. Several rotating ring disk electrode systems have been employed as shown in Table 2.1. In all cases both disk and ring were embedded in Araldite epoxy resin cylindrical body (Ciba-Geigy). The geometrical area of the disk electrode was in all cases 0.196  $\text{cm}^2$ . The geometric collection efficiency was calculated using the Albery-Hitchman theory(97) and experimentally verified with the  $\text{Fe}(\text{CN})_6^{4/3-}$  redox couple in a galvanostatic experiment. Soluble superoxide was detected at the ring electrode by convective-diffusion oxidation current at  $E_R = 3.0 \text{ V vs Li/Li}^+$  in DMSO. At this potential there is no evidence of solvent decomposition, unlike for Pt ring electrodes.

**Table 2. 1. Geometric dimensions of RRDE used and the respective calculated and experimental collection efficiencies.**

Electrode	r1	r2	r3	$N_0$ calc.	$N_0$ exp.
GC/Au	0.25	0.26	0.31	0.32	0.32
Au/Au	0.25	0.26	0.30	0.29	0.28
GC/Pt	0.25	0.265	0.3	0.22	0.22

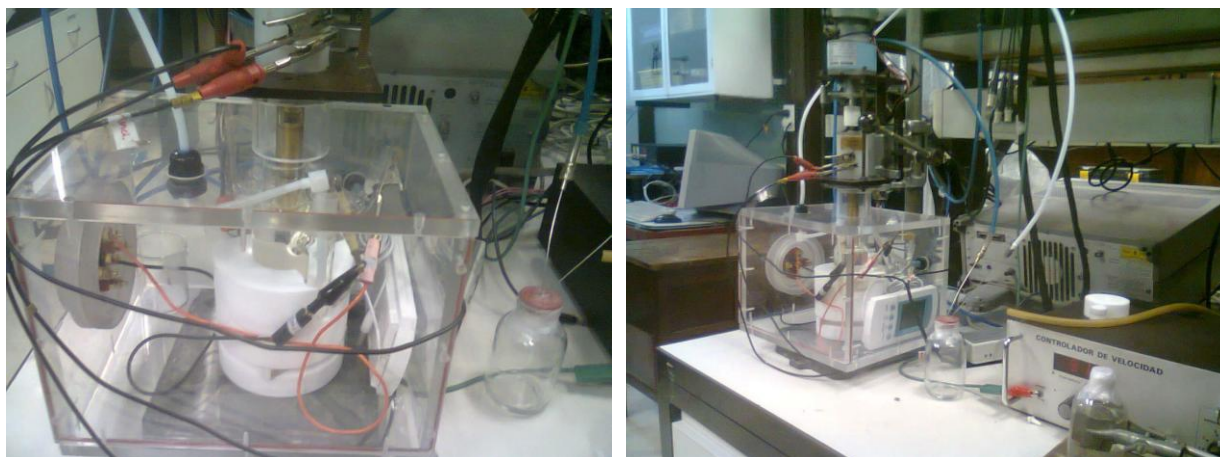


**Figure 2.3. Experimental Setup: Dry acrylic box used in Rotating Ring Disc Experiments.**

For the battery charge-discharge experiments, the costume-made cell was used (figure 2.4.) The cell consists of the anode electrode (Li metal or LLTO (lithiated lithium titanium oxide)) on the cell bottom, a cathode gas diffusion electrode (porous carbon) on top, and a separator (Celgard film embedded in electrolyte) in between. The upper gas diffusion type electrode is contacted by, and “breathes” through the stainless steel mesh current collector on top. The battery assembly is sandwiched in between two stainless steel conical springs (McMaster Carr 1692k22), that assure a constant pressure applied to the cell. The cell lid is equipped with two ports for gas inlet and outlet, so that compressed gas can be passed to the gas-diffusion electrode. The PTFE O-ring is placed in between upper and bottom battery parts. The cell is closed and sealed with a ss screw applying pressure on the top of sell assembly.

The cell was assembled inside the glove box with gas inlet and outlet sealed off by dummies. Once outside the glove box, the cell was connected to the dry oxygen line and purged with dry oxygen.

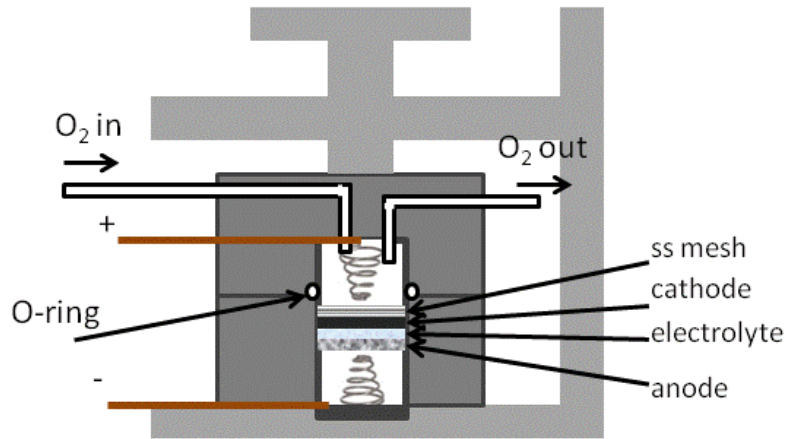
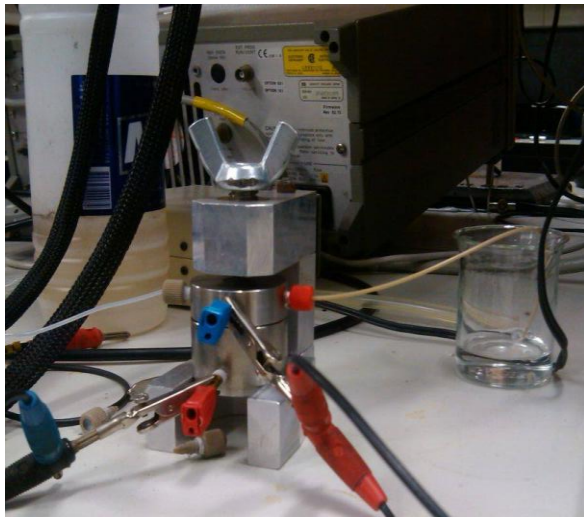


**Figure 2.4.**Li-air battery prototype photograph (left) and schematic representation (right).

## 2.6. Infrared experiments.

Electrochemical in situ subtractively normalized interfacial Fourier transform infrared spectroscopy (SNIFTIRS) experiments were carried out on a Thermo Nicolet 8700 (Nicolet, Madison, WI) spectrometer equipped with a custom-made external tabletop optical mount, an MCTA detector, and a custom-made Teflon electro-chemical cell (figure 2.5) with a polycrystalline gold or platinum disc electrode aligned against the CaF<sub>2</sub> window, a 1 in. (25 mm) CaF<sub>2</sub> equilateral prism (Harrick Scientific Technology). Typically, a few micrometers of electrolyte solution separated the electrode and the CaF<sub>2</sub> window. The design of spectroelectrochemical cells for FTIRS or PMIRRAS have been described before in the literature(98, 99). The electrochemical cell was a conventional three-electrode cell connected to a JaisleIMP88 Potentiostat controlled by the computer via a digital-to-analog converter (Agilent USB AD/DA converter). All potentials were measured with respect to a non aqueous reference electrode (as described in 2.4) and a Pt foil was used as counter electrode. The working gold electrode was polished first with 1 μm alumina, then with 0.3 μm and finally 0.05 μm alumina, until mirror-like appearance was achieved. The electrode potential was varied from open circuit potential to the potentials of interest. Each potential step comprises an equilibration time of 120 s followed by the acquisition of the spectrum by averaging 200 scans at 4 cm<sup>-1</sup> resolution.

For each system, a spectrum was obtained at open circuit and taken as reference. In a typical in situ FTIR spectroscopy experiment, it is necessary to measure a reference spectrum at a potential where the electrochemical process does not take place, and a sample spectrum where the desired process does take place. A ratio of the two spectra is then obtained. This type of experiment was originally called subtractively normalized interfacial Fourier transform infrared spectroscopy (SNIFTIRS). In SNIFTIRS spectra, usually there are bands in both up and down directions with respect to the baseline. Taking  $R_0$  as the reflectance in the reference spectrum and  $R$  as the sample spectrum reflectance, positive bands ( $R_0 > R$ ) correspond to the consumption of species and negative bands ( $R_0 < R$ ) correspond to the appearance of new species. Transmission spectra of the solutions were performed using a thin optical pass liquid cell with CaF<sub>2</sub> windows. The resolution was set to 4 cm<sup>-1</sup> and 200 scans were performed.

All measured spectra were processed with the OMNIC software in the following manner: standard gaseous water and carbon dioxide spectra were subtracted separately from each obtained spectrum in order to eliminate noise corresponding to ambient air.

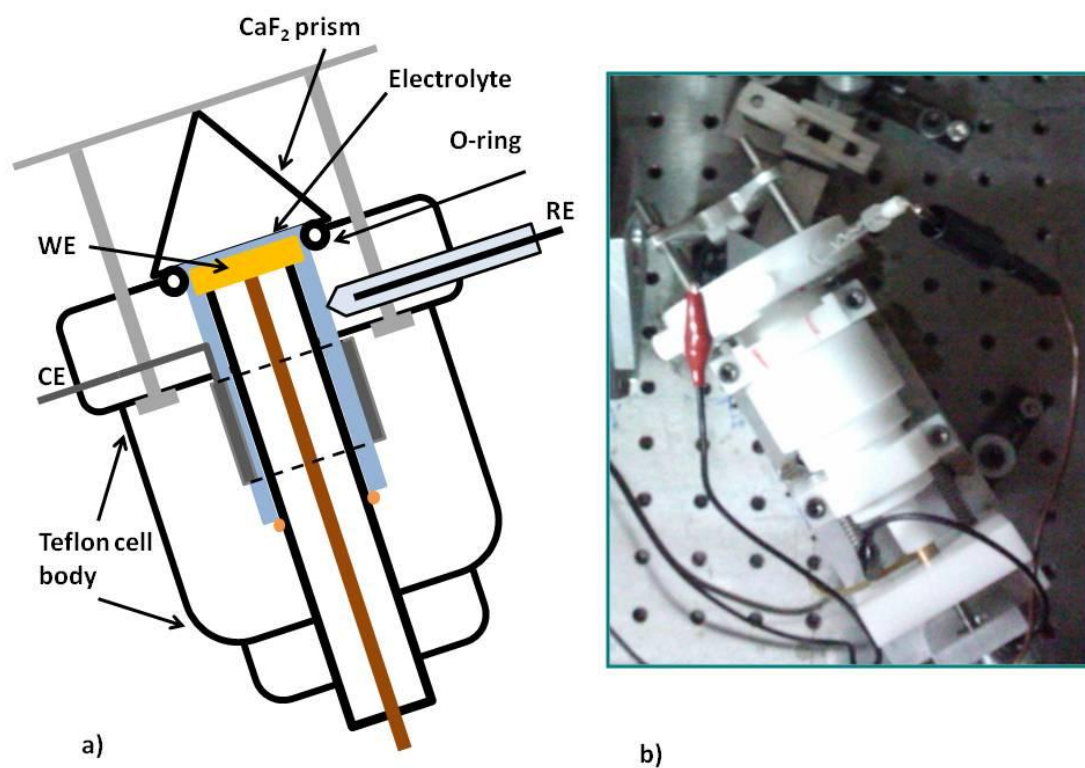


**Figure 2.5. Experimental spectroelectrochemical cell a) schematic representation and b) photograph. WE: working electrode, CE: counter electrode, RE: reference electrode.**

## 2.7. Differential electrochemical mass spectrometry (DEMS).

Differential electrochemical mass spectrometry (DEMS) was accomplished using a Pfeiffer vacuum Omnistar GSD 320 gas analysis system with a base pressure of  $10^{-8}$  mbar and with a quadrupole mass spectrometer QGM 220 (mass range 1-200 amu) operated with a secondary electron multiplier. The DEMS cell setup was a modification of the design pioneered by Baltruschat et. al.<sup>33, 34</sup> and consisted of a stainless steel base with a PTFE body. A gold sputtered PTFE membrane gas diffusion electrode (200  $\mu\text{m}$  thick and 0.1 micrometer pore diameter T01047WPH Microclar Teflon) with 0.50  $\text{cm}^2$  geometric electroactive area located at the bottom of the cell. The Au sputtered membrane was mechanically supported on a porous stainless steel frit. Surface tension of the solvent DMSO ( $43.5 \text{ mNm}^{-1}$ ) prevents penetration in the capillary porous structure of the PTFE membrane.<sup>35, 36</sup> A non-aqueous  $\text{LiMn}_2\text{O}_4/\text{LiMn}_2\text{O}_4$ <sup>30</sup> reference electrode in the same electrolyte was used in a fritted glass compartment and a  $1 \text{ cm}^2$  platinum gauze (Johnson Matthey) was employed as counter electrode. The flow system consisted of a Cole-Parmer Co. micropump to circulate the non aqueous electrolyte through the DEMS cell in an air tight system. The electrochemical cell was connected to the gas analyzer by connecting the outlet of the porous frit in the cell directly to the inlet valve of the MS analyser via an stainless steel cross. The two other ports were used to connect a mechanical pump via an on/off valve and a piezoelectric pressure sensor (details). This setup allowed monitoring the pressure at the back of the membrane and differentially pumping the vacuum side of the membrane. The typical pressure at the back of the membrane was approximately 1 mbar whereas the typical pressure in the MS was  $10^{-7}$  mbar. The inlet of the MS analyzer in the OmniStar system is differentially pumped by the 60 l/s turbomolecular pump that also pumps the MS.

## 2.8. Viscosity and conductivity measurements in organic solvents.

**Viscosity of ACN–DMSO mixtures.** Owing to the significant difference between the literature reported viscosity values of the mixtures (*100, 101*) (up to 20% difference for some compositions), we measured the viscosities of ACN–DMSO mixtures in the whole composition range with Cannon–Fenske (Ostwald modification) viscometers size 25 (0.5 – 2 mPa s) and size 50 (0.8 – 4 mPa s), calibrated with water. For viscosity determinations, viscometers were filled with the solution of interest inside the glovebox, sealed with Teflon caps, taken out of the glove box and thermostated in a water bath at  $298.15 \pm 0.05$  K. Then, the viscometers were opened and measurements were performed immediately to avoid water contamination.

**Conductivity of LiPF<sub>6</sub> and TBAPF<sub>6</sub> in ACN–DMSO mixtures.** An air-tight glass conductivity cell with a mixing bulb and platinized platinum electrodes was used to determine the conductivity of LiPF<sub>6</sub> and TBAPF<sub>6</sub> in ACN–DMSO mixtures as a function of electrolyte concentration ( $10^{-5}$  –  $10^{-3}$  M) and solvent composition. Conductivity measurements for LiPF<sub>6</sub> were performed for ACN–DMSO mixtures with ACN mole fractions ( $\chi_{\text{ACN}}$ ) = 0.000, 0.192, 0.373, 0.453, 0.586, 0.697, 0.798, 0.898, 0.947, 0.968, 0.995, and 1.000. Measurements for TBAPF<sub>6</sub> were performed for  $\chi_{\text{ACN}}$  = 0.269, 0.492, 0.754, and 0.960.

The cell constant,  $\kappa_{\text{cell}} = 0.0710 \pm 0.0008$  cm<sup>-1</sup> at 298.15 K, was determined using a standard KCl aqueous solution of known specific conductivity (*102*).

The conductivity measurements were performed according to the following protocol: first, the conductivity cell was filled with the solvent inside the glove box, by weighting the corresponding amounts of ACN and DMSO to obtain the desired composition. Then, the cell was transferred to an oil bath thermostated at  $298.15 \pm 0.08$  K and after reaching thermal equilibrium, the solvent resistance was measured. Afterwards, increasing weighted amounts of a stock solution of LiPF<sub>6</sub> or TBAPF<sub>6</sub>, prepared inside the glove box, in an ACN–DMSO mixture of equal composition, were added. Additions were transferred from a stock solution containing vessel to the conductivity cell (both air-tight and equipped with septum) with the use of a syringe. The resulting solution was homogenized by manual stirring; after reaching a new thermal equilibrium, the solution resistance was determined.

The salt molar conductivities,  $\Lambda$ , were determined according to

$$\Lambda = \frac{\kappa}{c} = \left( \frac{1}{R} - \frac{1}{R_0} \right) \frac{\kappa_{cell}}{c} \quad (2.3)$$

where  $\kappa$  is the solution specific conductivity,  $c$  is the electrolyte molar concentration,  $R$  is the solution resistance, and  $R_0$  is the solvent resistance. For the resistance measurements a precise LCR meter (GWIN-STEK) was used. An AC voltage (100 mV) was applied to the electrodes at different frequencies and the resistive and capacitive components were recorded, considering an equivalent resistance – capacitance parallel circuit. The resistance was recorded at several frequencies between 0.3 and 5 kHz and the extrapolated value at infinite frequency was computed.

**Conductivity data treatment.** The salt molar conductivity data as a function of concentration was analyzed with the equation given by Fuoss–Hsia–Fernandez Prini (FHFP) (103), which accounts for ionic association:

$$\Lambda = \Lambda^0 - S(\alpha c)^{\frac{1}{2}} + E\alpha c \ln(\alpha c) + J_1(d)\alpha c - J_2(d)(\alpha c)^{\frac{3}{2}} - K_a \Lambda \gamma_{\pm}^2(\alpha c) \quad (2.4)$$

Where  $c$  is the salt molar concentration,  $d$  the distance of closest approach of the free ions, whose concentration is  $\alpha c$ , with  $\alpha$  the degree of dissociation. The constants  $S$ ,  $E$ ,  $J_1$  and  $J_2$  were calculated using the equations given by Fernandez Prini (103) with the viscosity and dielectric constant data of the ACN–DMSO mixtures. The mean activity coefficient of the ions was approximated by the Debye–Hückel equation:

$$\ln \gamma_{\pm} = \frac{-A\sqrt{\alpha c}}{1+d\kappa} \quad (2.5)$$

Where  $\kappa$  is the reciprocal radius of the ionic atmosphere, and  $A$  was calculated using the dielectric constant data of the mixtures. The degree of dissociation  $\alpha$  is related to the association constant  $K_a$  by

$$K_a = \frac{(1-\alpha)}{\gamma_{\pm}^2 \alpha^2 c} \quad (2.6)$$

A non linear fit of  $\Lambda$ ,  $c$  data allowed the determination of  $\Lambda^0$  and  $K_a$ . The salt molar concentration  $c$  was determined from the weights of salt and solvents using the density of the mixture. The thermophysical properties of the ACN–DMSO mixtures (density(101) and dielectric constant (100)) at 298.15 K were fitted with polynomial equations as a function of composition, and the corresponding values for the measured compositions are given in Table 5.1 in chapter 5. Viscosity was fitted in logarithmic scale as a function of composition as will be discussed in chapter 5.

## 2.9. Electrochemical quartz crystal microbalance (EQCM).

EQCM CELL: The electrochemical cell was built all in Teflon<sup>®</sup> and the 10 MHz quartz crystal (Intl. Crystal Manufacturer, Oklahoma) were coated with 0.2 cm<sup>2</sup> gold disks (with 200 nm Au on titanium adhesion layer), placed at the bottom and filled with the electrolyte. Dupont<sup>®</sup> Kalrez perfluoroelastomeric AS568 o-rings were used (Viton o-rings are not suited since they swell in contact with DMSO).

EQCM Measurements: Crystal admittance spectra in the vicinity of the fundamental resonant frequency,  $f_o$ , were acquired using a Hewlett Packard HP E5100A network analyzer connected to the quartz crystal in the Teflon electrochemical cell through 50  $\Omega$  coaxial matched cables (HP10502A) via a HP 41900A  $\pi$ - Network test fixture with rigid brass connectors to the crystal. The HP E5100A network analyzer was interfaced to a computer via Agilent 82357B USB/GPIB interface and the electrochemical cell was controlled with a grounded working electrode by means of an operational amplifier potentiostat/ galvanostat with special software developed in the laboratory using Labview 10.0 (National). The working electrode was isolated by means of a series 4.7 nF capacitor, the electrochemical current was measured at the auxiliary electrode and both current and potential signals were acquired by 2 Agilent 34410 61/2 digit multimeters by USB interfaces. The network analyzer was calibrated prior to each measurement by 3-term calibration: open, close and 50  $\Omega$  . The acoustic admittance spectra of the Au covered quartz crystal were recorded at 1.5 s intervals simultaneously to current and potential signals for the oxygen reduction reaction (ORR).

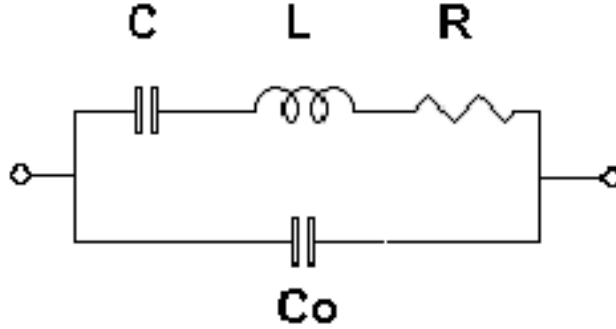
The electrical complex admittance of the Buterworth van Dyke (BVD) equivalent electrical circuit is:

$$Y(\omega) = G(\omega) + jB(\omega) \quad (2.7)$$

where the real part  $G(\omega)$  is the conductance and the imaginary part  $B(\omega)$  the susceptance of the quartz crystal admittance is given in terms of the BVD elements:

$$G = \frac{R}{R^2 + \left(\omega L - \frac{1}{\omega C}\right)^2} \quad \text{and} \quad B = \omega C_o - \frac{\left(\omega L - \frac{1}{\omega C}\right)}{R^2 + \left(\omega L - \frac{1}{\omega C}\right)^2} \quad (2.8)$$

With  $j = \sqrt{-1}$  and  $\omega_o = 2\pi f_o$  defines the series resonant frequency of the quartz crystal with a maximum conductance  $G(\omega_o)_{\max} = 1/R$  at the resonant frequency.



**Scheme 2.1. BVD electrical equivalent circuit  $C_0(LCR)$  for the quartz crystal resonator.**

The resistance,  $R$ , represents all the energy losses of the shear wave penetrating the liquid and surface film or surface particle asperities as well as losses in the o-ring support. Typical values of  $R_q = 40 \Omega$  (including O-ring and crystal fitting),  $L_q = 8.5 \text{ mH}$ ,  $C_q = 30 \text{ fF}$ , and  $C_0 = 5 \text{ pF}$  for 10 MHz crystals in air with  $\omega L$  (total)  $\sim 535,000 \Omega$  were obtained and experimentally verified.

For low crystal load by the surface deposit ( $Z_L \ll Z_Q$ ) a lumped element circuit can be approximated and the shift in the quartz impedance due to the ORR products deposit can be written:

$$\Delta Z = \Delta R + j\Delta(\omega L) \quad (2.9)$$

Where  $\Delta R$  and  $\Delta(\omega L)$  are the real and imaginary parts of the impedance shift with respect to the initial quartz crystal condition before the beginning of the ORR process.

For acoustically thin deposits, the Saurbrey equation relates the resonant frequency shift with the areal mass of deposit:(104)

$$\Delta f = -\frac{(2f_o^2)}{\sqrt{(\rho_Q \mu_Q)}} \cdot \frac{\Delta m}{A} \quad (2.10)$$

$\Delta f$  is the measured frequency shift,  $\Delta m$  the mass loading,  $A$  the piezoelectrically active area, the quartz density ( $\rho_Q = 2.648 \text{ g.cm}^{-3}$ ) and the shear modulus of AT-cut quartz ( $\mu_Q = 2.947 \times 10^{11}$ )

dyn cm<sup>-2</sup>). The sensitivity factor increases at high resonant frequency of the resonator which corresponds to a thinner quartz crystal; for example a 10 MHz AT-cut quartz crystal 0.017 cm thick has a nominal sensitivity of 0.226 Hz cm<sup>2</sup> ng<sup>-1</sup>.

For acoustically thin films ( $R \rightarrow 0$ ), the equivalent of eqn. (2.10) is:

$$\Delta(\omega L) = \Delta X_L = -\frac{\pi Z_Q \Delta f}{f_o} = \frac{2\pi Z_Q \Delta m}{\sqrt{(\rho_Q \mu_Q) A}} = 4.6 \times 10^{-8} \frac{\Delta m}{A} \quad (2.11)$$

with the conversion factor  $4.6 \times 10^{-8} \text{ g.cm}^{-2}.\Omega^{-1}$  calibrated by electrodeposition of copper on Au in water and the deposited mass calculated from the number of moles deposited with the Faraday law of electrolysis and the molar mass.

In order to check the feasibility of use of EQCM in ionic liquid  $\text{PYR}_{14}\text{TFSI}$ , the conversion factor was also calculated by depositing copper from the ionic liquid. First, the copper was dissolved electrochemically in ionic liquid from the high purity copper rod. This is evidenced by recorder cyclic voltammetry of  $\text{Cu}^+/\text{Cu}$  couple as shown in the figure 2.6.

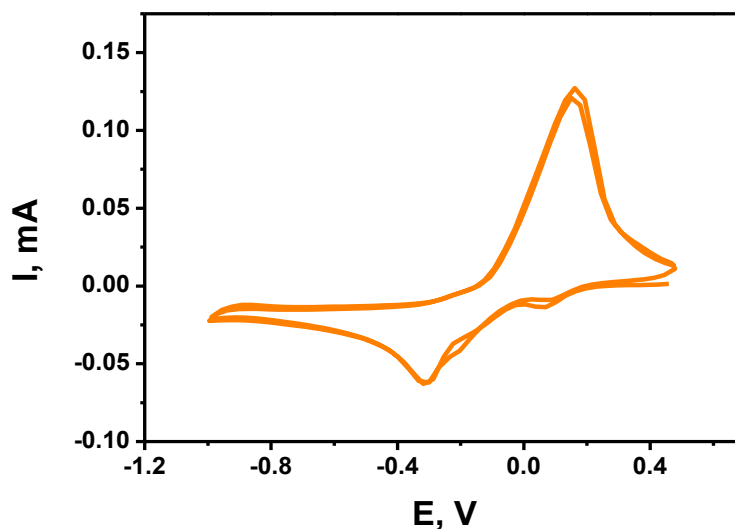


**Figure 2.6. CV recorded in the  $\text{PYR}_{14}\text{TFSI}$  ionic liquid containing electrochemically dissolved  $\text{Cu}^+$  ions, performed at 20 mV/s, in the EQCM electrochemical cell with Au coated quartz crystal working electrode,  $\text{Ag}/\text{Ag}^+$  reference electrode and Pt mess counter electrode.**

Then the galvanostatic pulses of + 10  $\mu\text{A}$  and - 10  $\mu\text{A}$  were applied to the cell and  $E$ ,  $\Delta(\omega L)$  and  $\Delta R$  were recorded as a function of time (see figure 2.7.)

The  $\Delta(\omega L)$  was plotted versus charge, smoothed, and a conversion factor was calculated from the slope in the obtained graph (see figure 2.8.) according to:

$$1/C_f = M/(nFA \cdot 1000 \cdot \text{slope}). \quad (2.12)$$

Where  $M$  is the molecular mass of  $\text{Cu}$ ,  $n$  is the number of electrons  $n=1$  for the reaction of  $\text{Cu}^+/\text{Cu}$  in ionic liquid,  $F$  is the Faraday constant and  $A$  is the electrode area.

We have obtained the value of  $5.3 \times 10^{-8} \text{ g} \cdot \text{cm}^{-2} \Omega^{-1}$ , very close to the conversion factor calculated in the aqueous solution. Notice the large value of the dissipation parameter in the BVD electrical equivalent circuit, for the highly viscous ionic liquid. However, the increase and decrease in mass due to copper deposition and dissolution does not affect appreciable  $R$ .

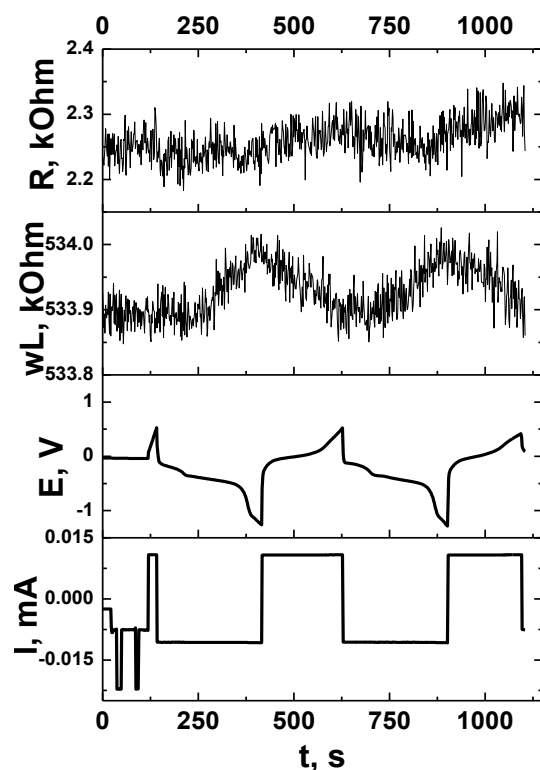


**Figure 2.7. Current pulses ( $\pm 10 \mu\text{A} \cdot \text{cm}^{-2}$ ) and simultaneous electrode potential evolution, time evolution of  $\Delta(\omega L)$  and  $\Delta R$  recorded simultaneously to the current pulses.**

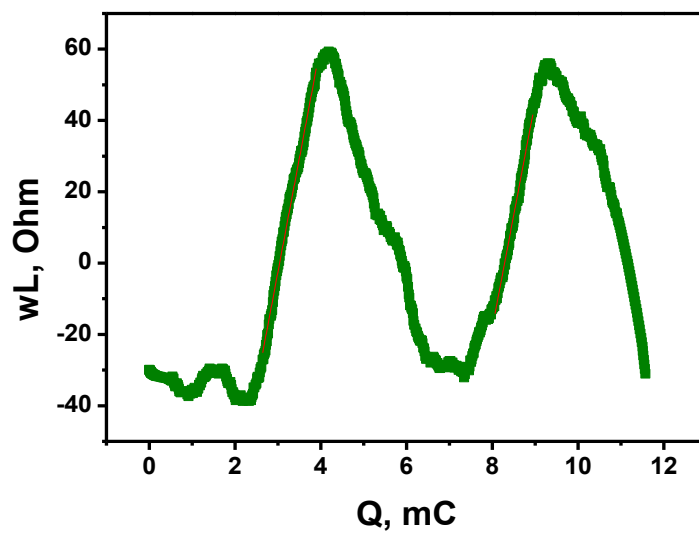


Figure 2.8.  $\Delta(\omega L)$  plotted versus charge  $Q$  during the current pulses ( $\pm 10 \mu\text{A}\cdot\text{cm}^{-2}$ )

## **2.10. Resumen en castellano del capítulo 2. Detalles experimentales.**

El trabajo con sustancias químicas sensibles al aire requiere de un entrenamiento adicional y un cuidado extremo al momento de preparar soluciones y llevar a cabo los experimentos. Para ello, hemos empleado una caja de guantes marca MBraun llena con argón para el almacenamiento y manipulación de los distintos reactivos grado batería, asimismo hemos usado el secado de sales de litio y líquidos iónicos a vacío y tamices moleculares para la eliminación de trazas de agua en solventes no acuosos. También hemos diseñado y construido varias celdas selladas al ambiente para llevar a cabo los experimentos electroquímicos y espectroelectroquímicos, usando jeringas como complemento para el llenado de dichas celdas con las soluciones a medir. La titulación Karl Fischer fue empleada de manera sistemática para evaluar el contenido de trazas de agua en las muestras y su evolución en el tiempo. En este capítulo se describe en detalle la complejidad del manejo de los reactivos sensibles al aire y también se detallan los experimentos llevados al cabo.

Entre las técnicas usadas se puede destacar las medidas electroquímicas como por ejemplo el uso del electrodo rotatorio de disco y anillo, también se explican las condiciones experimentales en los procesos de carga-descarga en una batería de Litio-aire fabricada en el laboratorio, se explican las medidas de la viscosidad y conductividad, se hace un resumen acerca de la técnica espectroscópica infrarroja por transformada de Fourier diferencial normalizada, espectroscopía de masa diferencial electroquímica y balanza de cristal de cuarzo electroquímica. La balanza de cristal de cuarzo electroquímica fue usada con el líquido iónico de muy alta viscosidad y por tal motivo se calibró con la solución de cobre en el líquido iónico.

# Chapter 3. Li-air battery prototype testing: the visualization of the problem.

## 3.1. Introduction

Over the last years numerous electrolyte-solvent systems were tested in the Li-air battery, however in a different extent, they all were found to degrade

As was mentioned earlier in this thesis, ionic liquids are of particular interest as a potential electrolyte system for the Li-air battery, with 1-Butyl-1-methylpyrrolidinium bis(trifluoromethylsulfonyl)imide  $\text{PYR}_{14}\text{TFSI}$  being one of the most investigated ionic liquid for battery applications. There are few examples of this ionic liquid application in the Li-air battery, showing both improved and fading performance (*105, 106*). Therefore, we have used this particular ionic liquid based electrolyte in order to test the Li-air battery prototype.

While, the vast research effort is concentrated to overcome the instabilities occurring on the cathode side, the lithium metal anode irreversibility remains an unsolved problem mainly ignored by field contributors. The lithium metal is highly reactive with chemical moieties, the mechanisms of its deposition and dissolution are poorly controlled and it is generally perceived as a safety hazard. The lithium metal cycling was found already to be challenging in the Li-ion systems, mainly due to the dendrite formation, however in the Li-oxygen system, the lithium cycling can be even more challenging due to the presence of molecular oxygen and its reduced species, their crossover to the anode, and also the parasitic reactions with redox mediators.

Therefore, the progress in the Li-air field is hindered by the instabilities of all three main components: anode, electrolyte and cathode, and their synergetic effects, and sometimes it may be difficult to separate which of these components contributes to the battery fading performance. There are even some studies that suggest that the lithium anode is the main reason of Li-air fading performance, due to problems related to oxygen crossover (*107*) and accumulation of lithium hydroxide (*108*). Therefore, the lithium metal protection membranes or other more stable anode materials have to be exploited both in the basic research and for the probable commercial applications. From the point of view of fundamental research, the substitution of lithium metal

anode with other more stable material, for example lithium titanate or hard carbons (HC), may help the researchers to distinguish better between anode and cathode parasitic chemistries.

There are several tactics that can be used to hinder the problems associated with oxygen crossover and parasitic chemistry on the lithium anode:

**1) Lithium metal protective films.** Many solvents that are used in the Li-oxygen battery testing do not form a stable SEI layer on the lithium. However some additives, such as  $\text{LiNO}_3$  may lead to the formation of stable SEI in these solvents.(65, 70, 71). On the other hand, Zheng et al. have reported the coating of lithium anode with a monolayer of interconnected amorphous hollow carbon nanospheres for the efficient lithium protection.(109) And some groups have stabilized the lithium metal by keeping than in the solution of propylene carbonate for at least three days before cycling it in the other solvent (DMSO).(36)

**2) Two-compartment cell.** This strategy implies that anode and cathode are separated by solid electrolyte membrane that allow a free path of  $\text{Li}^+$ , and each of the compartments is filled with the solution that works best either for the lithium anode or porous oxygen cathode electrodes.(105, 110)

**3) Substitution of lithium with other anode material.** The feasibility of the use of pre-lithiated hard carbons as an anode material with diglyme-based electrolytes was examined by Hirshberg et al.(111). On the other hand, Gasteiger's group have examined LTO/LLTO anodes for the Li-air battery(105, 112)

We have prepared the lithiated lithium titanate in order to substitute the lithium metal and to avoid the related parasitic chemistry, and to assess better the cathode and electrolyte associated fading performance. It is worth mentioning that LTO anode possesses low specific capacity and its redox potential is high, therefore with LTO anodes, the Li-air battery loses its advantages in energy density, however it is a suitable counter electrode for the system development from academic point of view.

### 3.2. Substitution of Li metal anode and Li-air battery charge-discharge experiments.

Lithium titanate was considered already for the applications in Li-ion batteries (113-118). It is a “zero strain” material(114) (no volume change during lithium insertion-extraction) and it possesses valuable properties: safety(115), lifetime, availability, good cycling and efficiencies. However it also has some drawback as high voltage and low capacity (low energy density). The graphite, which is currently used as anode material in most commercially available Li-ion batteries, has a potential of 0.1 V vs. Li/Li<sup>+</sup>, however for LTO this value is 1.5 V vs. Li/Li<sup>+</sup>. The lithium intercalation into LTO occurs according to the reaction:

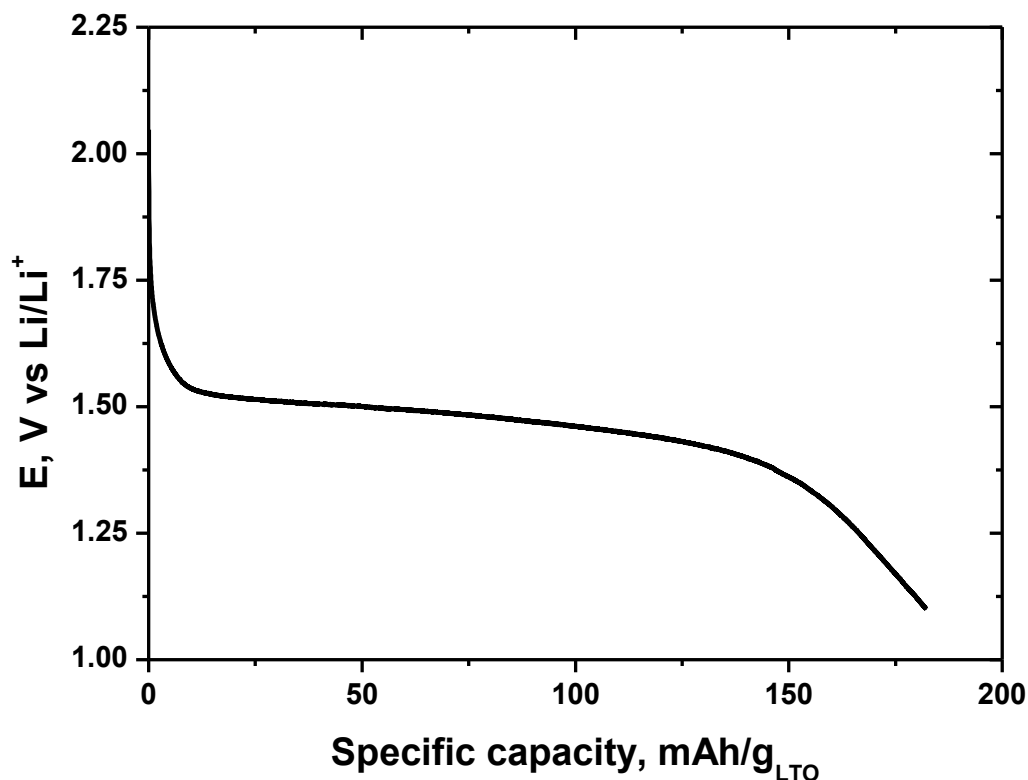


where x is usually 3.

It is suggested that LTO prevents anode-side electrolyte decomposition because of its high intercalation potential that lies inside the stability window of the commonly used electrolytes, meaning that the SEI formation is not necessary for the proper functioning. However there is no complete agreement whether the LTO is truly surface layer free material and there is an evidence of surface films formation on the LTO (119).

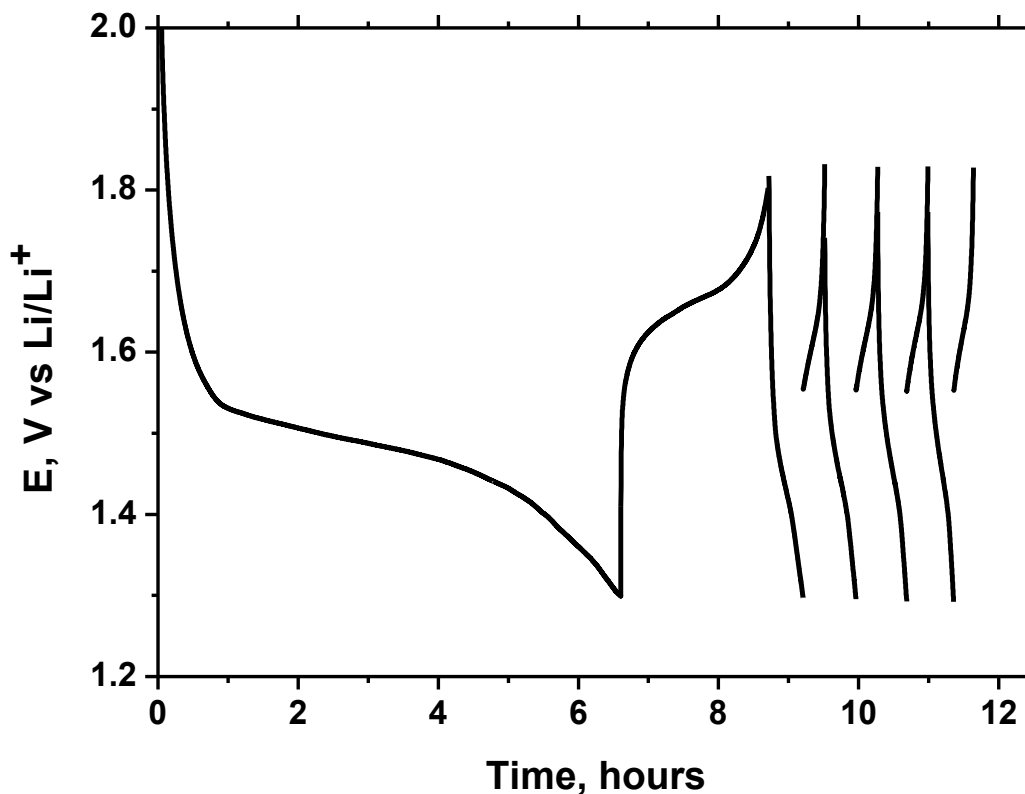
In the Li-air battery field, the idea of substitution of lithium metal is not widely practiced. To the best of our knowledge, only the Gasteiger’s group has investigated the feasibility of the use of LTO anodes in the Li-oxygen cell. However, they concluded that the SEI absence on the anode leads to the oxygen reduction on the LLTO(105).

Figure 3.1 shows a typical voltage profile of Li/LTO half-cell with the flat operating potential at around 1.5 V vs. Li/Li<sup>+</sup> and achieved discharge capacity of about 150 mAh/g<sub>LTO</sub>, that is in perfect agreement with previously reported studies(116-119). However it is worth mentioning that in the majority of previously reported literature organic carbonates were employed as electrolyte systems, known for the formation of stable SEI layer on various intercalation compounds and the lithium metal. Here, we were able to show a successful lithium intercalation into lithium titanate oxide from the ionic liquid based electrolyte.



**Figure 3.1. Discharge curve of the cell: LTO/ 0.6 M LiTFSI in PYR<sub>14</sub>TFSI / Li, at current of 40  $\mu$ A (10 mA/g<sub>LTO</sub> or 0.03 mA/cm<sup>2</sup>)**

Unfortunately, this process is not reversible over the various cycles as shown on the figure 3.2. It is observed that the delithiation capacity is about three times smaller than the expected one, and that the following cycles do not show practically any potential plateau. Taking into account the reported instability of this particular ionic liquid during the cathodic polarization of lithium electrode(120) and that this electrolyte does not form a stable SEI layer as in organic carbonates, and the effect of clogging of Li<sup>+</sup> diffusion channels in the SEI(121), we assume that the performance fading occurs as the result of electrolyte decomposition on the lithium metal, and is not related to the lithium titanate.



**Figure 3.2. Charge-discharge curves of the cell: LTO/ 0.6 M LiTFSI in PYR<sub>14</sub>TFSI / Li, at current of 40  $\mu$ A (10 mA/g or 0.03 mA/cm<sup>2</sup>)**

Therefore, for the use an anode in the Li-air cell, we have used the LLTO obtained from the single discharge of LTO/Li half-cell as shown in the figure 3.1.

The first discharge profile of the battery consisting of LLTO anode, ionic liquid based electrolyte and Vulcan carbon porous cathode, under a constant oxygen flow, is shown on the figure 3.3. The voltage plateau is observed at 1 V vs. LLTO anode that corresponds to 2.5 V vs Li metal, typical operating voltage of Li-air cell. The cell discharge is terminated with a sharp potential drop that is called “sudden death” and is normally explained by the clogging of cathode pores by insulating lithium peroxide and parasitic chemistry products. The achieved capacity represents a very small value compared to the majority of reported cells, which could be explained by the cathode surface area-porosity-architecture-loading interplay, which was not set up to the optimum conditions, as it was not the goal of the experiment.

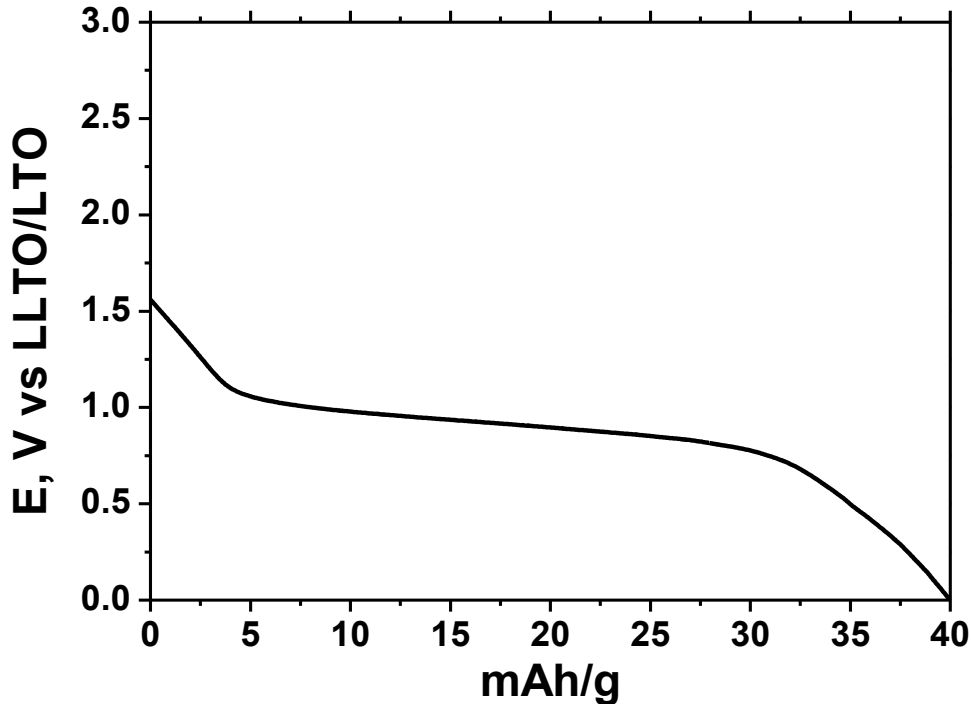


**Figure 3.3. First discharge profile of the cell LLTO/ 0.6 M LiTFSI in PYR<sub>14</sub>TFSI / C in 1 atm O<sub>2</sub> at current of 40  $\mu$ A (15 mA/g<sub>C</sub> 0.03 mA/cm<sup>2</sup>)**

The subsequent charge and the following cycles are depicted on the figure 3.4. The first recharge curve does not possess a plateau but increases steadily up to 3V, which corresponds to 4.5 V vs. lithium metal and is a typical cut off in the Li-air measurements. Notably, every following cycle possesses much smaller discharge capacity and the plateau is absent. Therefore, even when the lithium metal is substituted by LLTO anode, the cell is characterized by extremely limited cycle retention, and it can be concluded that the cathode and electrolyte are mainly responsible for the battery fading performance and further investigation into cathode fundamental electrochemistry is required.

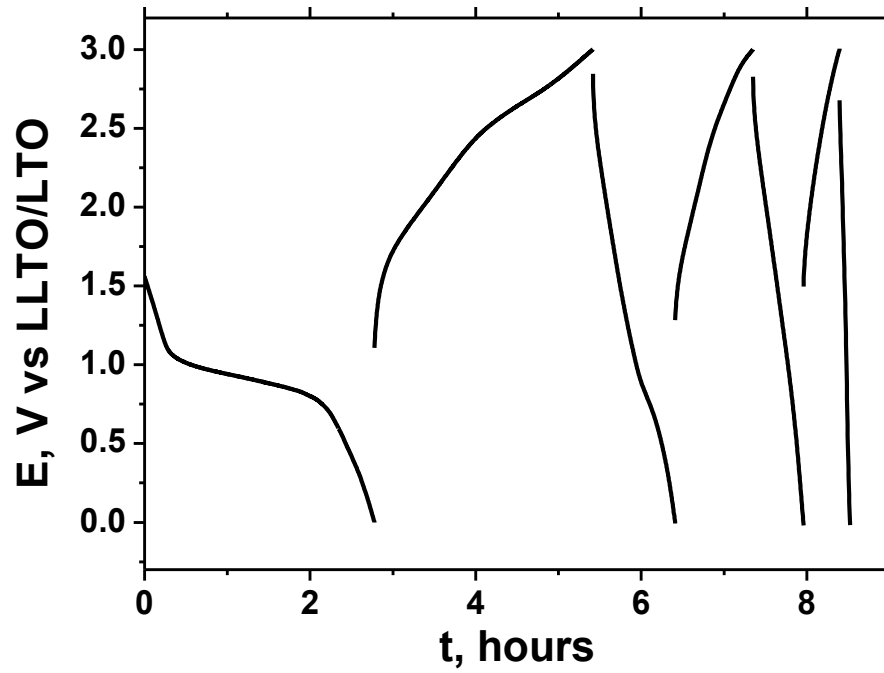


Figure 3.4. Charge-discharge profiles of the cell LLTO/ 0.6 M LiTFSI in PYR<sub>14</sub>TFSI / C in 1 atm O<sub>2</sub> at current of 40  $\mu$ A (15 mA/g<sub>C</sub> 0.03 mA/cm<sup>2</sup>)

### 3.3. Conclusions.

The literature browse showed the uncertainty on whether anode or cathode side was mainly responsible for the Li-air battery's fading performance. In order to sort it out, we have replaced the lithium metal anode with the lithiated lithium titanate.

The lithium titanate was successfully lithiated in the ionic liquid electrolyte medium, however the performance failed over the few cycles. We would assume that to be mainly related to the parasitic chemistry in the lithium metal anode. The Li-air cells built with LTO anode and porous carbon cathode were found to have very low cycle retention which is in agreement with most reported literature. The low cycle retention can be explained by the electrolyte and cathode instabilities and to the cathode occlusion by discharge species.

Therefore we concluded that the cathode and electrolyte, even when the lithium anode is replaced, are still responsible for the battery low cycleability, which is in agreement with many previously reported results. This means, that a deeper understanding of the basic Li-air battery electrochemistry at the cathode side is essential, such as mechanisms of Oxygen Reduction Reaction (ORR) during discharge, and Oxygen Evolution Reaction (OER) during charge, as well as the solvent, electrolyte and cathode material decomposition reactions mechanisms.

To conclude, in this chapter we visualized the Li-air battery challenge by performing charge-discharge experiments, and justified the necessity of deeper studies into the oxygen reduction and evolution reaction.

### **3.4. Resumen en castellano del capítulo 3. Pruebas del prototipo de batería de Litio-aire: visualización del problema.**

Mientras que la mayoría de la investigación científica está enfocada en resolver las reacciones indeseadas que ocurren en el cátodo de batería de Litio-aire, la irreversibilidad del ánodo de litio metálico sigue siendo un problema no resuelto y mayormente ignorado por los investigadores. El litio metálico es altamente reactivo, los mecanismos de su deposición y disolución son muy difícilmente controlados y generalmente es considerado como un material peligroso. Se ha demostrado que el ciclado del litio metálico es un sistema desafiante en las baterías de ion-litio, mayormente por razones tales como la formación de dendritas, pero en los sistemas de Litio-aire, el ciclado de litio puede ser un reto más dificultoso debido a la presencia del oxígeno molecular y sus especies reducidas, a su difusión hacia el ánodo y también a las reacciones parásitas con los mediadores redox.

Existen varias técnicas que podrían ser usadas para impedir los problemas relacionados con la difusión de oxígeno en el electrolito y la química parásita del ánodo de litio:

**1) Las capas protectoras sobre el litio metálico.** La mayoría de los solventes usados en las baterías de Litio-aire no forman un SEI (solid electrolyte interphase) estable sobre el litio. Pero algunos aditivos como por ejemplo  $\text{LiNO}_3$  pueden ayudar a formar una interfase SEI estable en esos solventes.(65, 70, 71). Por otro lado, algunos grupos han estabilizado el litio metálico almacenándolo en el carbonato de propileno por lo menos durante tres días antes de ciclarlo en otro solvente como DMSO.(36)

**2) Celda con dos compartimientos.** Esa estrategia implica que el ánodo y el cátodo están separados por la membrana sólida que permite la libre difusión de iones  $\text{Li}^+$ , y cada uno de los compartimientos se llena con la solución que mejor funciona para el ánodo de litio o el cátodo poroso de oxígeno.(105, 110)

**3) Sustitución de litio con otro material de ánodo.** La factibilidad del uso de carbonos duros (HC, hard carbons) prelitados como material del ánodo con un electrolito basado en diglima fue examinado por Hirshberg et al.(111). Por otro lado, el grupo de Gasteiger ha estudiado los ánodos de LTO/LLTO para las baterías de Litio-aire(105, 112)

En este capítulo, mostramos los resultados usando titanato de litio litiado para sustituir el litio metálico y evitar las reacciones parásitas relacionadas con su uso, y para poder evaluar de mejor manera la falla del funcionamiento de la batería asociada al cátodo y el electrolito.

Se demostró que aún con el ánodo de titanato de litio litiado, la batería posee una retención de carga muy baja. Por eso hemos concluido que el electrolito y el cátodo, aun en ausencia de ánodo de litio, son los principales responsables de la baja capacidad de ciclado de la batería, de acuerdo a la mayoría de los resultados reportados anteriormente. Eso significa que la comprensión profunda de la electroquímica fundamental de batería de Litio-aire es esencial, así como los mecanismos de electrorreducción de oxígeno durante la descarga y su evolución durante la carga, así como los mecanismos de la descomposición de los materiales del solvente, electrolito y cátodo.

Para concluir, en este capítulo hemos visualizado el desafío de la batería de Litio-aire mostrando experimentos de carga y descarga y hemos justificado la necesidad de estudios fundamentales de las reacciones reducción y evolución de oxígeno.

# CHAPTER 4. Cathode reaction: mechanistic insights into oxygen electroreduction and evolution reactions.

## 4.1. Introduction.

Due to the challenges facing Li-air battery technology, as was shown in the previous chapter, a detailed understanding of O<sub>2</sub> reduction and evolution reactions (ORR and OER) mechanisms in aprotic solvents, and its dependence on the nature of solvent, cation, anion and other variables, is of paramount importance.

ORR in organic solvents, namely acetonitrile, dimethylformamide, dimethylsulfoxide and pyridine, in the presence of large alkylammonium salts were studied in 1982 by Sawyer et al.(122), and the formation of stable and reversible O<sub>2</sub><sup>-</sup>/O<sub>2</sub> electrochemical couple has been shown by the means of cyclic voltammetry. Later on, after the introduction of non-aqueous Li-air battery in 1996 (31), the studies of ORR in organic solvents were partially repeated and extended to more solvents, which could potentially serve as electrolytes in non-aqueous Li-air battery: dimethyl sulfoxide (DMSO), acetonitrile (ACN), dimethoxyethane (DME), and tetraethylene glycol dimethyl ether (TEGDME)(86).

However substitution of alkylammonium salts with Li<sup>+</sup> has shown that the presence of Li<sup>+</sup> alters significantly the O<sub>2</sub> reduction mechanism, and that superoxide anion is not stable in the presence of Li<sup>+</sup> and chemically or electrochemically undergoes further reduction to peroxide anion O<sub>2</sub><sup>2-</sup> (85, 86).

In 2012 (the beginning of this doctoral thesis research) there was hardly any knowledge of the O<sub>2</sub>/Li<sub>2</sub>O<sub>2</sub> redox couple in the aprotic media. However now (in 2017), after years of intense fundamental research all over the world, a deeper insight into the chemistry underpinning O<sub>2</sub> cathode was gained. Around 2014-2015 several research groups, including ours, have suggested a new vision on the ORR mechanism (solution versus surface mechanism) (59, 73, 123) which will be discussed in more details later in the chapter. In the current chapter we will also discuss the ORR and OER in various non-aqueous solvents: DMSO, ACN and PYR<sub>14</sub>TFSI ionic liquid, the effect of Li<sup>+</sup> cation concentration, and explain the reaction mechanism and its steps from the

point of view of new unified mechanism of the ORR based on the solubility of  $\text{LiO}_2$  intermediate.

#### 4.2. ORR in non aqueous organic solvents without $\text{Li}^+$ .

Studies of the ORR in several potential electrolytes for Li-air battery without addition of  $\text{Li}^+$  salts have all shown similar results: formation of stable reversible  $\text{O}_2^-/\text{O}_2$  couple (1 electron reaction), observed by the means of cyclic voltammetry and RDE. Such results have been shown in numerous organic solvents, to mention some:

- 1) acetonitrile, dimethylformamide, dimethylsulfoxide, pyridine in the presence of tetraethylammonium perchlorate, on C, Au and Pt (124)
- 3) dimethoxyethane in the presence of tetrabutylammonium  $\text{TBA}^+$ , on glassy carbon (125)
- 4) DME and TEGDME, ACN, DMSO with  $\text{TBA}^+$  on GC (86)

In the figure 4.1 the cyclic voltammeteries performed in the oxygen saturated 0.1 M  $\text{TBAPF}_6$  solution in DMSO at different scan rates are shown. In agreement with the previous studies, the formation of reversible  $\text{O}_2/\text{O}_2^-$  couple is observed. The number of electrons was determined as  $n=1$  from the simplified Randles–Sevcik equation, if the temperature is assumed to be 25 °C:

$$i_p = k \cdot n^{3/2} \cdot A \cdot D^{1/2} \cdot v^{1/2} C$$

In this equation,  $i_p$  is a peak current,  $k$  is a constant of  $2.69 \times 10^5$  with units of  $\text{C mol}^{-1} \text{V}^{-1/2}$ ,  $n$  is the number of electrons,  $A$  is the electrode area ( $\text{cm}^2$ ),  $D$  is the oxygen diffusion coefficient ( $\text{cm}^2 \text{s}^{-1}$ ) and  $v$  is the scan rate ( $\text{V s}^{-1}$ ). Number of electrons  $n$  is determined from a slope of a plot peak current versus square root of a scan rate.

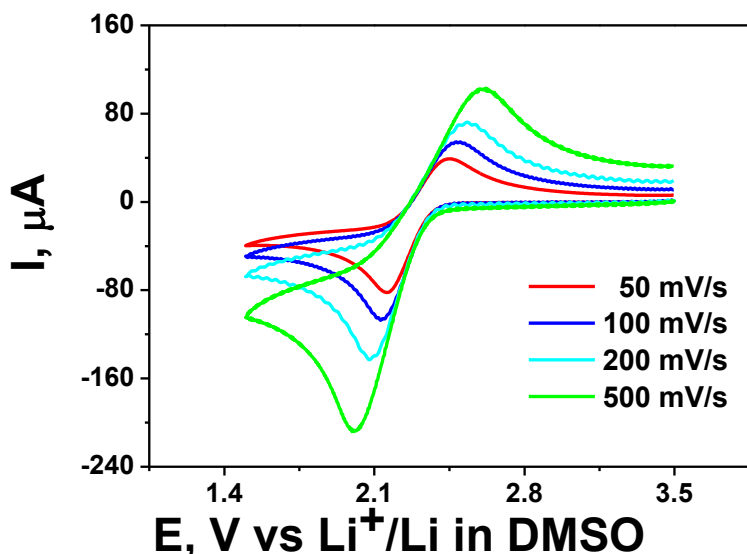


Figure 4.1. Cyclic voltammeteries performed in 0.1 M TBAPF<sub>6</sub> in DMSO, saturated in O<sub>2</sub>. CVs at scan rates 50, 100, 200 and 500 mV/s.

In the figure 4.2 the RRDE cyclic voltameteries of the same system are shown. The disc current corresponds to the ORR and the ring current is kept at fixed potential of 0 V vs Ag<sup>+</sup>/Ag (3 V vs Li/Li<sup>+</sup>) and detects soluble superoxide species in the solution.

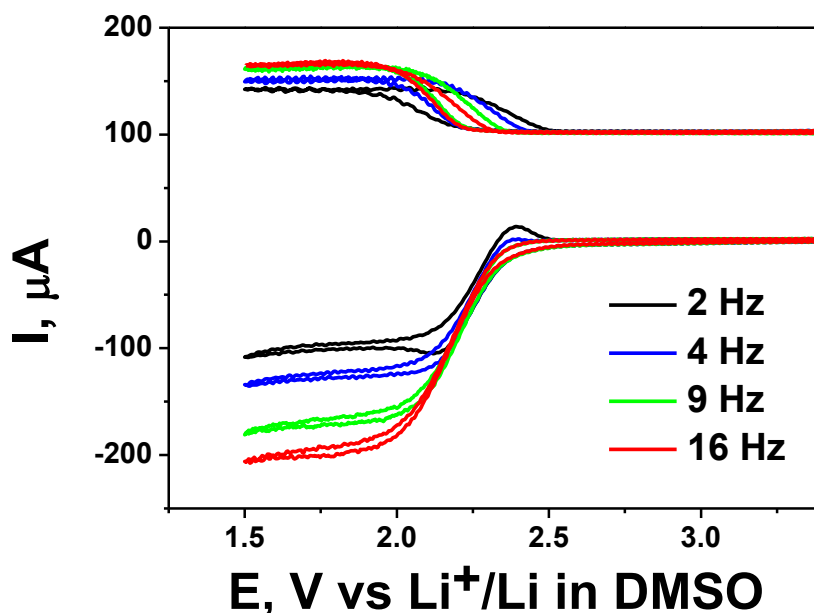
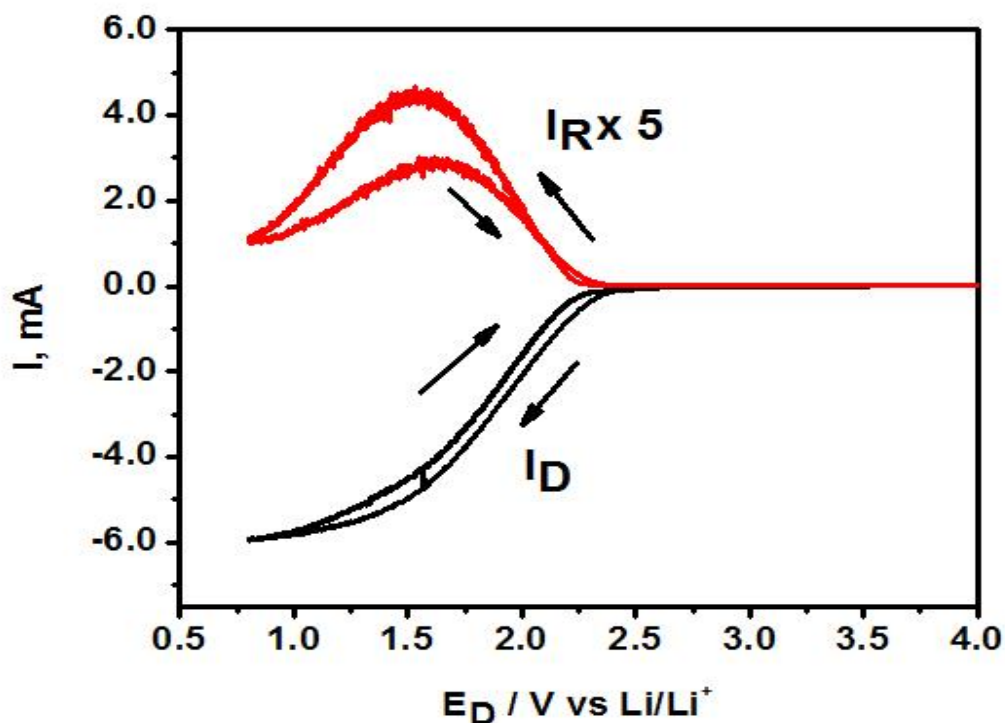


Figure 4.2. RRDE cyclic voltameteries performed in 0.1 TBAPF<sub>6</sub> in DMSO, saturated with O<sub>2</sub>, with rotation rates at 2, 4, 9 and 16 Hz. Ring electrode was kept at a stable potential of 0 V vs. Ag<sup>+</sup>/Ag reference electrode (3.5 V versus Li<sup>+</sup>/Li). Ring current is normalized to No = 0.22.

Figure 4.3 also depicts the rotating ring disk electrode currents vs. disk potential curves in the oxygen saturated 0.1 M TEAClO<sub>4</sub> in ACN. The disk current shows the oxygen reduction reaction and presents little hysteresis and approaches a limiting value while the ring current collecting O<sub>2</sub><sup>-</sup> under convective-diffusion exhibits a maximum at -1.6 V. The ring current corresponds to superoxide oxidation at 3 V vs. Li/Li<sup>+</sup> under convective diffusion conditions.

For the both ACN and DMSO, at the disk electrode the possible potential dependent sequential reactions are:



**Figure 4.3.** O<sub>2</sub> reduction on a GC disk electrode in O<sub>2</sub> (1 atm) saturated 0.1 M TEAClO<sub>4</sub> in purified CH<sub>3</sub>CN at W = 16 Hz and scan rate of 0.1 V s<sup>-1</sup>, ring current at E<sub>R</sub> = 3 V. The inset depicts a CV of O<sub>2</sub> reduction under unstirred conditions. Disc area is equal to A<sub>D</sub> = 0.2 cm<sup>2</sup>.

With two one-electron superimposed waves (see below). The bulky tetraalkylammonium cation stabilizes  $O_2^-$  and  $O_2^{2-}$  by cation–anion pairing (86). The convective-diffusion  $O_2$  reduction current,  $I_L$ , in figures 4.2 and 4.3. can be described by the Levich equation (126):

$$I_L = 0.62nFAD_{O_2}^{2/3}v^{-1/6}C_{O_2}\omega^{1/2} \quad (4.3)$$

where  $F$  is the Faraday constant,  $n$  is the number of electrons per  $O_2$  molecule,  $A$  is the electrode geometric area,  $D_{O_2}$  is oxygen diffusion coefficient in ACN or DMSO,  $C_{O_2}$  is the oxygen concentration,  $v$  is the kinematic viscosity, and  $\omega$  is the angular rotation rate of the electrode (rad/s).

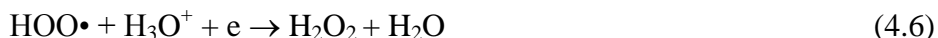
At the ring electrode ( $E_R = 3 \text{ V vs Li/Li}^+$ ) the soluble superoxide radical anion is oxidized under convective-diffusion conditions:



Considering  $No = 0.22$ , the ring current is only a fraction of the expected value ( $No \cdot I_D$ ); therefore a fraction of the superoxide formed at the disk electrode should decompose in transit to the ring electrode. In the presence of traces of water (50 ppm in the  $CH_3CN$  represents 2–3 mM as compared to  $O_2$  solubility 8.1 mM and thus superoxide concentration) the fast reaction ( $k_2 > 10^4 M^{-1} s^{-1}$ ):



yields  $H_2O_2$ . Also with traces of  $H_3O^+$  the reaction:



with  $E^{o'} = 0.8 \text{ V}$  would also account for the loss of superoxide.

It had been shown earlier that protic contaminants of the solvents lead to decomposition of  $O_2^-$  to  $H_2O_2$  and  $O_2$  (122). Therefore an increased attention is required to control the protic contaminations of the organic solutions, especially those containing highly hydrophilic  $Li^+$  cations. As an example, commercially available anhydrous acetonitrile contains around 10-20 ppm of  $H_2O$  which corresponds to 0.43-0.86 mM/l, while the  $O_2$  solubility in acetonitrile is 8.1

mM/l. This means that in purified anhydrous solution of acetonitrile, the concentration of protic contaminants can reach up to 10% of concentration of dissolved oxygen, therefore it can be suggested that 10% of superoxide formed, will undergo decomposition as a result of protonation. Also it is worth mentioning that reported values of water content usually correspond to the pure solutions, however addition of  $\text{Li}^+$  salts is likely to result in increased water content of the solutions due to its high hydrophilicity.

### 4.3. ORR and OER in non aqueous organic solvents in the presence of Li<sup>+</sup>.

As it has been mentioned before, substitution of large tetraalkylammonium cations (TEA<sup>+</sup> or TBA<sup>+</sup>) by a small acidic Li<sup>+</sup> cation alters significantly the mechanism of the ORR in non-aqueous solvents. First studies of ORR in the presence of Li<sup>+</sup> were performed by Abraham's group in 2010, who used the HSAB theory to explain the ORR mechanism. According to them (85, 86), the reduction of O<sub>2</sub> in the presence of Li<sup>+</sup> salts in organic solvents occurs in the following steps:

- 1) Formation of superoxide:



Formation of LiO<sub>2</sub> is a 1-electron process; however LiO<sub>2</sub> is not a stable compound and decomposes to form lithium peroxide. First the Hard Soft Acid Base theory (HSAB) was used to explain the stability of compounds. In this theory, the hardness of acids is evaluated but its Lewis acidity and the hardness of base – by its Guttmann donor number. In one work, the acidity of the cations was evaluated based on <sup>13</sup>C NMR chemical shifts and spin-lattice relaxation times <sup>13</sup>C=O in the solutions of propylene carbonate (PC) (98). According to the HSAB theory, soft bases form stable compounds with soft acids, and hard bases form stable compounds with hard acids. Generally, the lower radius of the ion and higher charge, the higher is its charge density, which means that acidity of cations (basicity of anions) is stronger.

Later (around 2014-2015) a more complete theory to explain ORR was developed, that will be discussed in much detail at the end of this chapter.

It is also worth noting that superoxide radical anion O<sub>2</sub><sup>-</sup> formed during the first O<sub>2</sub> reduction step is a strong reducing agent and was believed to be responsible for electrolyte decomposition.

- 2) Chemical decomposition of superoxide to form more stable peroxide:



- 3) Electrochemical reduction of superoxide (if it has not been completely decomposed chemically):



4) And ultimately possible reduction to lithium oxide:



However the cell potential is usually cut at 2 V vs. Li/Li<sup>+</sup> and reduction to lithium oxide does not occur normally in Li-O<sub>2</sub> cells, with lithium peroxide being the main theoretical discharge product as reported in numerous works.

The steps of the ORR in the presence of Li<sup>+</sup> are schematically presented on the figure 4.4.

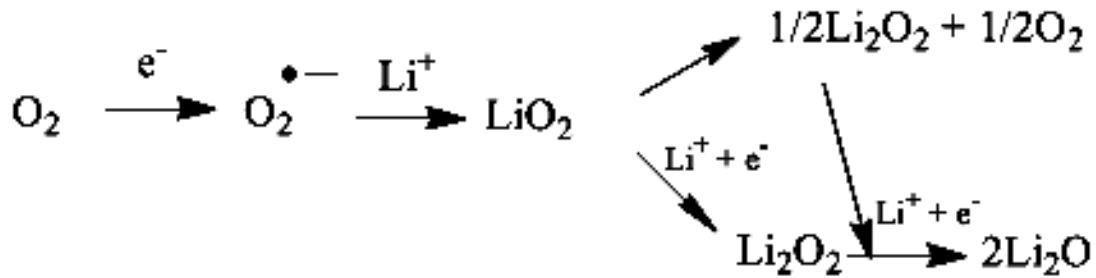
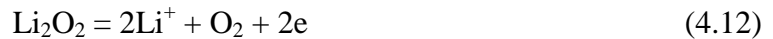


**Figure 4.4. Scheme of oxygen reduction process (32).**

Reaction is irreversible, and anodic decomposition of lithium oxides products occurs only at high overvoltages (with the exact overvoltage being a topic of debate currently) according to following reactions:



We have used the RRDE as an excellent technique to get insight into ORR mechanism, because of the possibility to detect the soluble superoxide anion (if formed) at the ring electrode, which is shown schematically on the figure 4.5.

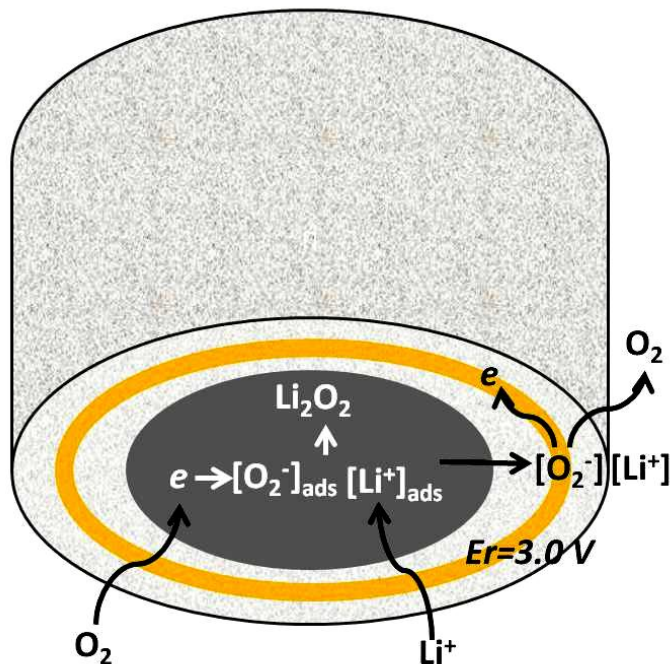


**Figure 4.5. Schematic representation of the use of RRDE technique in the study of ORR in  $Li^+$  containing non-aqueous solutions.**

The expected yield of superoxide at the ring electrode is only dependent on the geometry of the RRDE unless  $O_2^-$  can undergo decomposition processes. We have studied the ORR mechanism using the RRDE technique in ACN, DMSO and  $PYR_{14}TFSI$ : with and without  $Li^+$  salts, coupled to DEMS and EQCM. This allowed us to analyze the lithium peroxide formation reaction and to contribute to the development of the surface-solution model of the ORR.

In our hands, the RRDE has failed to detect (zero ring current) soluble  $O_2^-$  in the  $ACN+LiClO_4$  based electrolyte for the salt concentration above 1 mM. This implies that either solution soluble  $O_2^-$  is not formed at GC disk in  $Li^+$  bearing electrolytes of comparable concentration to  $O_2$  solubility, or it undergoes rapid dismutation to yield insoluble  $Li_2O_2$  in ACN.

However, adding 10  $\mu M$   $LiClO_4$  to the tetraethyl ammonium perchlorate solution,  $I_D$  is much smaller with a shoulder at 2.5 V and a peak at 1.9 V as depicted in figure 4.6 with surface passivation in the reverse scan. Surprisingly a non zero  $I_R$  is only a very small fraction of the disk current (i.e. 1–2  $\mu A$  vs 400  $\mu A$ ) but follows the  $I_D$  vs.  $E_D$  curve shape with the shoulder and the peak (127).

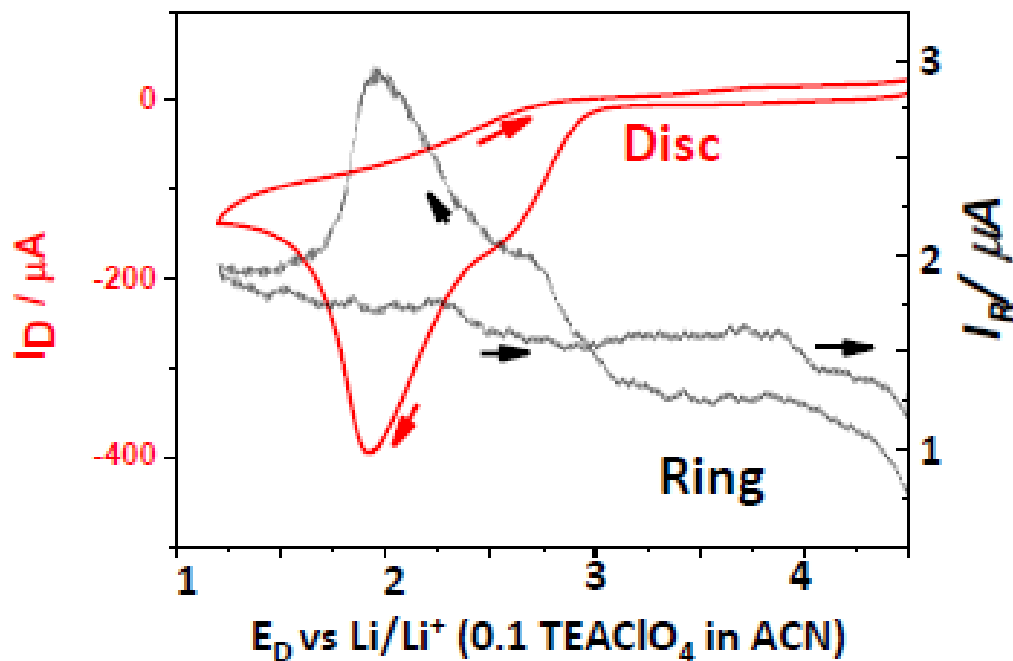


**Figure 4.6.** O<sub>2</sub> reduction on a GC/Pt RRDE in O<sub>2</sub> saturated 0.1 M TEAP in purified CH<sub>3</sub>CN containing 10 μM LiClO<sub>4</sub> at  $W = 9$  Hz and scan rate  $0.1 \text{ V s}^{-1}$ . Ring current at  $E_R=3 \text{ V}$ .  $A_D = 0.2 \text{ cm}^2$ .

In 10 μM LiClO<sub>4</sub> the concentration of Li<sup>+</sup> ions is some 800 times less than that of dissolved oxygen, and 10<sup>4</sup> times less than (TEA<sup>+</sup>), therefore the capacity of Li<sup>+</sup> ions in the weakly coordinating solvent acetonitrile to unstabilize LiO<sub>2</sub> by disproportionation into Li<sub>2</sub>O<sub>2</sub> and O<sub>2</sub> is extremely high.

The competition of I) two sequential one-electron transfer steps with intermediate superoxide and II) disproportionation of soluble superoxide into O<sub>2</sub> and insoluble Li<sub>2</sub>O<sub>2</sub> may determine the ability to charge-discharge the lithium–air battery. While the former heterogeneous electrochemical reactions limit the amount of insoluble Li<sub>2</sub>O<sub>2</sub> to monolayer or few layers due to tunneling distance and diffusion of Li<sup>+</sup> and O<sub>2</sub> limitations, precipitation of Li<sub>2</sub>O<sub>2</sub> from the solution adjacent to the cathode may lead to the formation of bulky deposits resulting in higher discharge capacity.

To sum up, we have shown with RRDE experiments in acetonitrile based electrolytes that small additions of  $\text{Li}^+$  can operate in opposite directions on the kinetics of the ORR by strongly affecting the stability of the  $\text{O}_2^-$  with respect to  $\text{O}_2$  and insoluble  $\text{Li}_2\text{O}_2$ .

The electrochemical behavior of the ORR in  $\text{Li}^+$  ion containing DMSO electrolyte shows cathodic currents that reach a peak which increases with rotating frequency but are below the convective-diffusion Levich current.

Figure 4.7 depicts the cyclic voltammetry of a Au electrode in oxygen saturated 0.1 M  $\text{LiPF}_6$  solution at a sweep rate of 100 mV/s when the electrode potential was linearly scanned between 4.7 to 1.9 V at 100 mV/s. In the reducing sweep current maxima are apparent with further passivation of the electrode.

The corresponding convective-diffusion soluble superoxide oxidation current at the Au ring electrode simultaneous to the ORR is shown in the upper part of figure 4.7.

Both disk and ring currents increase with rotation frequency and ring current maxima at 1.8 V is observed.

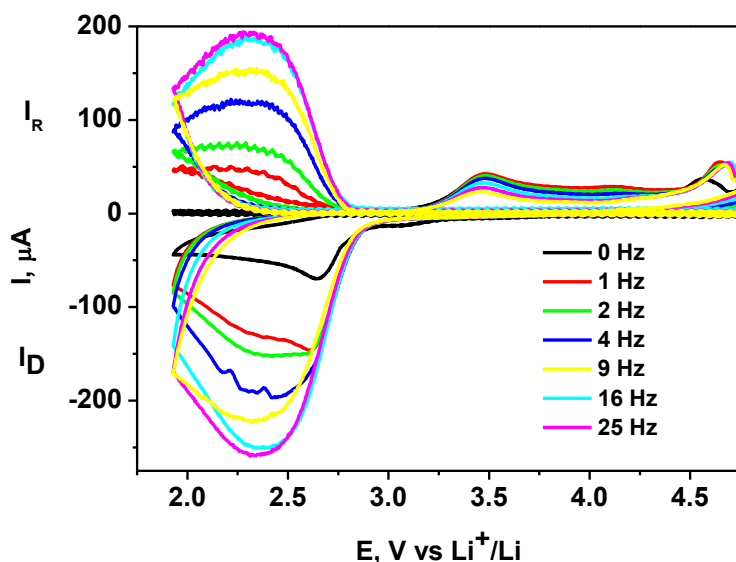
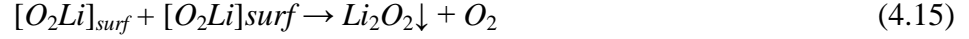


**Figure 4.7. RRDE CVs in 0.1 M  $\text{LiClO}_4$  in DMSO, saturated in  $\text{O}_2$ , rotated at 0, 1, 2, 4, 9, 16, 25 Hz.**

The ring current maxima indicates that the surface concentration of soluble  $O_2^-$  increases the larger the ORR overpotential and then decreases due to either disproportionate or a two electron transfer to  $O_2$  from the electrode, according to the accepted mechanism (36, 53):



Since the ORR product  $Li_2O_2$  is insoluble, the blocking of electron transfer at the electrode surface is observed in the reverse scan both on disk and ring electrodes.

We have investigated the accumulation and removal of oxygen reduced species from the electrode surface by exploring different cathodic and anodic potential windows, respectively.

Figure 4.8 depicts various cathodic potential windows performed in 0.1 M  $LiPF_6$  in DMSO. Notably the ring disc always detects soluble superoxide, which at some point reaches its peak and then diminishes in the same way as disc current. At very low overvoltages the superoxide formation is observed, however no anodic peaks are present meaning that insoluble lithium peroxide is not formed yet. However when opening the disc potential window to the higher overvoltage, the two anodic peaks start to appear which correspond to the lithium peroxide and/or parasitic chemistry (the parasitic reactions will be discussed in more details in chapter 6).

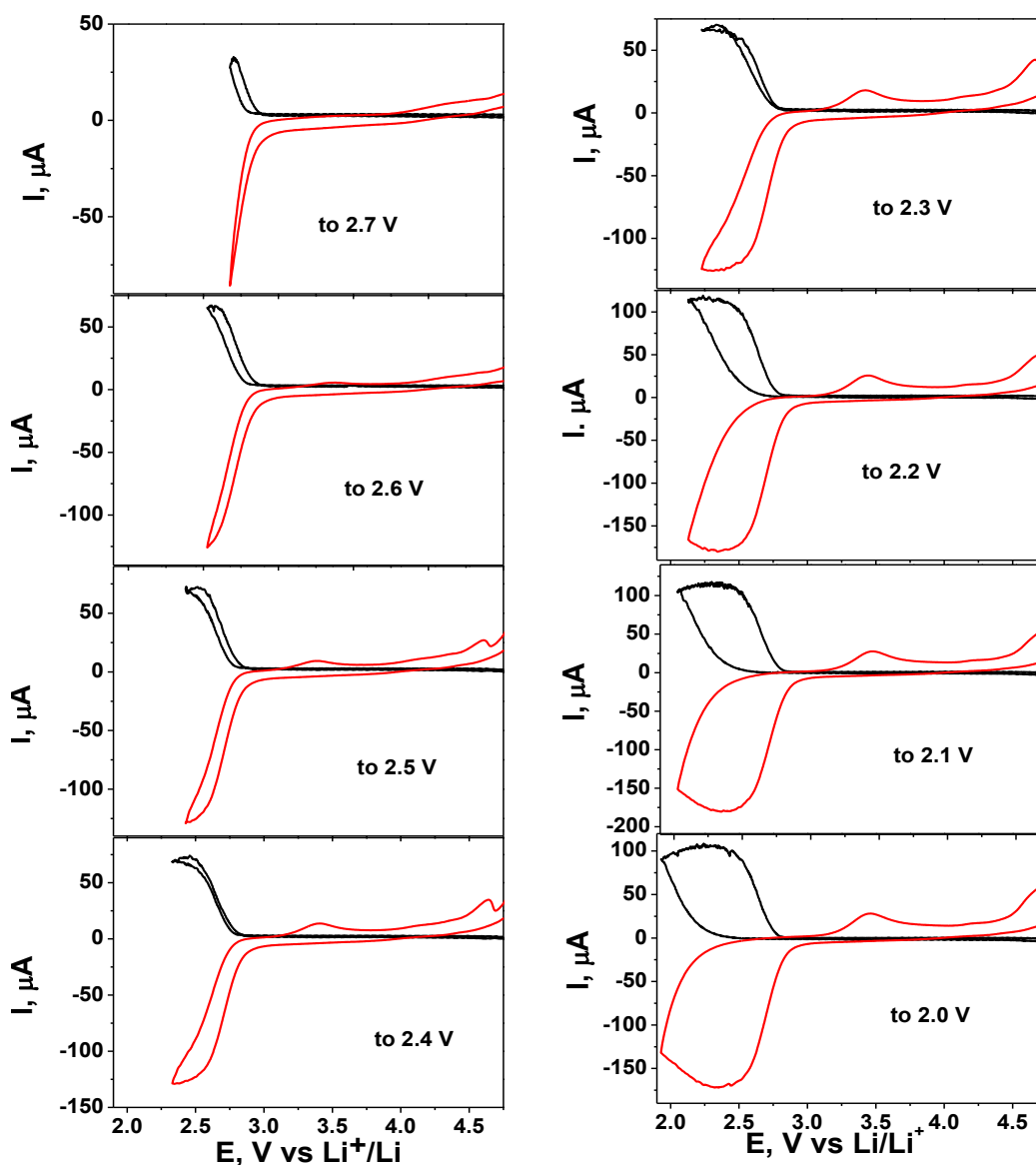


**Figure 4.8. RRDE CVs in 0.1 LiClO<sub>4</sub> in DMSO, O<sub>2</sub> saturated, at rotation 9 Hz.  
Effect of the cathodic voltage limit on the ORR: from 2.7 to 2.0 V.**

The removal of oxygen reduced species from the electrode surface by exploring different anodic potential windows is shown in figure 4.9. When opening the potential window to 4.7 V for 10 seconds (panel A), the second potential scan shows complete recovery of both disk and Au ring currents. Panel B shows that starting the potential sweep at 3.8V after a 10 second oxidation, subsequent lower cathodic currents are observed at disk and ring electrodes because of partly blockage by remaining oxygen reduction products on the surface. Finally, if we restrict the

positive potential limit to 3V for 10 seconds, the GC disk electrode surface is completely blocked with negligible disk and ring currents.

The oxidation and removal of  $\text{LiO}_2$  and  $\text{Li}_2\text{O}_2$  and solvent and electrolyte decomposition products extends over a wide potential range as can be seen from the anodic current in figure 4.9 A due to side reactions of  $\text{Li}_2\text{O}_2$  with the solvent and electrolyte salt.

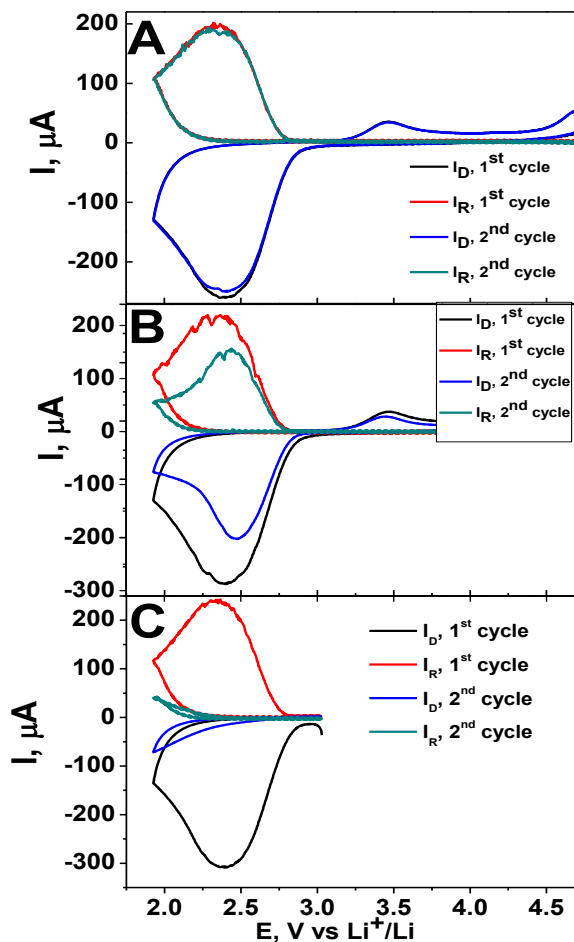


**Figure 4.9. RRDE CVs in 0.1  $\text{LiClO}_4$  in DMSO,  $\text{O}_2$  saturated, 9 Hz. Effect of the anodic voltage limit on the OER.**

#### 4.4. Lithium ion concentration effect in PYR<sub>14</sub>TFSI ionic liquid for Li-O<sub>2</sub> battery cathodes.

Ionic liquids (ILs) are promising electrolytes for metal-air batteries since they are non volatile, non flammable and liquid at room temperature with high oxygen solubility, and high stability particularly for Li-O<sub>2</sub> (60, 61) and Na-O<sub>2</sub> (128-130) batteries. One of the most widely investigated ILs for metal-O<sub>2</sub> batteries is N-butyl-N-methylpyrrolidinium bis(trifluoromethylsulfonyl)imide (PYR<sub>14</sub><sup>+</sup>TFSI also denominated [C4mpyr][TFSI].(131)

In ionic liquids, including PYR<sub>14</sub>TFSI, in the absence of protons and alkali metal ions, the reversible formation of O<sub>2</sub>/O<sub>2</sub><sup>-</sup> couple is observed (131-137) due to the stabilization of superoxide radical ion by IL cation like the tetralkyl ammonium cations in aprotic organic solvents. However, the ORR in ionic liquids changes in the presence of alkali metal ions, especially in the presence of the small Lewis acid Li<sup>+</sup> cation(138, 139). Allen et al.(87, 98) described the mechanism of ORR in PYR<sub>14</sub>TFSI in 25 mM Li<sup>+</sup> as follows:



Following for the oxygen evolution reaction (OER) in the anodic sweep:



Herranz et al. used the rotating ring disc electrode (RRDE) experiments to quantify the stability of PYR<sub>14</sub>TFSI in the presence of superoxide anion, but without Li<sup>+</sup> ion (140). The stability of PYR<sub>14</sub><sup>+</sup> studied by FTIR will be reported in details in chapter 6.

Lodge et al. have also reported a detailed characterization of the reduction of the ORR in pure PYR<sub>14</sub>TFSI: reversible reduction of O<sub>2</sub> to O<sub>2</sub><sup>-</sup> and O<sub>2</sub><sup>-</sup> to O<sub>2</sub><sup>2-</sup> take place at potentials 2.1 V and 0.8 V vs. Li<sup>+</sup>/Li, respectively. They found that in the presence of very low concentration of Li<sup>+</sup> such as 1 mM, the ORR takes place in two distinct peaks: 2.5 V (involving O<sub>2</sub> and Li<sup>+</sup>) and 1.9 V

(involving  $\text{PYR}_{14}^+$  and  $\text{O}_2$ ). However, at higher  $\text{Li}^+$  concentration, i.e. 0.3 M the ORR starts at the same potential as for low  $\text{Li}^+$  concentration and leads to complete electrode passivation by insoluble  $\text{Li}_2\text{O}_2$ , estimated to be 7 monolayers of a uniform film (139).

We report the use of RRDE technique to study the  $\text{PYR}_{14}\text{TFSI}$  ionic liquid with various  $\text{Li}^+$  concentrations from 0 to 50 mM, complemented by DEMS and EQCM, and discuss the mechanism of ORR in this ionic liquid.

Figure 4.10 depicts cyclic voltammetry of an Au electrode in  $\text{PYR}_{14}\text{TFSI} + \text{LiTFSI}$  at different  $\text{Li}^+$  concentrations, 0-50 mM, at  $50 \text{ mV}\cdot\text{s}^{-1}$ . In pure ionic liquid  $\text{PYR}_{14}\text{TFSI}$  a quasi-reversible one-electron wave is observed with a mid-peak potential of 2.04 V, while a cathodic ORR peak at 1.91 V is in good agreement with previous reports.(98, 139) In the reverse scan an oxidation peak at 2.16 V corresponds to the oxidation of superoxide at the electrode surface which has not diffused away from the electrode surface, i.e. the reaction  $\text{O}_2/\text{PYR}_{14}^+\text{O}_2^-$  is reversible.

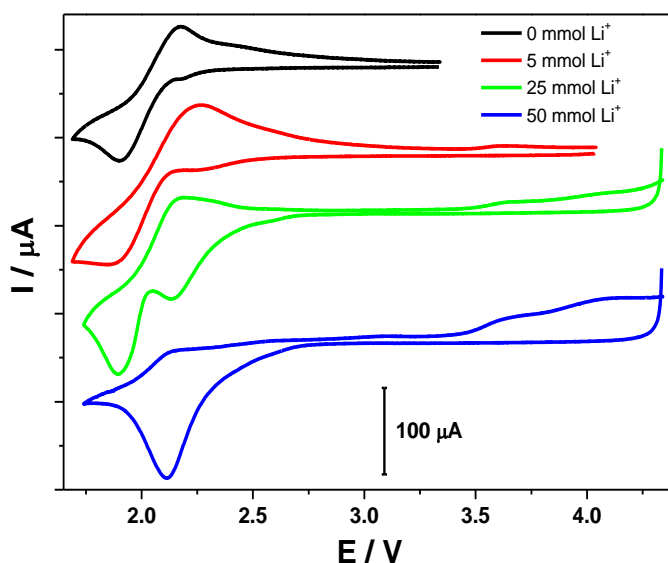


**Figure 4.10: Cyclic voltammetry experiment of  $\text{O}_2$  saturated in  $\text{PYR}_{14}\text{TFSI} + \text{LiTFSI}$  at different  $\text{Li}^+$  concentrations 0-50 mM at  $50 \text{ mV}\cdot\text{s}^{-1}$ .**

As we introduce 1 to 25 mM  $\text{LiTFSI}$  in the ionic liquid the quasi reversible peak is still observed but a second oxygen reduction peak at more positive potential, i.e. 2.15 V is now present due to

the formation of  $\text{Li}^+\text{O}_2^-$  ion pair. The  $\text{O}_2/\text{LiO}_2$  redox couple exhibits a more positive potential than  $\text{O}_2/\text{PYR}_{14}^+\text{O}_2^-$  due to the effect of a better acceptor cation.(141)

At 50 mM LiTFSI a single cathodic peak at 2.15 V is observed and the re-oxidation superoxide peak disappears, while the anodic current is observed above 3.4 V from 25 mM lithium ion concentration. Thus, the  $\text{O}_2/\text{PYR}_{14}^+\text{O}_2^-$  reaction does not contribute to the current at high  $\text{Li}^+$  concentration. Under stirring with a rotating disc electrode system convective-diffusion ORR plateau is observed in figure 4.11 for the lithium free  $\text{PYR}_{14}\text{TFSI}$  and cathodic peaks are present in lithium containing electrolyte.

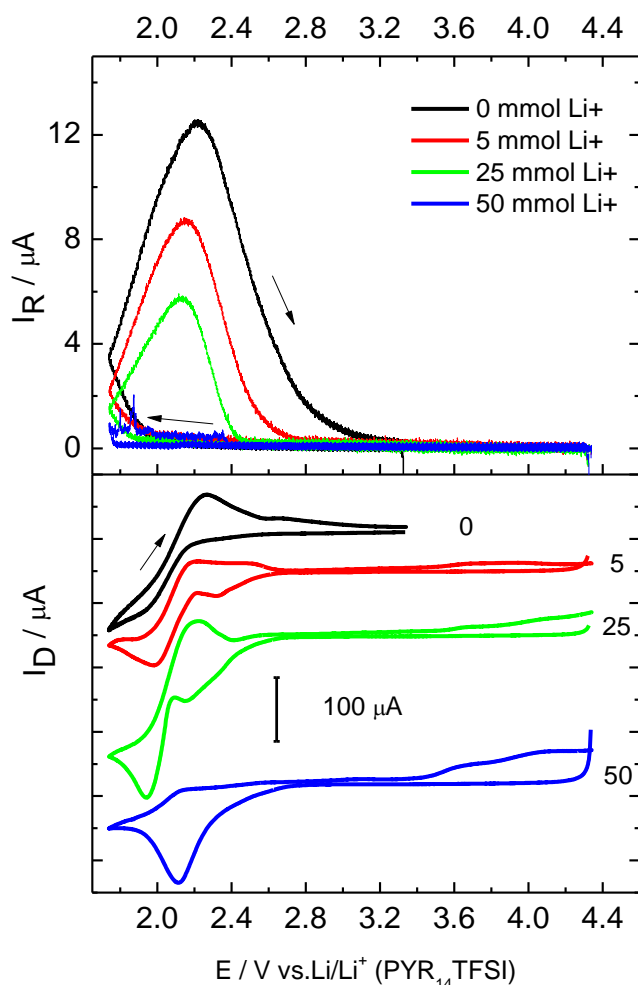


**Figure 4.11.** Au-Au RRDE experiment of  $\text{O}_2$  saturated in  $\text{PYR}_{14}\text{TFSI} + \text{LiTFSI}$  at different  $\text{Li}^+$  concentrations 0-50 mM, 4 Hz,  $50 \text{ mV}\cdot\text{s}^{-1}$ , ring potential 3.0 V,  $A = 0.2 \text{ cm}^2$ ,  $N_o = 0.28$ .

A rotating ring disc electrode study of the ORR in  $\text{PYR}_{14}\text{TFSI}$  containing  $\text{LiTFSI}$  shows that superoxide ion can be detected at the ring electrode downstream the Au disc electrode, see figure 4.11. However the ring electrode response is delayed in time (or potential in the cyclic voltammetry at  $50 \text{ mV}\cdot\text{s}^{-1}$ ) with respect to the ORR onset at the disc electrode. Similar findings have been reported for  $\text{O}_2$  saturated pure  $\text{PYR}_{14}\text{TFSI}$  and have been ascribed to the slow diffusion of  $\text{O}_2^-$  radical ion in the ionic liquid. (140) While the diffusion coefficient for neutral  $\text{O}_2$  in  $\text{PYR}_{14}\text{TFSI}$  is  $2.9 \times 10^{-6} \text{ cm}^2\cdot\text{s}^{-1}$ , (98) superoxide exhibits a negative charge and therefore the diffusion coefficient in the highly charged ionic liquid is much lower, i.e.  $1.1 \times 10^{-7} \text{ cm}^2\cdot\text{s}^{-1}$ . (140)

The slow diffusion of superoxide is also responsible for the positive currents in the back scan due to the oxidation of superoxide radical that has not completely diffused away from the disc electrode surface at positive enough potential for its anodic oxidation.

The main feature of Figure 4.11 is the strong effect of lithium ion concentration in the ionic liquid: The yield of superoxide ion detected at the ring electrode decreases and the disc current pre-peak at 2.15 V increases the higher the  $\text{LiTFSI}$  concentration. Therefore insoluble  $\text{Li}_2\text{O}_2$  becomes the main interfacial electrode reaction product at 50 mM  $\text{LiTFSI}$  with no detection of superoxide at the ring electrode.

Notice that the solubility of oxygen in  $\text{PYR}_{14}\text{TFSI}$  is 13.6 mM (131), and therefore the  $\text{O}_2^-$  concentration is much less than the concentration of the ionic liquid cation  $\text{PYR}_{14}^+$ , so that ion pairs  $\text{PYR}_{14}^+ \text{O}_2^-$  prevail, but above 25 mM  $\text{Li}^+$ , the ion pair  $\text{Li}^+ \text{O}_2^-$  is more favorably formed due to the strong Lewis acidity of the small  $\text{Li}^+$  cation. However this  $\text{Li}^+ \text{O}_2^-$  ion pair is short lived and disproportionates into  $\text{Li}_2\text{O}_2$ .

Superoxide is the first oxygen reduction product as shown by Frith et. al. (142) who have reported a Raman band at  $1107 \text{ cm}^{-1}$  assigned to superoxide anions during the ORR in  $\text{O}_2$  saturated  $\text{PYR}_{14}\text{TFSI}$  containing 10 mM  $\text{LiTFSI}$ . At low concentration of hard Lewis acid  $\text{Li}^+$  cations and high concentration of soft organic cations  $\text{PYR}_{14}^+$  these can associate to the superoxide ion, and therefore, prevent them from combining to form  $\text{Li}_2\text{O}_2$ . As the  $\text{LiTFSI}$  concentration increases, the main surface reaction product is  $\text{Li}_2\text{O}_2$  as has been shown in this electrolyte by ex-situ the  $805 \text{ cm}^{-1}$  Raman spectroscopy band characteristic of lithium peroxide

(143) and confirmed in the present study by the EQCM mass increase in Figure 4.12. In spite of the noisy data due to the high viscosity of the ionic liquid, there is a clear gravimetric evidence of formation of insoluble product as expected for  $\text{Li}_2\text{O}_2$  at low overpotentials. Furthermore, notice that the mass increases at the peak due to formation of  $\text{Li}^+\text{O}_2^-$  and possible further disproportionation.

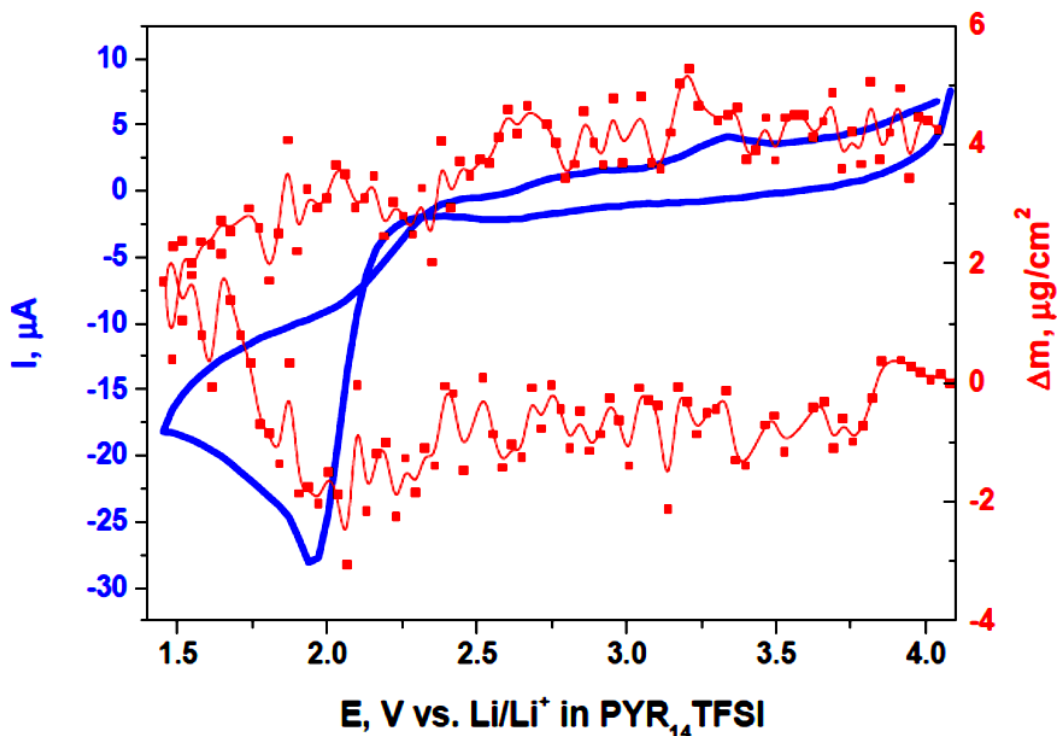


**Figure 4.12. Cyclic voltammetry experiment of  $\text{O}_2$  saturated  $\text{PYR}_{14}\text{TFSI} + 0.18 \text{ M LiTFSI}$  at  $50 \text{ mV/s}$  and  $10 \text{ MHz}$  EQCM mass increase ( $\Delta m/A$ ) simultaneous to the cyclic voltammetry.**

We notice that the reference  $\text{Li}_2\text{Mn}_2\text{O}_4/\text{LiMn}_2\text{O}_4$  electrode is  $2.61 \text{ V vs. Li/Li}^+$  in  $\text{PYR}_{14}\text{TFSI}$ .

In cyclic voltammetry both potential and time are convoluted, therefore we have performed constant current steps in the cathodic and anodic directions followed by open circuit potential (OCP). In reduction and oxidation galvanostatic current steps at  $80 \text{ microamps}$  in  $\text{O}_2$  saturated  $50 \text{ mM LiTFSI} + \text{PYR}_{14}\text{TFSI}$  we recorded the Au electrode potential in the lower panel of Figure 4.13, the total quartz crystal admittance  $\omega L$  (in the  $534.00 \text{ } \Omega$ ) and the viscoelastic losses  $R \sim 2200 \text{ } \Omega$  due to the high viscosity of the ionic liquid. For comparison, the impedance contribution

of the DMSO in contact with the quartz crystal is  $Z_L^\square = 326 \Omega$  while for the 0.1 M LiPF<sub>6</sub>/DMSO with the 10 MHz quartz crystal mounted with the o-ring it was found experimentally 460  $\Omega$ .

Upon reducing oxygen at  $-80 \mu\text{A}$  the oxygen cathode electrode potential drops and  $\omega L$  increases by 88  $\Omega$  ( $4.6 \times 10^{-8} \text{ g}/\Omega$ ), 4  $\mu\text{g}$  as expected for the deposition of Li<sub>2</sub>O<sub>2</sub> on the Au electrode. Notice that there is almost no change in the R parameter.

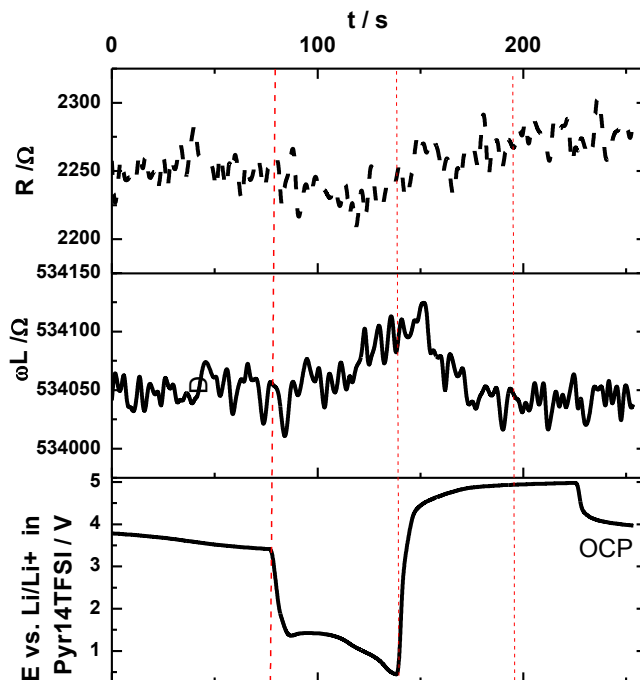


**Figure 4.13. Chronopotentiometry of O<sub>2</sub> saturated PYR<sub>14</sub>TFSI + 50 mM LiTFSI and simultaneous 10 MHz EQCM complex admittance  $\omega L$  and R of the BVD equivalent circuit.**

When an anodic current step of  $+80 \mu\text{A}$  is applied, oxidation of the surface takes place and the Au electrode potential goes in the positive direction while  $\omega L$  decreases by almost the same 88  $\Omega$  (4  $\mu\text{g}$ ) returning the mass per unit area to the baseline and continues at that value even at OCP. Taking the total charge in each step of  $\pm 25 \times 10^{-3} \text{ C}/\text{cm}^2$  and the mass variation per unit area  $4 \times 10^{-6} \text{ g}/\text{cm}^2$  we calculate a mass per electron of 15 g which compares to 23 g for Li<sub>2</sub>O<sub>2</sub>. Therefore the EQCM microgravimetry proves the formation of lithium peroxide on the Au surface.

Differential electrochemical mass spectrometry (DEMS) for O<sub>2</sub> ( $q/m = 32$ ) and CO<sub>2</sub> ( $q/m = 44$ ) simultaneous to the ORR and re-oxidation in pure PYR<sub>14</sub>TFSI ionic liquid and in 25 mM LiTFSI

in  $\text{PYR}_{14}\text{TFSI}$  under constant current pulses are shown in Figure 4.14. In both systems  $I_{32}$  mass spectrometric current decreases in the cathodic pulses due to the  $\text{O}_2$  depletion in the ORR. After correction for the mass spectrometry ionic current delay due the transport in our DEMS vacuum setup, i.e.. 22 seconds, the positive  $I_{32}$  current that corresponds oxygen evolution for pure ionic liquid occurs at about 2 V confirming the evidence in the cyclic voltammetry anodic peak during the back scan and the RRDE detection of superoxide. In 25 mM  $\text{Li}^+$  solution in  $\text{PYR}_{14}\text{TFSI}$ , the mass 32 ionic current peak due to superoxide oxidation is smaller.

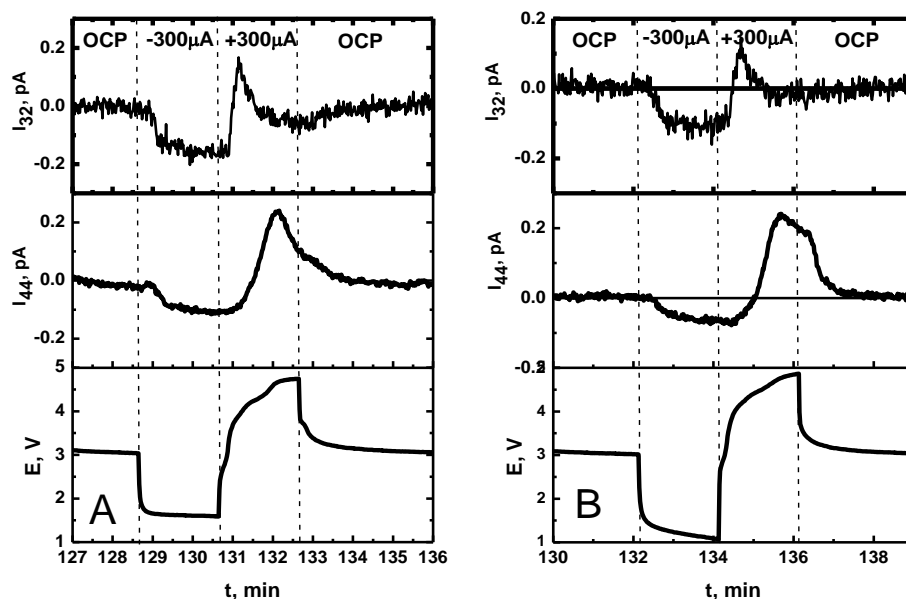


**Figure 4.14. DEMS currents for  $I_{32}$  and  $I_{44}$  respectively and Au electrode potential in  $\text{O}_2$  saturated  $\text{PYR}_{14}\text{TFSI}$  (A) and  $\text{PYR}_{14}\text{TFSI} + 25 \text{ mM LiTFSI}$  (B) for reduction and oxidation pulses at a -300 and + 300  $\mu\text{A}$  respectively .**

It should be noticed that there is no DEMS evidence of  $\text{O}_2$  evolution expected from  $\text{Li}_2\text{O}_2$  oxidation above 3.2 V while anodic currents are observed in figures 4.10 and 4.11. However,  $I_{44}$  mass spectroscopic current due to  $\text{CO}_2$  increases above 4.2 V consistent with the FTIR evidence (144) and the mass loss in the EQCM experiment. Therefore the parasitic reaction of  $\text{Li}_2\text{O}_2$  with the ionic liquid cation is expected to yield surface species that can only be oxidized at high overpotentials.

To conclude, competition of ORR product  $O_2^-$  for the  $PYR_{14}^+$  and the strong Lewis acid  $Li^+$  is reflected in the lower yield of soluble superoxide, EQCM mass increase and the positive shift of the  $O_2/O_2^-$  potential while increasing the  $Li^+$  concentration in the ionic liquid.

#### 4.5. Surface versus solution mechanism: new understanding of ORR.

In 2014-2015, with a much of research effort, appeared more understanding of ORR in aprotic solvents. The new model of ORR has replaced the previously used HSAB theory. Exactly two different models for  $\text{Li}_2\text{O}_2$  formation have been suggested: via solution or surface. The proposed mechanism is schematically shown in the figure 4.15. In high donor number solvents, such as DMSO, a soluble superoxide has been detected in the solution (53, 58, 59), and therefore a mechanism via solution was suggested. While in ACN, where no soluble superoxide is detected on the ring electrode, the surface mechanism is predominant.

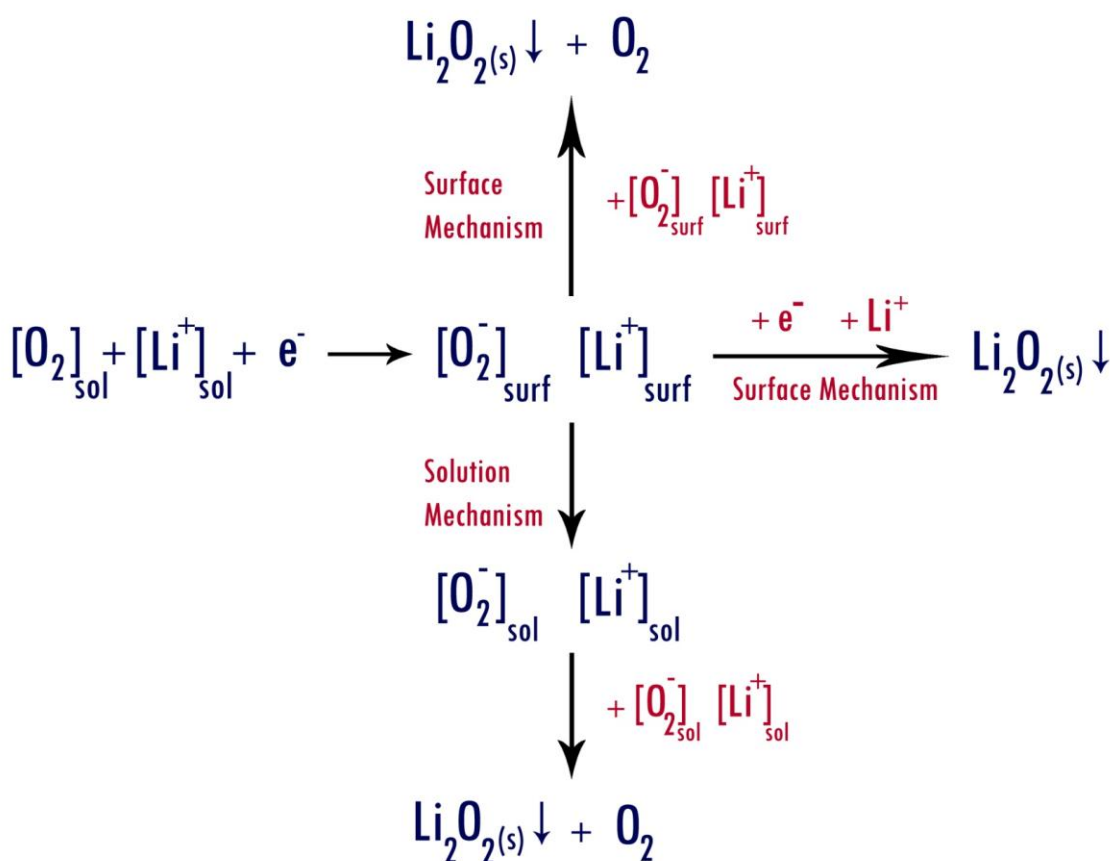


**Figure 4.15. Schematics of the mechanism of ORR in aprotic solvents in presence of  $\text{Li}^+$ : solution vs. surface.**

Also a unified mechanism has been suggested, where the surface and solution mechanism are two limiting cases.(123) This unified model explains the ORR based on the solubility of  $\text{LiO}_2$ , or more precisely on the free energy of the reaction:



To summarize, the reaction mechanism (solution vs. surface) is influenced by many factors:

1) **Nature of solvent: solvent's donor number (DN) and acceptor number (AN)** (59, 73). The higher solvent's DN, the higher its ability to solvate the  $\text{Li}^+$  and therefore stabilize soluble superoxide. This means that solvents with higher DN, such as DMSO, promote solution mechanism, while lower DN number solvents, such as ACN, promote surface mechanism as has been shown earlier in the chapter. The solvation of  $\text{O}_2^-$  is correlated with solvent's AN, however varies to much lower extent than the solvation of  $\text{Li}^+$ , and therefore is not predominant to determine the mechanism.(145)

2) **Nature of lithium salt anion** (146-148). Similarly to the solvent, the ability of salt anion to stabilize the  $\text{Li}^+$  cation would promote the solution-way mechanism. Thus the increasing  $\text{NO}_3^-$  anion concentration was shown to trigger equilibrium to the solution mechanism.(146)

3) **Additives and impurities** (72, 73, 84, 149). Some high DN additives or impurities (such as water traces(73)) in lower DN solvents may solvate preferentially  $\text{Li}^+$  and therefore promote the ORR mechanism via solution. In the next chapter we will show in detail the effect of preferential solvation of the  $\text{Li}^+$  cation.

4) **Current density and potential** (150, 151). Higher discharge current and higher discharge overvoltage both promote faster second electron reduction to form  $\text{Li}_2\text{O}_2$  at the expense of the disproportionation mechanism, therefore would promote a surface-based mechanism over the solution path.

5) **Lithium ion concentration**. As has been shown in this chapter, very low  $\text{Li}^+$  concentration result in superoxide stabilization and therefore also promotes mechanism via solution species.

The discharge mechanism is of paramount importance, because of the shape of non conductive and insoluble  $\text{Li}_2\text{O}_2$  deposit. The solution mechanism enhances large  $\text{Li}_2\text{O}_2$  toroid growth (higher discharge capacity), while surface mechanism results in thin passivating film of  $\text{Li}_2\text{O}_2$  (lower discharge capacity) (73, 150). Therefore for the purpose of prolonged battery cycle life, solution mechanism is more favorable and the variables promoting solution-way mechanism should be prioritized.

## 4.6. Conclusions.

In this chapter we have presented the mechanistic studies of oxygen reduction reaction in several non-aqueous solvents, namely acetonitrile, dimethylsulfoxide and  $\text{PYR}_{14}\text{TFSI}$  ionic liquid in the presence of tetraalkylammonium cations and  $\text{Li}^+$ , by means of Rotating Ring Disc Electrode technique, coupled to EQCM and DEMS. We have shown that RRDE is a powerful technique to get an insight into the ORR mechanism due to the possibility to detect soluble superoxide intermediate.

The formation of reversible and stable  $\text{O}_2/\text{O}_2^-$  couple was observed in all non-aqueous solvents studied in the presence of tetraalkylammonium cations, in agreement with previous studies.

As expected, the addition of  $\text{Li}^+$  cation was found to change significantly the ORR mechanism. We have reported that small additions of  $\text{Li}^+$  into ACN operate in different direction the ORR kinetics by affecting the stability of  $\text{O}_2^-$  with respect to  $\text{O}_2$  and insoluble  $\text{Li}_2\text{O}_2$ . Unlike the behavior in acetonitrile-lithium solutions,  $\text{LiO}_2$  is more stable in DMSO and can diffuse out in solution and be detected at the ring electrode. In case of the ionic liquid  $\text{PYR}_{14}\text{TFSI}$ , the competition of ORR product  $\text{O}_2^-$  for the  $\text{PYR}_{14}^+$  and the strong Lewis acid  $\text{Li}^+$  is reflected in the lower yield of soluble superoxide, EQCM mass increase and the positive shift of the  $\text{O}_2/\text{O}_2^-$  potential while increasing the  $\text{Li}^+$  concentration in the ionic liquid.

No soluble superoxide could be detected into the ACN solution for  $\text{Li}^+$  concentrations above 10  $\mu\text{M}$ , while the DMSO-based solutions could stabilize the soluble superoxide even at considerable  $\text{Li}^+$  concentrations as 0.1 M, and for the ionic liquid  $\text{PYR}_{14}\text{TFSI}$  the soluble superoxide could be detected up to the  $\text{Li}^+$  concentrations of 25 mM (roughly double concentration of dissolved oxygen).

We have shown that the solvents with higher ability to solvate the  $\text{Li}^+$  cation ( $\text{DMSO} > \text{PYR}_{14}\text{TFSI} > \text{ACN}$ ), result in stabilization of soluble superoxide and thus promote the solution mechanism resulting in the higher discharge capacity of cell.

Finally, we have analyzed the progress in understanding the fundamental mechanism of the ORR in non-aqueous solvents, transitioning from the HSAB theory into the new model based on the solubility and stability of  $\text{LiO}_2$  intermediate. This new model elaborated independently in

2014-2015 by several research groups explains two limiting cases: solution versus surface mechanism that reflects the  $\text{Li}_2\text{O}_2$  deposit shape and the battery discharge capacity.

#### 4.7. Resumen en castellano del capítulo 4. Reacción de cátodo: detalles del mecanismo de electroreducción y evolución de oxígeno.

En este capítulo se estudió en detalles el mecanismo de electroreducción de oxígeno en distintos solventes no acuosos, tales como acetonitrilo, dimetil sulfóxido y el líquido iónico  $\text{PYR}_{14}\text{TFSI}$  en presencia de los iones tetraalquilamonio y litio, mediante el uso de la técnica electroquímica del electrodo rotatorio de disco y anillo (RRDE), complementado estos resultados con los obtenidos mediante las técnicas de la microbalanza electroquímica de cristal de cuarzo (EQCM) y la espectrometría de masas diferencial electroquímica (DEMS). Hemos demostrado que el RRDE es una técnica poderosa para estudiar dichos mecanismos ya que permite detectar la presencia del superóxido soluble.

La formación de la cupla reversible y estable de  $\text{O}_2/\text{O}_2^-$  fue observada en todos los solventes no acuosos empleados en presencia del ion tetraalquilamonio, que está en concordancia con estudios anteriores.

Sin embargo, el agregado del catión  $\text{Li}^+$  altera significante el mecanismo de reducción de oxígeno (ORR). Hemos demostrado que el agregado de pequeñas cantidades de ion  $\text{Li}^+$  en ACN opera en dirección opuesta a la cinética de la ORR afectando la estabilidad del anión superóxido  $\text{O}_2^-$  con respecto al oxígeno  $\text{O}_2$  y el peróxido de litio insoluble  $\text{Li}_2\text{O}_2$ . Al contrario de los soluciones de litio en acetonitrilo, el superoxido de litio es más estable en DMSO y puede difundir a la solución y ser detectado en el anillo del RRDE. En el caso del líquido iónico  $\text{PYR}_{14}\text{TFSI}$ , la competencia del producto de ORR  $\text{O}_2^-$  por los cationes  $\text{PYR}_{14}^+$  y el ácido fuerte de Lewis  $\text{Li}^+$ , está reflejado en una baja producción de superóxido soluble, en el aumento de masa observado en EQCM y en el cambio a valores más positivos del potencial de  $\text{O}_2/\text{O}_2^-$ , con el aumento de la concentración del litio en el líquido iónico.

No se detectó superóxido soluble en soluciones de acetonitrilo cuyas concentraciones de litio fueran mayores a  $10 \mu\text{M}$ , mientras que en electrolitos basados en DMSO, el superóxido soluble fue estable aún en concentraciones elevadas del litio como por ejemplo  $0.1 \text{ M}$ . Por otro lado, en el líquido iónico  $\text{PYR}_{14}\text{TFSI}$ , el superóxido soluble fue detectado hasta una concentración de  $\text{Li}^+$  de  $25 \text{ mM}$  (que corresponde al doble de la solubilidad de oxígeno en este electrolito).

Hemos demostrado que los solventes con mayor capacidad de solvatar al ion  $\text{Li}^+$  ((DMSO >  $\text{PYR}_{14}\text{TFSI}$  > ACN), estabilizan en mayor grado al ion superóxido y promueven el mecanismo vía solución que resulta en mayor capacidad de descarga de la celda.

Finalmente hemos progresado en el análisis y comprensión del mecanismo fundamental de la ORR en solventes no acuosos, que evolucionó desde la teoría de HSAB (Teoría del ácido-base fuerte y débil, en inglés) al nuevo modelo basado en la solubilidad y la estabilidad del intermediario  $\text{LiO}_2$ . Este modelo fue elaborado de forma independiente entre 2014 y 2015 por varios grupos de investigación y explica los dos casos extremos: el mecanismo vía solución versus el mecanismo vía superficie, que resulta en una morfología diferente del depósito de  $\text{Li}_2\text{O}_2$  y en una capacidad de descarga de la batería totalmente diferentes.

El mecanismo de reacción (solución versus superficie) se ve influenciado por numerosos factores:

- 1) Naturaleza del solvente: número donador DN y aceptor del solvente AN. El solvente con mayor número donador solvata mejor al ion  $\text{Li}^+$  y estabiliza el superóxido soluble.
- 2) Naturaleza del anión de sal de litio. (146-148). Del mismo modo como el solvente, la capacidad del anión a estabilizar el cation  $\text{Li}^+$  promueve el mecanismo vía solución.
- 3) Aditivos e impurezas. (72, 73, 84, 149). Algunos aditivos o impurezas con un alto número donador (por ejemplo trazas del agua(73)) en soluciones de número donador más bajo pueden solvatar de manera preferencial el ion litio y promover el mecanismo vía solución. En el próximo capítulo se estudiara en más detalles el efecto de la solvatación preferencial del ion litio.
- 4) Densidad de corriente y el potencial.(150, 151). La densidad de corriente y el sobrepotencial de descarga más altos promueven una reducción más rápida mediante una electroreducción por dos electrones para formar el peróxido de litio a expensas del mecanismo de dismutación y por eso promueve el mecanismo de superficie.
- 5) Concentración de iones litio. En este capítulo se demostró cómo afectan las concentración de litio más bajas, resultando en la estabilización del ion superóxido, promoviendo la reacción vía solución.

# Chapter 5. The exploration of mixed electrolyte systems for the Li-air battery and the effect of Li<sup>+</sup> solvation.

## 5.1. Introduction.

As shown in the previous chapter, DMSO exhibits unusual properties related to the ORR that is stabilization of the intermediate O<sub>2</sub><sup>-</sup> anion, which does not occur in other solvents (53). In this chapter we report that soluble superoxide radical anions can be detected at a rotating ring disk electrode (RRDE) system in lithium solutions of acetonitrile (ACN) containing 0.1 M DMSO ( $\chi_{\text{ACN}} = 0.995$ ), while no evidences of soluble O<sub>2</sub><sup>-</sup> are observed in lithium acetonitrile solutions.

We have suggested that those observations could be due to the preferential solvation of Li<sup>+</sup> cation by DMSO molecules that in turn prevents the disproportionation of lithium superoxide ( $2 \text{O}_2\text{Li} \rightarrow \text{Li}_2\text{O}_2 + \text{O}_2$ ). In order to test this hypothesis, we have studied the ionic conductivity of lithium hexafluorophosphate (LiPF<sub>6</sub>) in comparison to tetrabutylammonium hexafluorophosphate (TBAPF<sub>6</sub>) in ACN–DMSO mixtures in the whole composition range. These results were complemented with measurements of Li/Li<sup>+</sup> electrode potential as a function of the composition of the ACN-DMSO mixture.

On the other hand we have studied the oxygen diffusivity and solubility in these mixed solvent systems that also show a non linear dependence as a function of mixture composition. Both the effects of preferential solvation on Li<sup>+</sup> ion and O<sub>2</sub> molecule are discussed in this chapter.

## 5.2. The RRDE evidence of $\text{Li}^+$ preferential solvation.

Unlike in acetonitrile, in the strong Lewis base DMSO with 0.1 M  $\text{LiPF}_6$  electrolyte it has very recently been shown that soluble superoxide formed at a glassy carbon disk can be detected at a gold ring (53) due to the strong  $\text{Li}^+$  solvation in the highly polar DMSO and the stabilization of the solvated  $\text{O}_2^-\text{Li}^+$  ion pair in solution. We have studied the ORR in 0.1 M  $\text{LiClO}_4$  containing 0.1 M DMSO in an equivalent concentration to the lithium ion in a large excess of acetonitrile (1:200). Figure 5.1 depicts the resulting RRDE ORR curve with hysteresis, surface passivation and oxidation of  $\text{Li}_2\text{O}_2$  at positive potentials and detection of superoxide oxidation ring current. Notice that the soluble  $\text{O}_2^-$  reaching the ring is an important fraction of the flux at the disk electrode, i.e.  $-\text{I}_\text{R}\text{N}_0^{-1}$  compared to  $\text{I}_\text{D}$ .

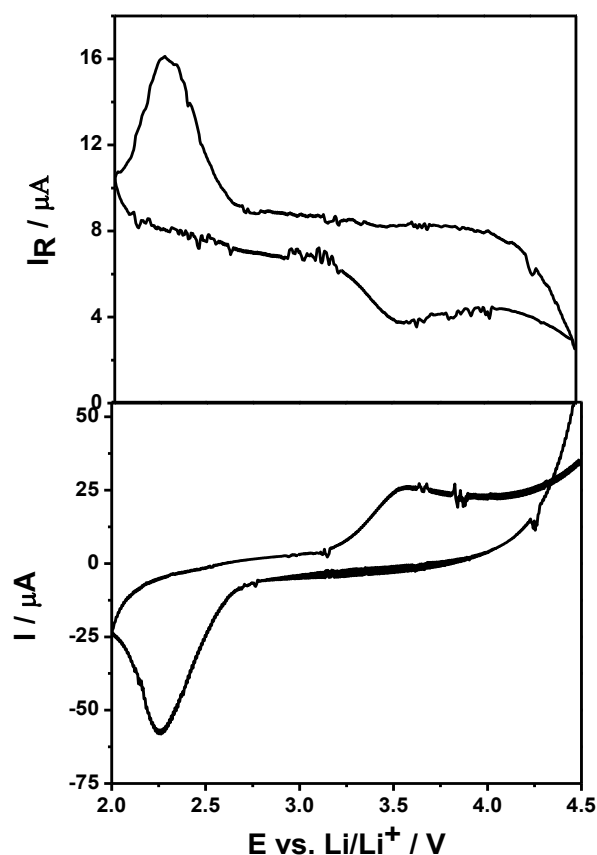


**Figure 5.1.**  $\text{O}_2$  reduction on a GC/Pt RRDE in  $\text{O}_2$  saturated 0.1 M  $\text{LiClO}_4$  in purified  $\text{CH}_3\text{CN}$  containing 0.1 M DMSO at  $W = 9$  Hz and scan rate  $0.1 \text{ Vs}^{-1}$ . Ring current at  $\text{ER}=0\text{V}$ .  $\text{A}_\text{D} = 0.2 \text{ cm}^2$ .

Even in large excess of acetonitrile,  $\text{Li}^+$  ions seem to be preferentially solvated by DMSO with solvated  $\text{Li}^+\text{-O}_2^-$  ion pair stable with respect to disproportionation into  $\text{Li}_2\text{O}_2$  and  $\text{O}_2$ . The decrease in  $\text{O}_2^-$  concentration at more reducing potentials, i.e. a maximum ring current, indicates that a second electron transfer occurs and soluble  $\text{Li}^+ - \text{O}_2^-$  produces  $\text{Li}_2\text{O}_2$  collecting less superoxide at the ring. We have also investigated the slow reaction of DMSO and  $\text{O}_2^-$  into dimethylsulfone and spectroscopic studies are presented in the next chapter..

### 5.3. Redox potential of the Li/Li<sup>+</sup> electrode in different media.

The importance to assess correctly the standard potentials in non-aqueous solvents was mentioned already in the chapter 2 and in the perspective paper(152). Here we will study in detail the redox potential of Li/Li<sup>+</sup> couple in different media, as well as in mixed electrolyte systems and draw corresponding conclusions about Li<sup>+</sup> preferential solvation and its implications on the ORR and Li-air battery performance.

Probably one of the best known Li/Li<sup>+</sup> potentials is one in the aqueous solution and is equal to about -3.04 V vs. NHE, as can be found in any table of standard electrode potentials. As we know that lithium metal is reactive with water, this potential has been measured by using diluted lithium amalgam which is stable in water. For the different systems, the lithium potential will depend on the solvent-electrolyte combination with the Li<sup>+</sup>-ion solvation energy being a very important factor. Without going deeply into the thermodynamics, we can assume that for the reaction



taking place in two different solvents, the difference between the electrode potentials is proportional to the difference between the Gibbs energies of solvation in those two solvents :  $\Delta G = -nF\Delta E$ . It is well known that for the small ion such as Li<sup>+</sup> the solvation energy may vary strongly from solvent to solvent. The mentioned above relation is of course also true for the different cations: Na<sup>+</sup>, K<sup>+</sup> and Mg<sup>2+</sup>, however with a smaller  $\Delta E$  difference for a bigger size of cation (lower difference in solvation energies). That is why in 1947 Pleskov have suggested Rb/Rb<sup>+</sup> electrode as a reference for non-aqueous solvents however it was found later by Koeppe et al. in 1960 that even for such big cation as Rb<sup>+</sup> the difference in solvation energies could not be neglected (cited from IUPAC document: RECOMMENDATIONS ON REPORTING ELECTRODE POTENTIALS IN NONAQUEOUS SOLVENTS(153)).

In 1983 the issue of reporting electrode potentials in non-aqueous solvents already existed and the IUPAC recommended the use of ferrocene/ferrocenium ion and bis(biphenyl)chromium(I)/bis(biphenyl)chromium(O)redox couples as stable internal references(153). Those two redox couples presented the best known solvent independent redox

systems due to their big ionic size and delocalized charge, meaning that solvating energies would vary very slightly in different solvents.

We have measured the cyclic voltammetry of the ferrocene/ferrocenium redox couple versus Li metal submerged in the  $\text{Li}^+$ -containing solution in different organic solvents. The results are presented on the figure 5.2. As can be seen from the figure, the reversible ferrocene/ferrocenium couple is observed with potentials varying in different solvents reaching up to 0.5 V difference from ACN to DMSO. Assuming the potential of ferrocene couple is not affected by the solvent, it is concluded that this variation is due to the shift in our “reference”  $\text{Li}/\text{Li}^+$  electrode potential.

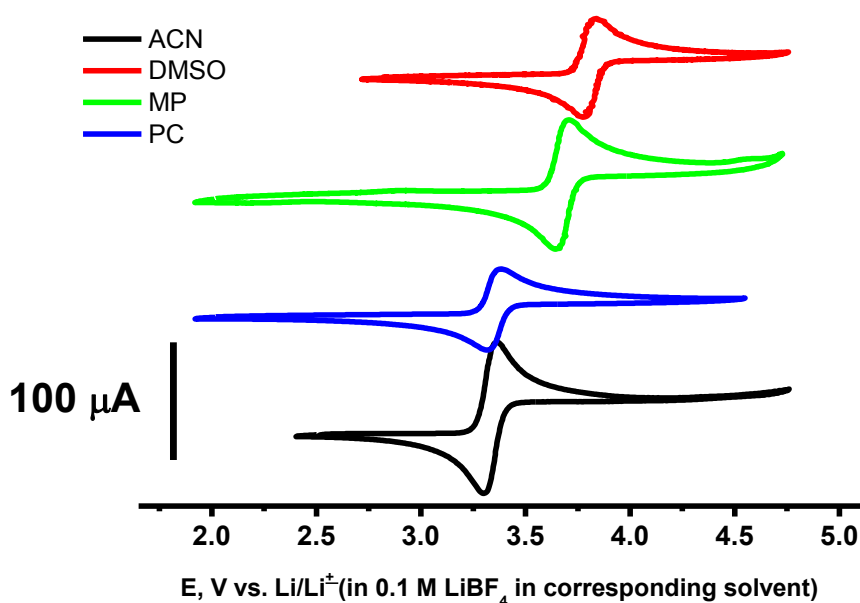
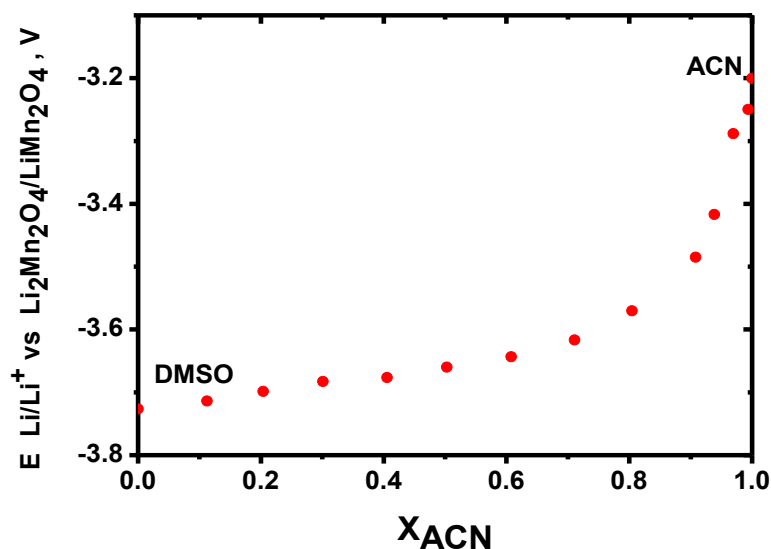


**Figure 5.2.** IR drop corrected cyclic voltammeteries performed in the solution containing 10 mM ferrocene and 0.1 M  $\text{LiBF}_4$  in ACN (acetonitrile), DMSO (dimethyl sulfoxide), MP (1-Methyl-2-pyrrolidinone) and PC (propylene carbonate). Working electrode: Pt, counter electrode: PT mesh, reference electrode: Li, scan rate 100 mV/s.

In case of dealing with the mixed electrolyte, the estimation of the  $\text{Li}/\text{Li}^+$  potential also is not trivial. It has been shown both experimentally<sup>(84)</sup> and theoretically<sup>(154)</sup>, that when working with DMSO-ACN mixtures, in the solutions rich in ACN (for example 80% of ACN and 20% of DMSO mole fractions), the  $\text{Li}/\text{Li}^+$  potential is more similar to that of pure DMSO, than pure

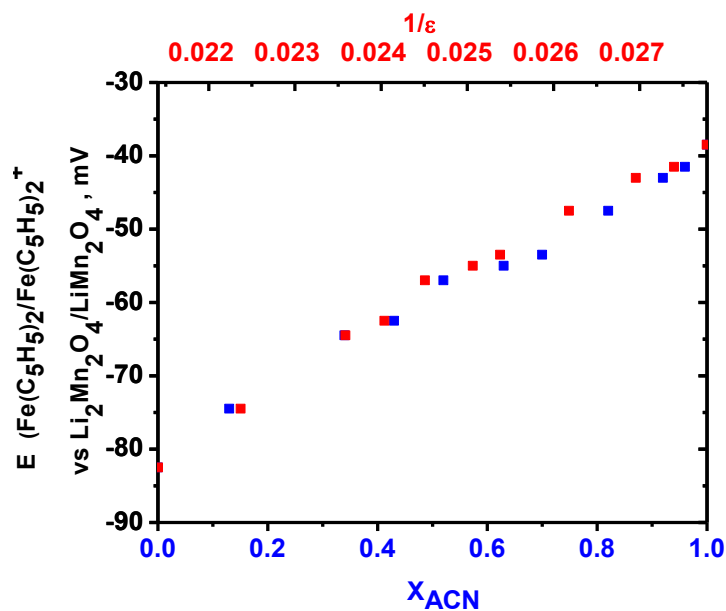
ACN (see figure 5.3). This is explained by the preferential solvation of  $\text{Li}^+$  cations by DMSO molecules even in the huge excess of ACN.

Figure 5.3 shows the  $\text{Li}/\text{Li}^+$  electrode potential vs. the reversible lithium electrode in ACN–DMSO mixtures in the whole composition range.



**Figure 5.3.  $\text{Li}/\text{Li}^+$  electrode potential vs.  $\text{Li}^+$  reversible electrode as a function of ACN mole fraction in ACN–DMSO mixtures.**

Corrections, due to the potential difference in the interface between the DMSO reference electrode and the DMSO-ACN solution, determined by measuring the  $\text{Li}_2\text{Mn}_2\text{O}_4/\text{LiMn}_2\text{O}_4$  reference electrode vs. the ferrocene-ferrocenium couple, plotted in figure 5.4, were taken into account in the calculations. The figure also shows the scale of the inverse of the dielectric constant of the mixtures.



**Figure 5.4. Redox potential of the ferrocene-ferrocenium couple versus  $\text{Li}_2\text{Mn}_2\text{O}_4/\text{LiMn}_2\text{O}_4$  reversible reference electrode, determined in solutions of 0.1 M  $\text{LiPF}_6$ , 5-10 mM ferrocene, as a function of  $\chi_{ACN}$  bottom scale (blue), and as a function of inverse dielectric constant top scale (red).**

As it has been previously pointed out the potential of the  $\text{Li}/\text{Li}^+$  couple (vs.  $\text{Li}_2\text{Mn}_2\text{O}_4/\text{LiMn}_2\text{O}_4$  reference electrode) depends strongly on the electrolyte used to measure it. This is due to the fact that lithium solvation free energy depends notably on the solvent, for instance, the potential of a non-aqueous  $\text{Ag}/\text{Ag}^+$  reference electrode vs.  $\text{Li}/\text{Li}^+$  (0.1 M  $\text{LiPF}_6$ ) varies from 3.23 V in ACN to 3.70 V in DMSO. In figure 5.3, it can be observed that around mole fraction  $\chi_{ACN} \sim 0.8$  the potential of the  $\text{Li}/\text{Li}^+$  electrode increases markedly, while around  $\chi_{ACN} \sim 0.95$  the curvature of the potential composition dependence seems to vary. This seems to indicate that an important solvation effect is observed in ACN–DMSO mixtures even with small DMSO contents.

Computer simulation results (155) reinforce this hypothesis showing that lithium ion first solvation shell is formed exclusively by DMSO molecules for  $\chi_{ACN} < 0.9$ , while incorporates ACN molecules above this composition, as shown in the figure 5.5.

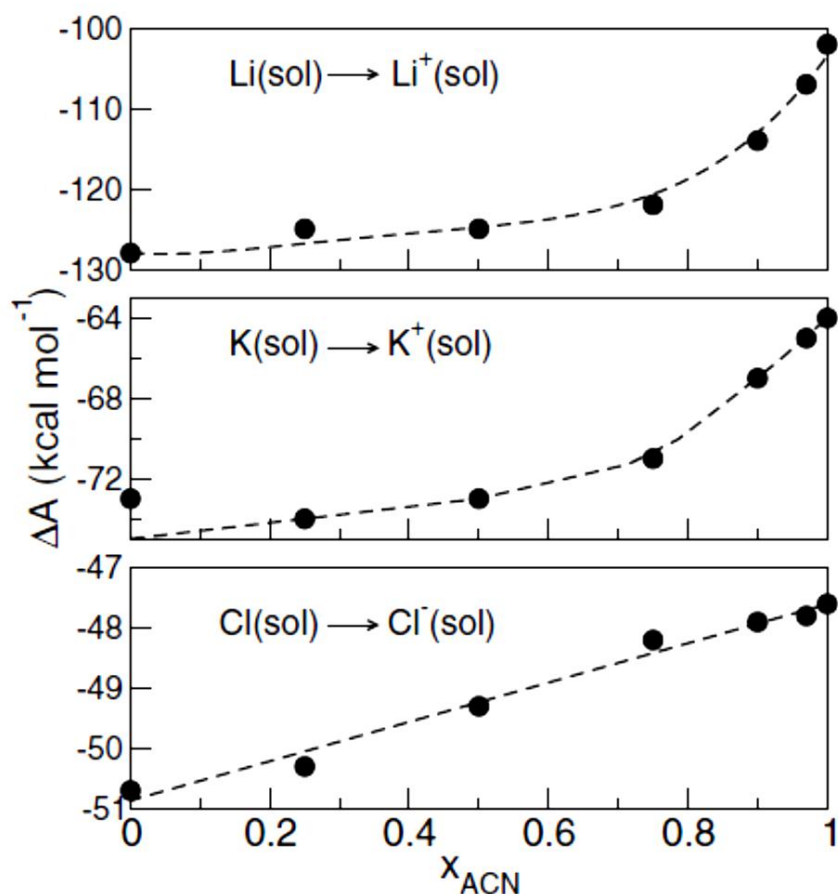


**Figure 5.5.** Free energy associated to the “charging process”  $M(sol) \rightarrow M^+(sol)$  and  $X(sol) \rightarrow X^-(sol)$ . Reproduced from the reference (155): R. Semino, G. Zaldívar, E.J. Calvo, D. Laria, Lithium solvation in dimethyl sulfoxide–acetonitrile mixtures, *J. Chem. Phys* **141** (2014) 214509.

Computer simulation results indicate that notable changes in lithium solvation are produced for very small quantities of DMSO in ACN–DMSO mixtures in accordance with our measurements. Thus, although the two solvents exhibit “similar” physicochemical properties, such as their dipolar moment and aprotic character, changes in lithium solvation are produced for very small DMSO contents in the mixtures.

In order to further test this hypothesis, we also studied the conductivity of  $LiPF_6$  and  $TBAPF_6$  in the whole composition range to compare the molar conductivity of the solvated  $Li^+$  ion with that of the bulky non solvated  $TBA^+$  cation (reported in this chapter 5.4.)

A very similar phenomena has been observed for the  $\text{Li}/\text{Li}^+$  redox potential measured in the mixtures of DMSO with ionic liquid  $\text{PYR}_{14}\text{TFSI}$ , that is shown on the figure 5.6. The  $\text{Li}^+$  solvation is weaker in the ionic liquid  $\text{PYR}_{14}\text{TFSI}$  with respect to the DMSO, that solvates strongly the  $\text{Li}^+$  ion. That is reflected in the big difference of redox potential of  $\text{Li}/\text{Li}^+$  in pure DMSO and ionic liquid  $\text{PYR}_{14}\text{TFSI}$  and is in agreement with the RRDE results shown in chapter 4.4. The pronounce decrease of  $\text{Li}/\text{Li}^+$  redox potential is observed in the range 0.8-1 mole fraction of  $\text{PYR}_{14}\text{TFSI}$ , that can be explained by the preferential solvation of  $\text{Li}^+$  by DMSO in the excess of ionic liquid molecules, that is the same behavior as in the DMSO-ACN mixtures.

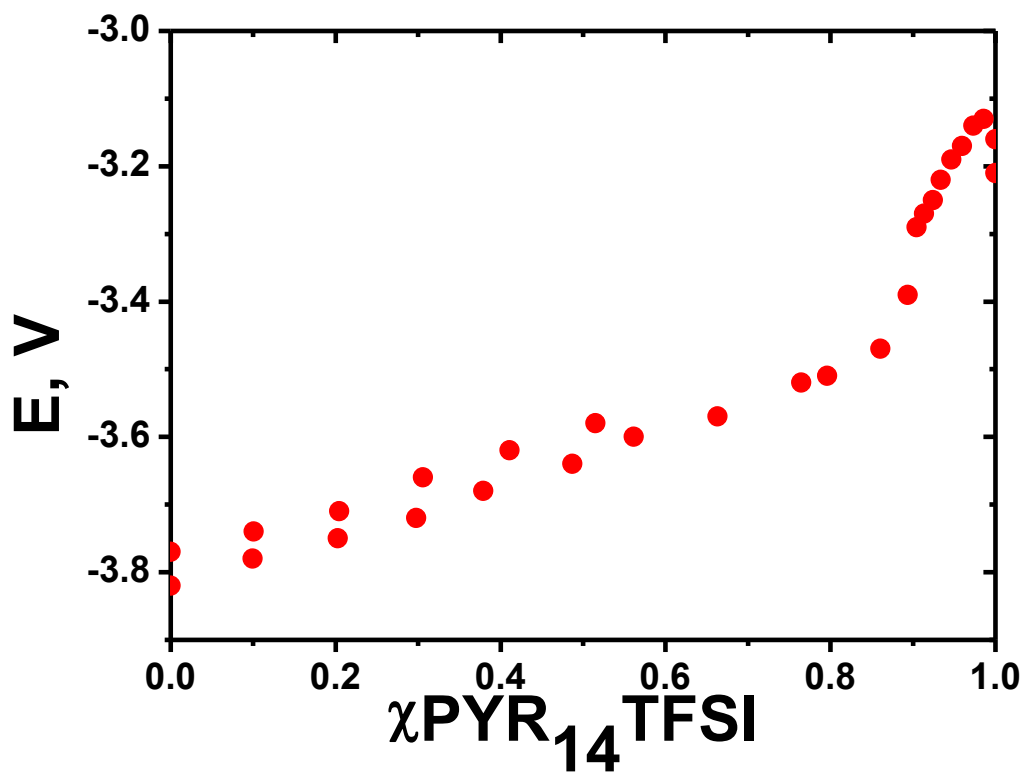
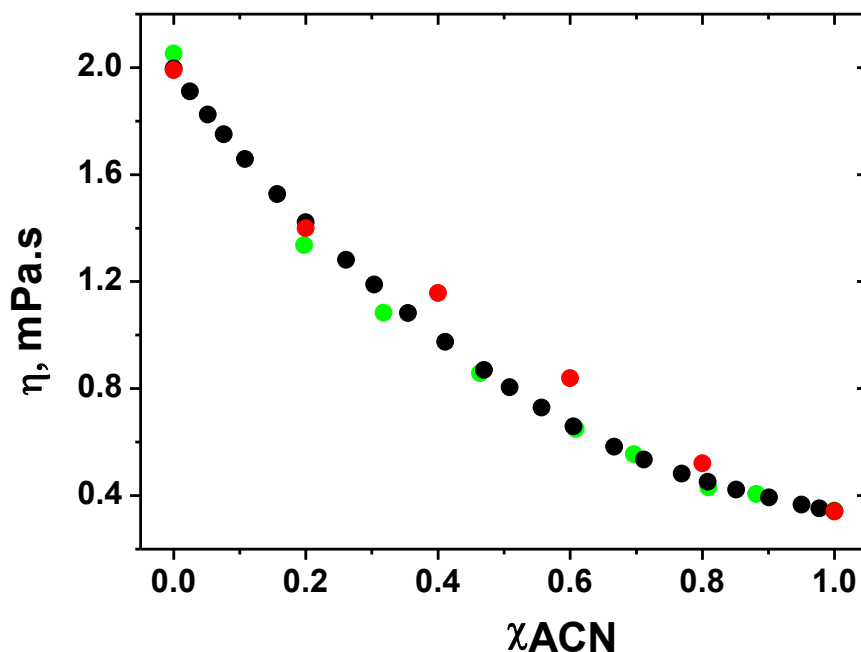


Figure 5.6.  $\text{Li}/\text{Li}^+$  electrode potential vs.  $\text{Li}^+$  reversible electrode as a function of  $\text{PYR}_{14}\text{TFSI}$  mole fraction in  $\text{PYR}_{14}\text{TFSI}$ -DMSO mixtures.

#### **5.4. A conductivity study of preferential solvation of lithium ion in acetonitrile-dimethyl sulfoxide mixtures**

Among the research concerning the potentially interesting electrolytes for lithium batteries, transport studies are of great interest and importance. Numerous studies of transport properties of several electrolyte systems for Li-ion batteries are nowadays available (156-158). However, it has been shown that typical electrolyte systems employed in Li-ion batteries (based on organic carbonates and ethers) are not appropriate for Li-air batteries due to the electrolyte decomposition by the oxygen reduction reaction (ORR) intermediates and/or products (34, 47, 49, 159-164). Thus, more information on transport properties in other electrolyte systems for Li-air batteries is needed.

**Viscosity of ACN–DMSO mixtures.** Figure 5.7 shows our viscosity measurements in comparison with reported data by other authors (100, 101). It can be observed that our measurements agree, within the experimental error (between 2.3 and 3.6%), with viscosity data reported by Grande et al. (100) Thus, in order to fit the experimental viscosity data as a function of composition, we chose as input values our experimental data and those reported by these authors.



**Figure 5.7. Viscosity of ACN–DMSO mixtures as a function of ACN mole fraction. Data reported by Gill et al. (101)] (red), Grande et al. (100) (black), and that measured in this work (green).**

**Conductivity of LiPF<sub>6</sub> and TBAPF<sub>6</sub> in ACN–DMSO mixtures.** Table 5.1 and figure 5.9 show the molar conductivities of LiPF<sub>6</sub> and TBAPF<sub>6</sub>, at infinite dilution, as a function of composition. Thermophysical properties (density, dielectric constant, and viscosity) of the corresponding mixtures, calculated as previously described, are included in Table 5.1.

The errors assigned to the values of  $\Lambda^\circ$  in Table 5.1, obtained from the standard deviation of the fits of  $\Lambda(c)$  vs.  $c$  with the following equation:

$$\Lambda = \Lambda^0 - S(\alpha c)^{\frac{1}{2}} + E\alpha c \cdot \ln(\alpha c) + J_1(d)\alpha c - J_2(d)(\alpha c)^{\frac{3}{2}} - K_a \Lambda \gamma_{\pm}^2(\alpha c) \quad (5.2)$$

vary between 0.09% and 1.2% for our calculations. Figure 5.8 shows, as mode of example, the deviations of the experimental data to the calculated best fit for the conductivity measurements of LiPF<sub>6</sub> in the pure solvents.

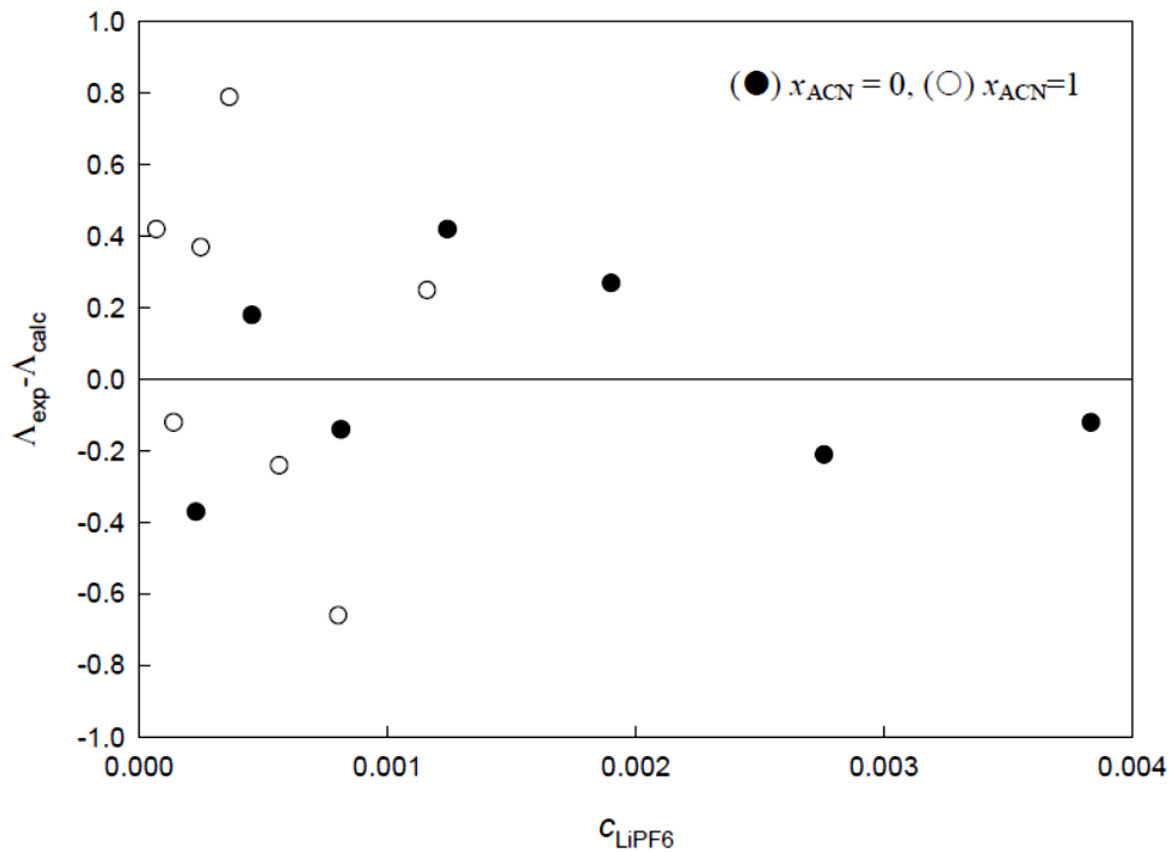


**Figure 5.8. The deviations of the experimental data to the calculated best fit for the conductivity measurements.**

In order to estimate the uncertainty in the molar conductivity of the salt, at each concentration and solvent composition, we should analyze the uncertainties in the salt molarity, temperature, and solvent conductivity (background conductivity).

**Table 5.1. Molar conductivity of LiPF<sub>6</sub> and TBAPF<sub>6</sub> in ACN–DMSO mixtures and thermo-physical properties of the corresponding mixtures.**

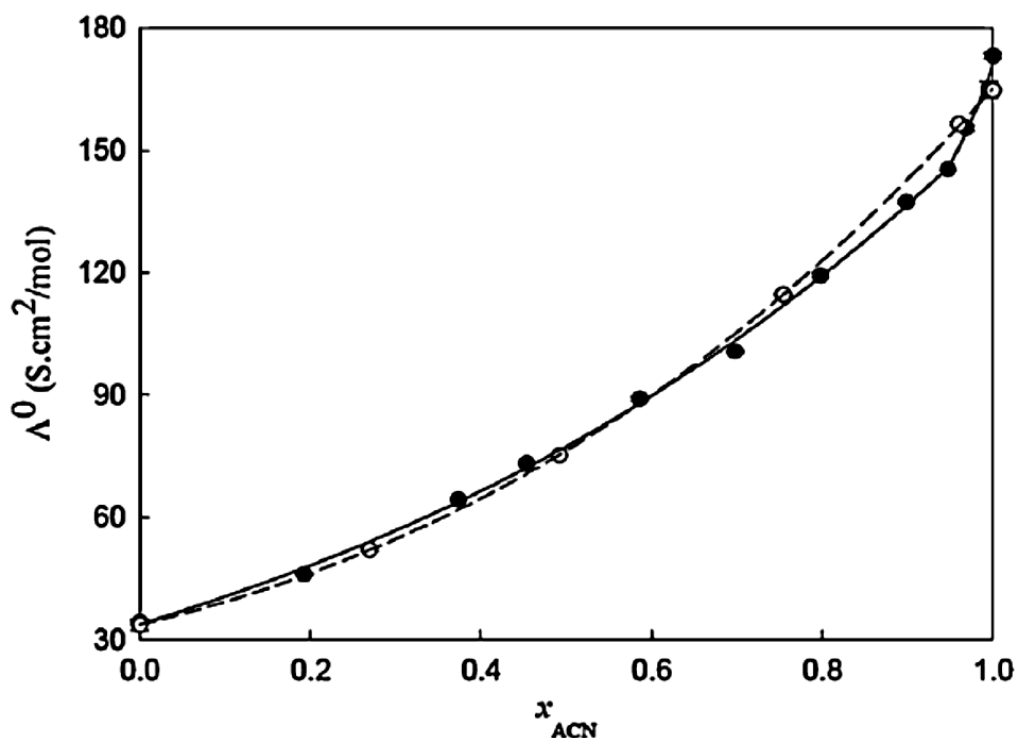
$x_{\text{ACN}}$	$\delta$ (g/cm <sup>3</sup> )	$\epsilon$	$\eta$ (mPa s)	$\Lambda^\circ$ LiPF <sub>6</sub> (S cm <sup>2</sup> mol <sup>-1</sup> )
0.000	1.096	46.7	1.990	34.1 ± 0.3
0.192	1.043	43.9	1.437	46.0 ± 0.1
0.373	0.9901	42.1	1.023	64.3 ± 0.3
0.453	0.9657	41.4	0.8760	70.23 ± 0.06
0.586	0.9238	40.3	0.6788	89.1 ± 0.5
0.697	0.8868	39.4	0.5517	100.7 ± 0.3
0.798	0.8521	38.5	0.4626	109.3 ± 0.6
0.898	0.8158	37.3	0.3934	137.4 ± 0.4
0.947	0.7977	36.7	0.3659	145.4 ± 0.3
0.968	0.7896	36.4	0.3550	155.5 ± 0.5
0.995	0.7796	36.1	0.3426	165 ± 2
1.000	0.7775	36.0	0.3401	173.2 ± 0.7

$x_{\text{ACN}}$	$\delta$ (g/cm <sup>3</sup> )	$\epsilon$	$\eta$ (mPa s)	$\Lambda^\circ$ TBAPF <sub>6</sub> (S cm <sup>2</sup> mol <sup>-1</sup> )
0.000	1.096	46.7	1.990	33.6 ± 1.4*
0.269	1.021	43.1	1.2476	52.0 ± 0.6
0.492	0.9538	41.1	0.8131	75.2 ± 0.3
0.754	0.8674	38.9	0.4992	114.6 ± 0.2
0.960	0.7929	36.6	0.3594	156.5 ± 0.5
1.000	0.7775	36.0	0.3401	164.8 ± 0.1*

\* data obtained from  $\lambda_i$  values reported in Ref.(92, 165, 166)

The salt molar concentration was determined by weight, using the calculated density of the mixtures with an uncertainty of ±1%. The temperature of the sample was determined with an uncertainty of ±0.08°C, and considering that the molar conductivity of the salts changes approximately 2%/K, the uncertainty in the temperature introduces an uncertainty of 0.16% in the measured conductivity. Finally, it was estimated that the change of water sorbed by the solvent mixture during the measurements (~10 ppm) has a negligible effect on the measured conductivity, because the solvent conductivity (before adding the salt) does not change significantly.



**Figure 5.9. Infinite dilution molar conductivity values for LiPF<sub>6</sub> (●) and TBAPF<sub>6</sub> (○) in ACN–DMSO mixtures as a function of ACN mole fraction.  $\Lambda^\circ$  for TBAPF<sub>6</sub> in the pure solvents were taken from Ref (92, 165, 166). Error bars for the conductivities plotted in this figure are smaller than the size of the symbols. The dashed line corresponds to the polynomial fit performed for TBAPF<sub>6</sub> as a function of composition, while the solid lines, merging at  $\chi_{ACN} \sim 0.95$ , are the best fits for LiPF<sub>6</sub>.**

Therefore, it can be concluded that the relative error of the molar conductivity should not exceed 1.2%. The cell constant was determined with an error of 1.1%, but this does not affect the precision, but the accuracy of the conductivity measurements.

Reported data (92-96, 165, 166) for the ionic infinite molar conductivities of Li<sup>+</sup> and PF<sub>6</sub><sup>-</sup> ions in ACN (92, 93, 165), and DMSO (92, 94-96, 166), indicate that for LiPF<sub>6</sub>,  $\Lambda^\circ = 173.1 \pm 0.3 \text{ S cm}^2 \text{ mol}^{-1}$  in pure ACN, and  $\Lambda^\circ = 33 \pm 2 \text{ S cm}^2 \text{ mol}^{-1}$  in pure DMSO, being our measurements in excellent agreement with these results.

As expected, the infinite dilution molar conductivities of both salts increase with increasing ACN content, since the viscosity decreases with increasing ACN content in the mixture. However, while  $\Lambda^0$  for TBAPF<sub>6</sub> in ACN–DMSO mixtures exhibits a monotonic concentration dependence, which could be properly fitted with a cubic equation all over the composition range,  $\Lambda^0$  for LiPF<sub>6</sub> exhibits non-monotonic composition dependence with a clear change in the curvature around  $\chi_{ACN} \sim 0.95$ .

The association constants of LiPF<sub>6</sub> are only significant in pure ACN ( $Ka = 43 \pm 7$ ) and for the mixture with  $\chi_{ACN} = 0.995$  ( $Ka = 28 \pm 16$ ). This result can be explained considering that the dielectric constant of the mixtures increases with increasing DMSO content (see Table 5.1). The infinite dilution molar conductivities of TBAPF<sub>6</sub> in the pure solvents were extracted from ionic molar conductivity data (92, 165, 166) of the component ions. The ionic association for TBAPF<sub>6</sub> in ACN–DMSO solutions mixtures for  $\chi_{ACN} = 0.27, 0.49, 0.75$  and  $0.96$  are negligible and the salt is fully dissociated in this concentration range.

The viscosity of the ACN–DMSO mixtures changes from 0.34 mPa s in pure ACN to 1.99 mPa s in pure DMSO. Thus, the viscous friction is primarily responsible for the strong ionic mobility changes with composition. In order to eliminate the effect of viscosity in the conductivity composition dependence we plotted, in figure 5.10, for LiPF<sub>6</sub> and TBAPF<sub>6</sub>, the Walden product, expressed by,

$$\lambda^0 \eta = \frac{z^2 e F}{Ar} \quad (5.3)$$

where  $z$  is the ionic charge,  $e$  is the electron charge,  $F$  is the Faraday constant,  $r$  is the hydrodynamic radius of the ion, and  $A$  is a constant whose value depends on the friction conditions ( $6\pi$  for stick and  $4\pi$  for slip boundary conditions, respectively) for Li<sup>+</sup> and TBA<sup>+</sup> ions, with  $\lambda_i$  calculated as mentioned previously.

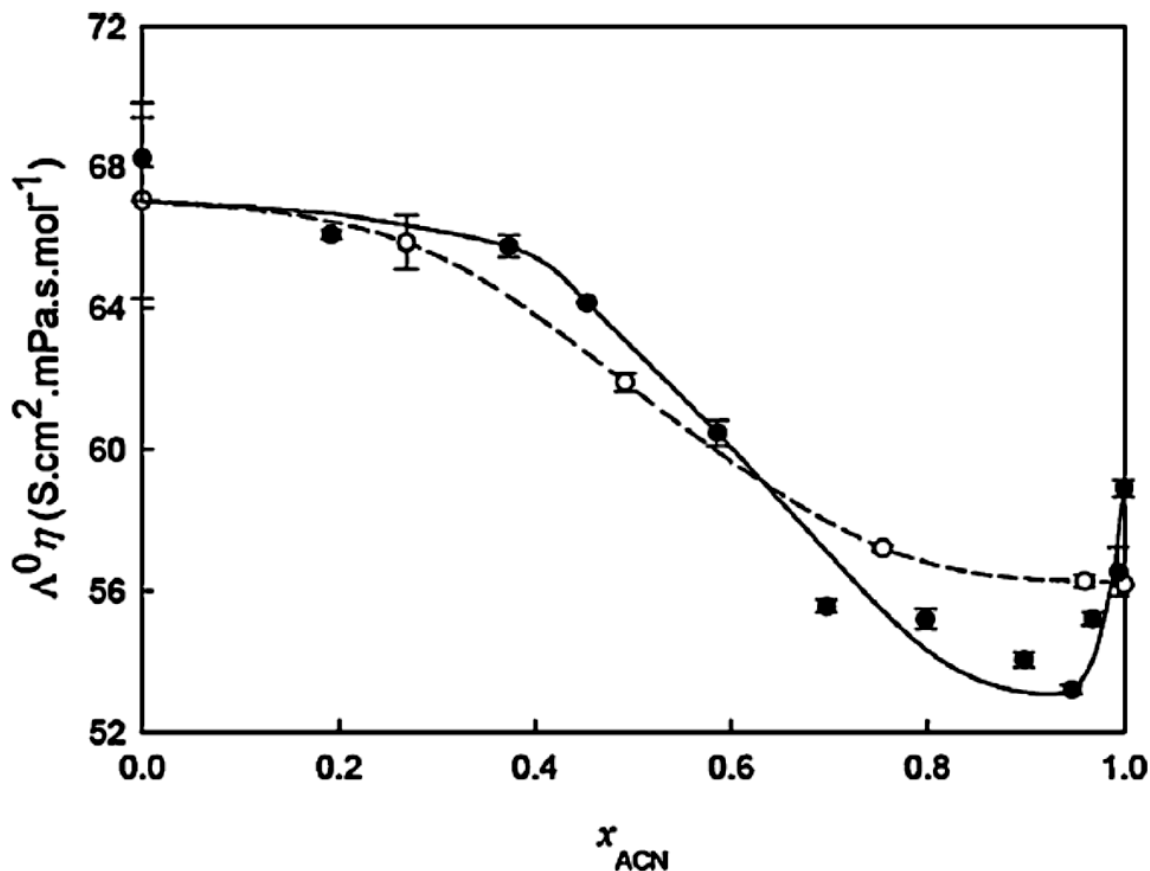


**Fig. 5.10. Walden product for the limiting molar conductivities of  $\text{LiPF}_6$  (●) and  $\text{TBAPF}_6$  (○) in ACN–DMSO mixtures as a function of ACN mole fraction. The dotted and bold lines for  $\text{TBAPF}_6$  and  $\text{LiPF}_6$ , respectively, were added as a guide to the eye.**

In the figure 5.10 it can be observed that the Walden product for  $\text{TBAPF}_6$  is not constant as predicted by the Walden rule, but decreases from  $67 \text{ S cm}^2 \text{ mPa s mol}^{-1}$  in DMSO down to  $56 \text{ S cm}^2 \text{ mPa s mol}^{-1}$  in ACN. This implies an apparent change in the radius of the salt. However, this is not plausible taking into account that the ions are bulky and should behave essentially as non-solvated ions. Therefore, the composition dependence of the Walden product needs to be analyzed in terms of a more complete model that includes the dielectric friction of the ions with the solvent dipoles (167-169). Briefly, the coupling of the ion mobility with the dipole solvent relaxation time leads to an expression for the local viscosity near the ion given by (169),

$$\eta(r) = \eta_0 \left( 1 + \frac{R_{HO}^4}{r^4} \right) \quad (5.4)$$

where  $R_{HO}$  is the Hubbard-Onsager radius, given by:

$$R_{HO} = \frac{\tau e^2 (\varepsilon_0 - \varepsilon_\infty)}{16\pi\eta_0\varepsilon_0} \quad (5.5)$$

with  $\varepsilon_0$  and  $\varepsilon_\infty$  being the static and infinite frequency dielectric constant of the solvent, and  $\tau$  the dielectric relaxation time. The values of  $R_{HO}$  are 0.175 nm for DMSO and 0.183 nm for ACN at 298.15 K (92), indicating that the relation  $\eta(r)/\eta_0$  is lower for DMSO as compared with ACN, in agreement with the trend observed in Figure 5.10, where the Walden product decreases from DMSO to ACN.

For  $\text{LiPF}_6$ , the Walden product exhibits a minimum, not observed for  $\text{TBAPF}_6$ , for  $\chi_{ACN} \sim 0.95$ . If we hypothesize that the dielectric friction effect for  $\text{TBA}^+$  is similar to that for  $\text{Li}^+$ , the reduction in the Walden product for  $\text{LiPF}_6$  observed when decreasing the ACN content when going from  $\chi_{ACN} = 1$  to  $\chi_{ACN} = 0.95$  can be interpreted as an increment in the value of  $r$ . Considering, that  $\text{PF}_6^-$  behaves essentially as a non solvated ion, this increment can be considered fundamentally as an increment in the  $\text{Li}^+$  hydrodynamic radius. This can be hypothesized to be due to the fact that for  $\chi_{ACN} = 0.95$  the first solvation shell of the  $\text{Li}^+$  ion, which is formed by ACN molecules in pure ACN, is partially or totally replaced by the larger DMSO molecules.

### 5.5. Microelectrode study of oxygen diffusivity and solubility in mixed solvents.

**Literature overview.** We have studied the diffusivity and solubility of oxygen molecule in the DMSO, ACN and their mixtures. The literature search has shown the availability of these data for pure solvents, however to the best of our knowledge there is no data available for the mixtures of these solvents. The bibliographic experimental values of oxygen diffusion coefficient, the measurement methods and the conditions are summarized for the ACN and DMSO in the table 5.2 and 5.3 accordingly. The bibliographic experimental values for oxygen solubility in ACN and DMSO are depicted in the table 5.4. As can be seen, the diffusivity of oxygen in both solvents varies depending on the conducting salt type and concentration. For the DMSO; the reported values of oxygen diffusion coefficient are lying between  $9.75 \cdot 10^{-6}$  and  $7.49 \cdot 10^{-5}$  cm<sup>2</sup>/s with a medium value lying between  $2 \cdot 10^{-5}$  and  $3 \cdot 10^{-5}$  cm<sup>2</sup>/s. For the ACN, those values are in between  $2.1 \cdot 10^{-5}$  and  $11 \cdot 10^{-5}$  cm<sup>2</sup>/s with a medium reported value of about  $5 \cdot 10^{-5}$  to  $6 \cdot 10^{-5}$  cm<sup>2</sup>/s. As for the oxygen solubility, the reported values vary from 6-8 mM/l for the ACN and between 1 and 4 mM/l for the DMSO. While the both solubility and diffusivity of oxygen in both solvents vary significantly between different experimental conditions, the general trend is that the solubility and diffusivity of oxygen in about 3 times higher in the ACN than in DMSO that is reasonable considering that ACN has much lower viscosity that DMSO.

**Table.5.2. Bibliographic values for O<sub>2</sub> diffusion coefficient in ACN.**

Method	Conditions	Diffusion coefficient, cm <sup>2</sup> /s	Reference
CV RDE	0.1 TBAClO <sub>4</sub>	$7.05 \pm 0.53 \cdot 10^{-5}$ $7.03 \pm 0.45 \cdot 10^{-5}$	(170)
	LiPF <sub>6</sub> TBAPF <sub>6</sub>	$4.64 \cdot 10^{-6}$ $2.45 \cdot 10^{-5}$	(86)
	TBAPF <sub>6</sub> TBAClO <sub>4</sub>	$2.1 \cdot 10^{-5}$ $2.2 \cdot 10^{-5}$	(85)
Microelectrodes	0.1 TBAClO <sub>4</sub>	$9.2 \cdot 10^{-5}$	(171)
Au microelectrodes	0.1 TEAClO <sub>4</sub>	$11 \pm 1.2 \cdot 10^{-5}$	(172)

**Table.5.3. Bibliographic values for O<sub>2</sub> diffusion coefficient in DMSO.**

Method	Conditions	Diffusion coefficient, cm <sup>2</sup> /s	Reference
CV	0.1 TBAClO <sub>4</sub>	3.11 ± 0.09·10 <sup>-5</sup>	(170)
RDE		3.05 ± 0.35·10 <sup>-5</sup>	
	0.1 TEAClO <sub>4</sub> , 25°C	3.23·10 <sup>-5</sup>	(173)
	LiPF <sub>6</sub>	1.67·10 <sup>-5</sup>	(86)
	TBAPF <sub>6</sub>	9.75·10 <sup>-6</sup>	
Microelectrodes	TBAPF <sub>6</sub>	2.2·10 <sup>-5</sup>	(174)
	TBAClO <sub>4</sub>	2.3·10 <sup>-5</sup>	
	TBACF <sub>3</sub> SO <sub>3</sub>	1.8·10 <sup>-5</sup>	
	TBAN(CF <sub>3</sub> SO <sub>2</sub> ) <sub>2</sub>	4.7·10 <sup>-5</sup>	
Pt RDE	0.2 LiClO <sub>4</sub>	2.7·10 <sup>-5</sup>	(175)
	0.5 TBAClO <sub>4</sub>	7.49·10 <sup>-5</sup>	(176)
Au microelectrodes	0.2 TEAClO <sub>4</sub>	2.2±0.4·10 <sup>-5</sup>	(172)

**Table 5.4. Bibliographic values for O<sub>2</sub> solubility in ACN and DMSO.**

O <sub>2</sub> solubility in ACN, mM/l	O <sub>2</sub> solubility DMSO, mM/l	Reference
8.1	2.1	(122)
6.3±0.3		(171)
	TBAPF <sub>6</sub> 2.79	(174)
	TBAClO <sub>4</sub> 2.92	
	TBACF <sub>3</sub> SO <sub>3</sub> 3.89	
	TBAN(CF <sub>3</sub> SO <sub>2</sub> ) <sub>2</sub> 1.43	

Here we used ultramicroelectrodes (UMEs) because they possess advantageous properties as they allow obtaining simultaneously the diffusion coefficient and the solubility of electroactive species from single chronoamperometry(126).

**Radius of microelectrode.** Gold disc UMEs have been used throughout the experiments. The UME radius has been determined by performing the Cyclic Voltammetry at 10 mV/s in the solution containing 2 mM of ferrocene in 0.1 M TBAPF<sub>6</sub> in ACN. The resulting CV recorded independently 6 times are shown on the figure 5.11. It can be seen that voltametric response results in a steady state current of about 20 nA, as expected for the typical current-potential curve at UME.

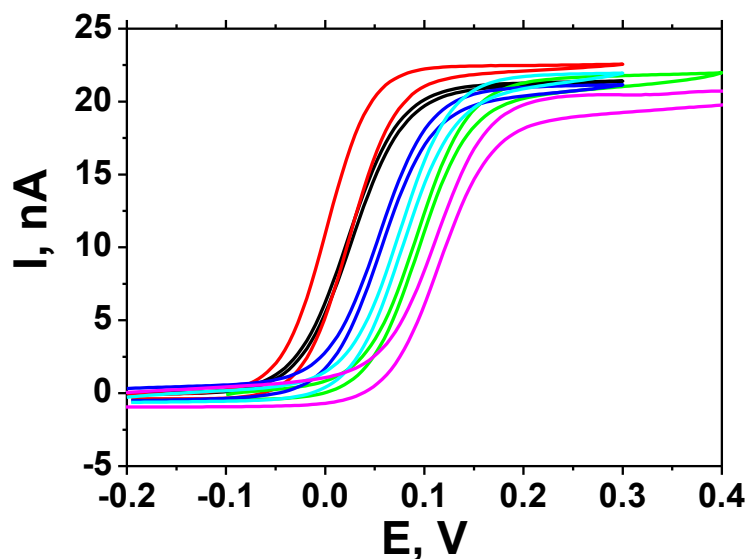


**Figure 5.11. CVs performed in solution 2 mM of ferrocene in 0.1 M TBAPF<sub>6</sub> in ACN, 10 mV/s. Six independent identical experiments are shown.**

The radius of microelectrode was calculated with the stationary limiting current according to the formula:

$$i_{ss} = 4\pi nFD_oC_o r_o \quad (5.6)$$

where  $i_{ss}$  is the limiting current obtained from the CV,  $n$  is the number of electrons ( $n=1$  for the reaction ferrocene/ferrocenium ion),  $F$  is the Faraday constant,  $D_o$  and  $C_o$  are the diffusion coefficient ( $D=2.24 \cdot 10^{-5} \text{ cm}^2/\text{s}$  (177)) and concentration of ferrocene respectively,  $r_o$  is the radius of microelectrode. The average of six measurements, value of microelectrode radius was calculated as 12.4  $\mu\text{m}$  (see table 5.5) and this value was used for the rest of the measurements.

**Table 5.5. Calculated microelectrode radius.**

Experiment	$i_{ss}$ , A	r, $\mu\text{m}$	Area $\pi r^2$ , $\text{m}^2$
1	2.10E-08	12.15	4.63E-10
2	2.25E-08	13.01	5.32E-10
3	2.15E-08	12.43	4.86E-10
4	2.10E-08	12.15	4.63E-10
5	2.20E-08	12.72	5.08E-10
6	2.05E-08	11.86	4.41E-10
Average		12.39	4.82E-10

**Microelectrode studies in oxygen saturated ACN, DMSO and their mixtures.** The cyclic voltammetry performed in the DMSO, both deoxygenated and oxygenated at different bubbling times are depicted in the figure 5.12. As expected, in the absence of oxygen, the current is negligible in the entire potential scan, however after bubbling the oxygen for 5 min a plateau with a steady state current is observed around -15 nA, that corresponds to the reversible oxygen reduction to superoxide anion ( $n = 1$ ). After the oxygenating for 10 or more minutes, the steady state current has increased to -30 nA, thus we concluded that 10 min was a sufficient oxygenation time in the experimental setup used. Then oxygen was kept over the solution to keep saturation conditions.

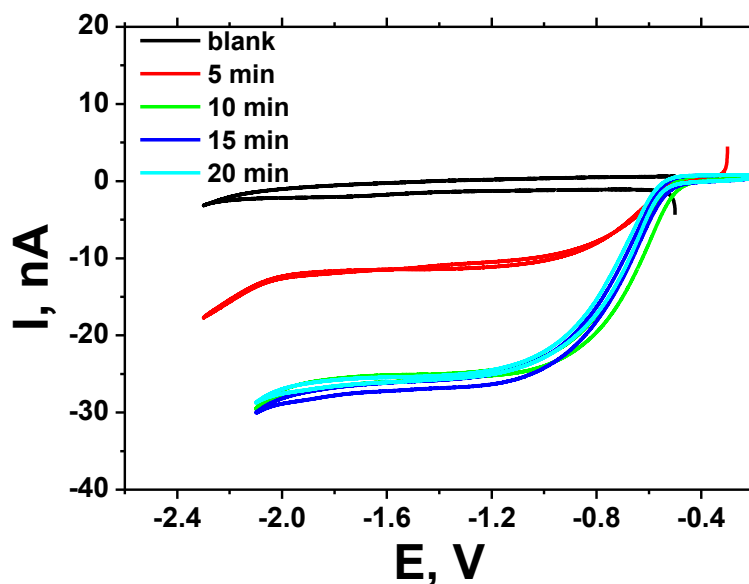


**Figure 5.12.  $O_2$  reduction in 0.1 M TBAPF<sub>6</sub> DMSO as a function of oxygenation time**

The same experiment was performed for the ACN solution. As in the case with DMSO, we had found 10 min to be sufficient time to saturate the solution with oxygen. Note, that the current plateau is observed at around -300 nA, that is one order of magnitude higher than in the DMSO-based solutions as a result of both higher diffusivity and solubility of oxygen in acetonitrile. (see figure 5.13).

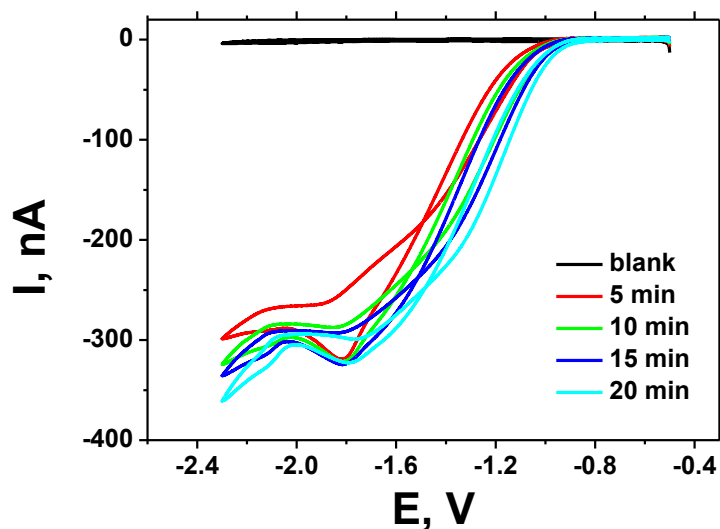


**Figure 5.13. O<sub>2</sub> reduction in 0.1 M TBAPF<sub>6</sub> ACN as a function of oxygenation time.**

Notably, in the both solvents reversible superoxide formation is observed with the superoxide anion stabilized by tetrabutylammonium cation. However, the remarkably different behavior is observed when trace lithium ion is added to the DMSO-based solution, thus making it impossible to perform UMEs studies on oxygen diffusivity and solubility in the lithium containing solutions. As can be seen in the figure 5.14, when adding some Li<sup>+</sup> cation, the ORR wave falls to 0 with a consequent passivation of the electrode surface by insoluble products. These results are in agreement with the ORR mechanism in non-aqueous solvents discussed in the previous chapter.

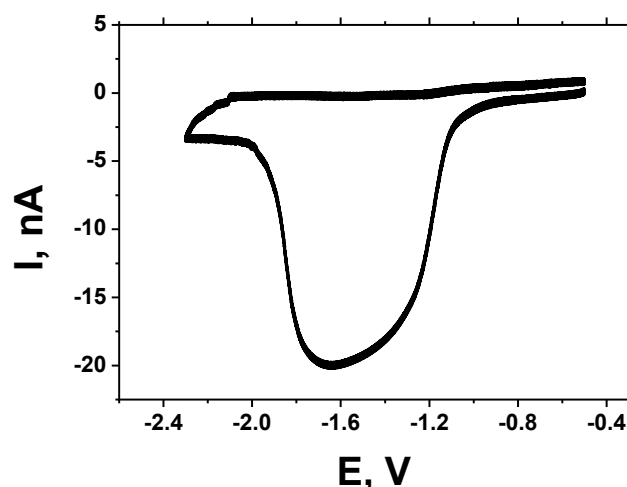


**Figure 5.14. O<sub>2</sub> reduction in 0.1 M TBAPF<sub>6</sub> DMSO, contaminated with Li<sup>+</sup>.**

The CVs performed in the oxygen saturated 0.1 M TBAPF<sub>6</sub> solution in pure DMSO and ACN, and their mixtures with 24%, 53% and 80% mole fraction of ACN, are presented on the figure 5.15 The peak on the reverse scan was observed sometimes, especially for the ACN-rich solutions. We suggested that this phenomena could be explained by the water contamination (trace water may destabilize the superoxide anion to form oxygen and hydrogen peroxide) and also the change of the effective microelectrode radius by absorbed species.

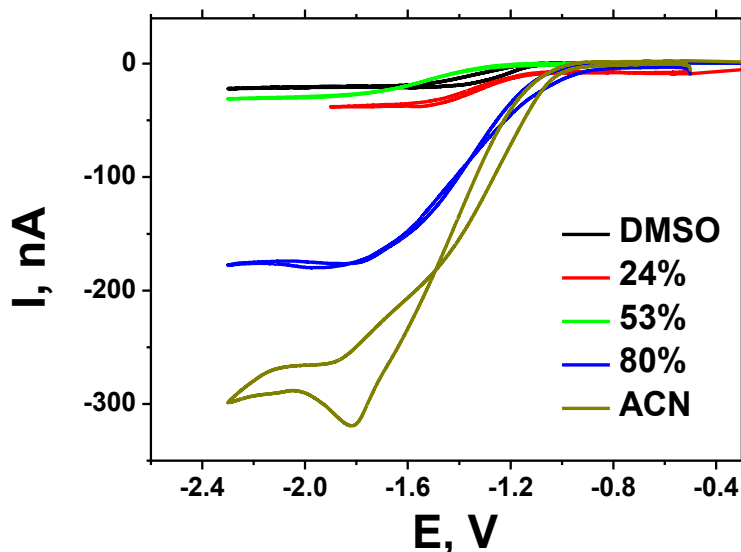


**Figure 5.15. CVs of O<sub>2</sub> reduction in 0.1 M TBAPF<sub>6</sub> in mixtures DMSO-ACN as a function of mole fraction of ACN**

After recording the corresponding CV experiments, the single potential step chronoamperometric experiments were performed. In the typical experiment, the potential was held for 0,5 s at the potential where ORR occurs (we used various potential values in the -1,8 and -2,3 V range).

The time-dependent current response obtained was analyzed and fitted in Origin software (Microcalc) by using the following equations, as proposed by Shoup and Szabo (178), which sufficiently describe the current response,  $I$ , over the entire time:

$$I = -4nFDcr_{df}(\tau), \quad (5.7)$$

$$f(t) = 0.7854 + 0.8863\tau^{-1/2} + 0.2146\exp(-0.7823\tau^{-1/2}), \quad (5.8)$$

where  $n$  is number of electrons,  $F$  is the Faraday constant,  $D$  is the diffusion coefficient and  $c$  is the initial concentration,  $r_d$  is the radius of the microdisc and the dimensionless time parameter,  $\tau$ , is given by:

$$\tau = 4Dt/r_d^2. \quad (5.9)$$

Notice that both parameters  $c$  and  $D$  can be obtained from the non linear fit since they appear as a product and  $D$  in the limiting current and also in the dimensionless time,  $\tau$ , unlike chronoamperometry with semi-infinite diffusion at large plane electrodes where the Cottrell eqn. convolutes  $c \cdot D^{1/2}$  (126).

For the Shoup and Szabo fitting, the time interval between 0,1 and 0,5 s of chornomaperometric transient was chosen, the example of the transient and its fit in the DMSO solvent are shown on the figure 5.16.

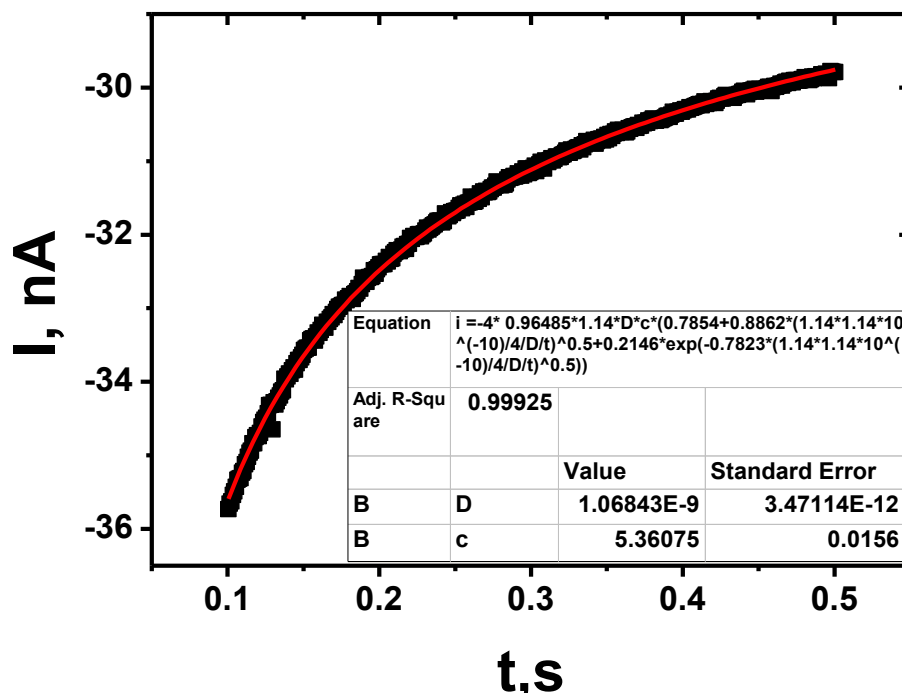


**Figure 5.16. An example of experimental chronoamperometric transient (in black) and Shoup and Szabo fit (red line) in oxygen saturated 0.1 M TBAPF<sub>6</sub> DMSO. Inset table shows fitted values of  $D$  (oxygen diffusion coefficient) and  $C$  (oxygen concentration).**

For each solvent and solvent mixture, the D and C were determined for at least 8 times, and the average values with a standard deviation were calculated. The experimentally determined oxygen diffusion coefficients for the ACN, DMSO and their mixtures are compiled in the table 5.6 and are depicted on the figures 5.17 and 5.18, respectively.

**Table 5.6. Experimental values of oxygen diffusion coefficient and diffusivity in the oxygen saturated 0.1 M TBAPF<sub>6</sub> containing ACN, DMSO and their mixtures.**

$\chi_{\text{ACN}}$ in ACN-DMSO mixture	$D_{\text{O}_2}, 10^{-5} \text{ cm}^2/\text{s}$	$C_{\text{O}_2}, \text{ mM/l}$
0 (DMSO)	$1.43 \pm 0.49$	$4.32 \pm 1.07$
0.25	$3.22 \pm 1.03$	$2.73 \pm 2.60$
0.53	$2.37 \pm 0.82$	$3.11 \pm 1.19$
0.8	$1.85 \pm 0.50$	$21.93 \pm 6.53$
0.9	$3.83 \pm 0.71$	$14.22 \pm 3.46$
1 (ACN)	$6.26 \pm 2.01$	$6.74 \pm 2.80$

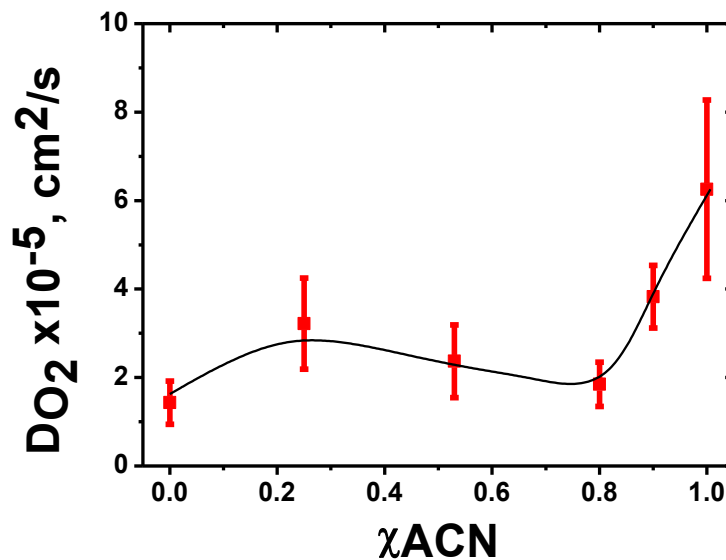


**Figure 5.17. Experimental oxygen diffusion coefficient as a function of mole fraction of ACN in ACN-DMSO mixtures. Black curve was added to guide the eye.**

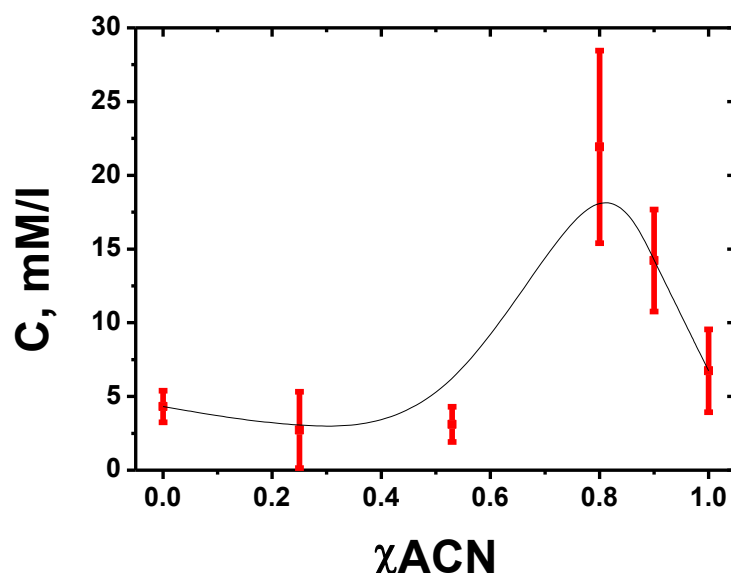


**Figure 5.18. Experimental oxygen concentration as a function of mole fraction of ACN in ACN-DMSO mixtures. Black curve was added to guide the eye.**

We determined the  $D_{O_2}$  in DMSO equal to  $(1.43 \pm 0.49) \cdot 10^{-5} \text{ cm}^2/\text{s}$  and  $D_{O_2}$  in ACN equal to  $(6.26 \pm 2.01) \cdot 10^{-5} \text{ cm}^2/\text{s}$ , that is within the error is in agreement with previously reported results. Notably, the dependence of oxygen diffusion coefficient is not lineal as a function of ACN mole fraction, however a significant decrease from  $(6.26 \pm 2.01) \cdot 10^{-5} \text{ cm}^2/\text{s}$  to  $(1.85 \pm 0.50) \cdot 10^{-5} \text{ cm}^2/\text{s}$ , is observed in the region 0,8-1  $\chi_{ACN}$ . However in the range 0 - 0.8 ACN mole fractions the oxygen diffusion coefficient does not vary much and lies in between  $1 \cdot 10^{-5}$  to  $3 \cdot 10^{-5} \text{ cm}^2/\text{s}$  (see figure5.17).

As for the oxygen solubility, the values were determined as  $4.32 \pm 1.07 \text{ mM/l}$  in DMSO and  $6.74 \pm 2.80 \text{ mM/l}$  in ACN. In comparison to the literature, the oxygen solubility in ACN is in very good agreement with previously reported values; however the oxygen solubility in DMSO is somewhat higher than normally reported in the literature. Notably, the oxygen solubility is neither lineal in the ACN-DMSO mixtures range, and a very pronounced increase is observed in the range 0.8-1  $\chi_{ACN}$ .

These observed phenomena, a sharp decrease of oxygen diffusion coefficient and significant increase in oxygen solubility could be explained by the preferential solvation of oxygen by

DMSO molecules in ACN. The very similar phenomena was observed and reported by Compton group in the mixtures ACN-H<sub>2</sub>O, and was also explained it by the preferential solvation of oxygen by water molecules in ACN(171).

The effect of preferential solvation of oxygen molecules in the solvent mixtures is very important for the electrolyte formulation for the Li-air battery, as conditions with optimum oxygen solubility and diffusivity may be selected

## 5.6. Conclusions.

In this chapter we have explored the mixed electrolyte systems for Li-air battery applications. We have studied the effects of mixed electrolyte composition on the solvation of two principal reactants: lithium ions and oxygen molecule.

We have concluded, by redox potential of the Li/Li<sup>+</sup> electrode and electrical conductivity of LiPF<sub>6</sub> and TBAPF<sub>6</sub> measurements in ACN–DMSO mixtures, that lithium ion is preferentially solvated by DMSO even for very small mole fractions of DMSO in ACN. This preferential solvation effect is of great importance since it stabilizes the superoxide ion preventing the disproportionation of lithium superoxide ( $2 \text{O}_2\text{Li} \rightarrow \text{Li}_2\text{O}_2 + \text{O}_2$ ).

On the other hand, we have studied with the use of microelectrodes, the oxygen diffusivity and solubility in the ACN-DMSO mixtures. The significant decrease of oxygen diffusion coefficient and anomalous increase in oxygen solubility was observed in the range 0.8 – 1 mole fraction of ACN. We have suggested that those phenomena could be explained, similarly to the Li<sup>+</sup>, with the preferential solvation of oxygen by DMSO molecules in the access of ACN.

Our study of DMSO-ACN as a model system is very relevant for the optimization of the electrolytes for Li-air batteries, since it could help to find an adequate electrolyte solvent composition which prevents the disproportionation of lithium superoxide, minimize solvent oxidation by reactive oxygen species, while optimizing conductivity and oxygen solubility values.

## 5.7. Resumen en castellano del capítulo 5. La exploración de sistemas de electrolitos mixtos para baterías de Litio-aire y el efecto de la solvatación del ion $\text{Li}^+$ .

Es conocido que la naturaleza del solvente y el material del cátodo influyen en el mecanismo de electroreducción del oxígeno, tal como en la estabilidad del solvente. En el capítulo anterior fue demostrado que la reducción de oxígeno ocurre por un mecanismo distinto en solventes como acetonitrilo (ACN) y dimetil sulfóxido (DMSO). El ion superóxido  $\text{O}_2^-$  que es el producto intermediario de electroreducción de oxígeno, es más estable en DMSO y se detecta en anillo del electrodo rotatorio de disco y anillo, mientras que no se detecta en acetonitrilo. En este capítulo hemos demostrado que aunque en ACN puro no es posible detectar el superóxido en el anillo, el agregado de bajas concentraciones de DMSO (tales como 0.1M DMSO en ACN) resultan en la detección de superóxido en el anillo. Los resultados electroquímicos han sugerido que el DMSO solvata preferencialmente los iones de  $\text{Li}^+$ . Para analizar esta hipótesis se ha estudiado la solvatación de  $\text{Li}^+$  en mezclas DMSO-ACN por medio de técnicas experimentales, complementándolas con simulaciones computacionales. Se estudiaron entonces las propiedades de los reactivos que intervienen en la reacción del cátodo: ion litio ( $\text{Li}^+$ ) y la molécula de oxígeno ( $\text{O}_2$ ) en ACN, DMSO y en mezclas de ambos. Se midió la relación del potencial de  $\text{Li}/\text{Li}^+$  con la fracción molar de acetonitrilo como así también la conductividad de  $\text{LiPF}_6$  en mezclas de ACN-DMSO desde ACN puro hasta DMSO puro. Se determinó la conductividad a dilución infinita  $\Lambda_0$  de la sal en función de la fracción molar de acetonitrilo usando la ecuación de Fuoss-Hsia Fernandez Prini (FHFP). Se determinó el producto de Walden y el radio hidrodinámico medio de la sal.

A partir de simulaciones de dinámica molecular, se analizó la solvatación preferencial del DMSO aún en mezclas ricas en ACN y se determinaron tanto el coeficiente de difusión del ion  $\text{Li}^+$  como la energía libre de Gibbs requerida para ionizar un átomo de Li a  $\text{Li}^+$ . Se concluyó que los iones  $\text{Li}^+$  se encuentran solvatados por 4 moléculas de DMSO en las concentraciones mayores a 3%.

Hemos encontrado que los resultados experimentales de electrodo rotatorio de disco y anillo, las medidas de la conductividad eléctrica y las simulaciones están de acuerdo y se complementan.

Por otro lado, con el uso de microelectrodos de Au se midió los coeficientes de difusión y solubilidad de oxígeno. Mientras que en ACN el O<sub>2</sub> posee un mayor coeficiente de difusión y solubilidad que en DMSO, la variación de dichas propiedades no es lineal con la fracción molar del solvente en la mezcla, probablemente por los efectos de solvatación preferencial del oxígeno.

Para concluir, en este capítulo se mostró y analizó el efecto del solvente en los reactivos y los productos de la reacción de electroreducción de oxígeno y la ventaja del uso de un electrolito mixto como estudio relevante para el desarrollo de la batería no-acuosa de Li-aire. Los resultados indican una solvatación preferencial del ion Li<sup>+</sup> por moléculas de DMSO en mezclas de DMSO-ACN aun para altas fracción molares de ACN. Asimismo, se observó una solvatación preferencial de moléculas oxígeno por DMSO incluso en exceso de ACN. Estos resultados son de fundamental interés para el desarrollo de las baterías de litio-aire y brindan una mayor comprensión de los mecanismos básicos de la electroreducción de oxígeno en solventes no-acuosos.

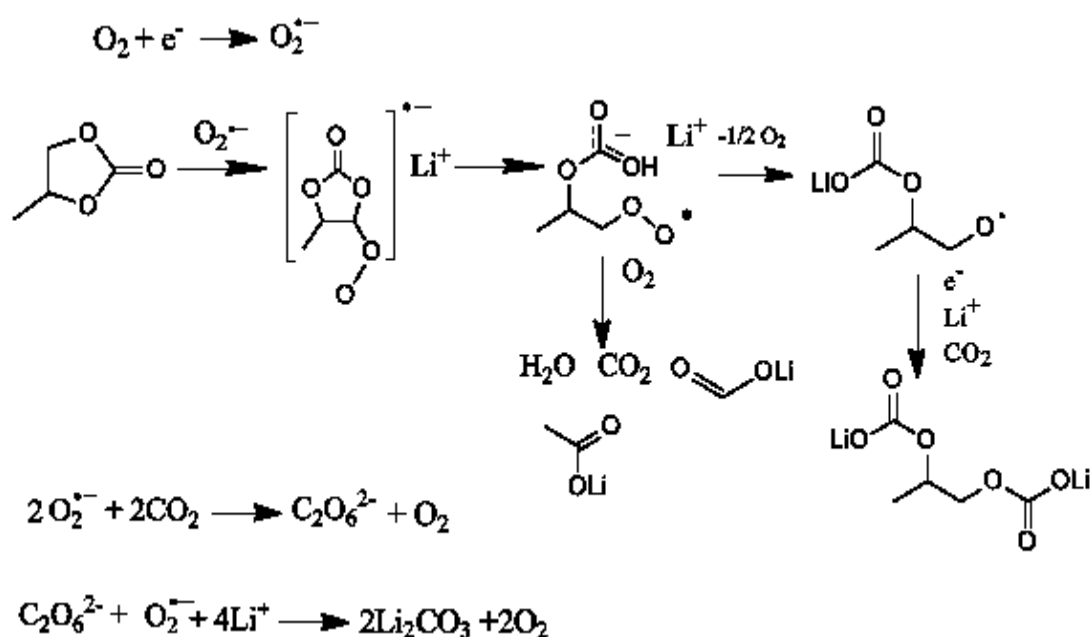
# CHAPTER 6. Investigation of the solvent's instability in the Li-air battery.

## 6.1. Introduction.

The solvent's instability in the presence of reactive reduced oxygen species is widely recognized as one of the most challenging issues facing the Li-air technology.

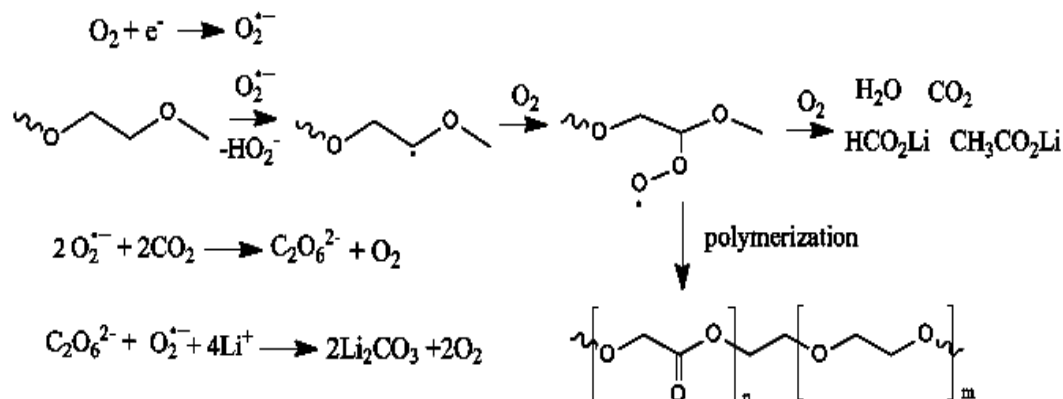
As mentioned in the introduction chapter, various electrolyte systems were proposed and all of them were found to decompose to a less or higher degree.

It has been suggested that organic carbonate electrolytes decompose chemically due to reaction with superoxide according to the following mechanism(47):



The only disadvantage of this mechanism is that the life of superoxide anion is very short in the presence of  $Li^+$ .

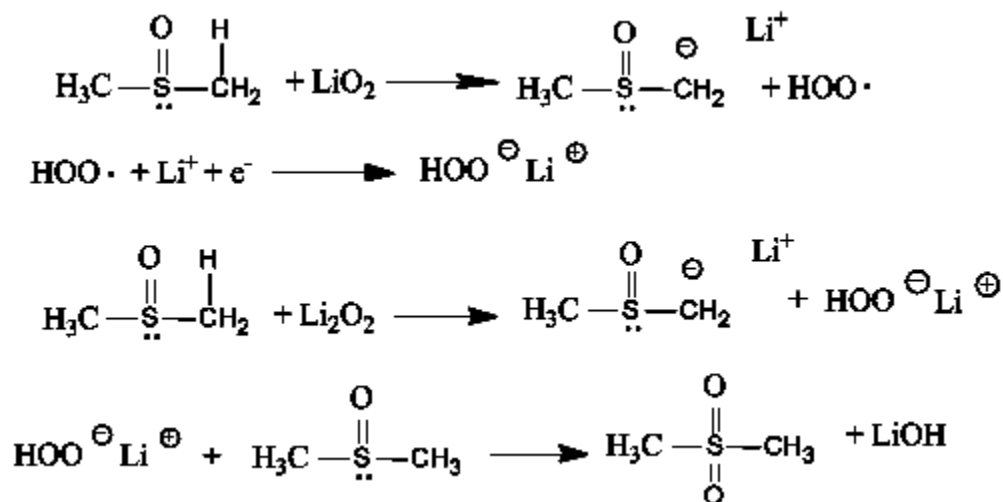
For organic ethers, the following decomposition mechanism via hydrogen abstraction by superoxide has been proposed(159):



However Sharon et al. argued this mechanism; based on previous numerous studies on superoxide, they stated that: superoxide does not abstract hydrogen atoms.(12)

Instead, they have suggested that decomposition results from the nucleophilic attack of  $\text{Li}_2\text{O}_2$  on the triglyme (51).

In other study, Sharon et al. proposed a scheme of DMSO decomposition in the presence of  $\text{Li}^+$  ions(54):



In this chapter we have used spectroelectrochemical techniques, mainly in situ SNIFTIRS, couples to the electrochemical cell, in order to reveal parasitic reactions occurring during the ORR and OER in the Li-air cell.

## 6.2. Infrared spectroscopy studies on the stability of dimethyl sulfoxide for application in a Li-air battery.

Dimethyl sulfoxide (DMSO) was investigated as a possible aprotic solvent in lithium electrolyte for Li-air battery in 2010 by Laoire and co-workers; they demonstrated an increased stability of oxygen reduction species in this media (86). In 2012, several reports showed DMSO-based Li-air cells with promising electrochemical performance and also an increased stability of this electrolyte system with porous carbon(179) and gold (36) cathodes. Also in 2013, Trahan et al.(53) determined that DMSO is a practical solvent based on rotating disk electrode (RDE) and rotating ring-disk electrode (RRDE) cyclic voltammetry studies; they also reported a DMSO-based Li-air cell with a carbon cathode. In a 2013 we reported that soluble superoxide radical anions can be detected at a ring electrode of a RRDE system in lithium solutions of acetonitrile containing 0.1 M DMSO, unlike acetonitrile lithium electrolytes that show no evidence of soluble  $O_2^-$ .(58) It has been suggested that soluble superoxide can nucleophilically attack the solvent. However, in 2013 there was no evidence of the stability of DMSO based electrolytes for application in the Li-air battery. Further investigation was required because it has been reported before that DMSO in the presence of superoxide anions may undergo oxidation to dimethyl sulfone ( $DMSO_2$ ). As early as 1968, Goolsby and Sawyer(180) studied the oxygen reduction reaction in DMSO on gold, platinum, and mercury electrodes. They reported that the electrochemical reduction of superoxide in DMSO in the presence of  $(C_2H_5)_4NClO_4$  (tetraethylammonium perchlorate) produces dimethyl sulfone. This was concluded based on infrared data obtained during the large scale reduction of oxygen at  $-2.05$  V with evidence in the appearance of an IR peak at  $8.81 \mu m$  ( $1135 cm^{-1}$ ), which is characteristic of dimethyl sulfone. They suggested the following reaction:



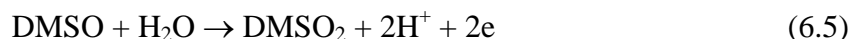
In 1982, Gampp and co-workers (181) reported superoxide first order decomposition in DMSO with a half-life of 100 h to yield dimethyl sulfone, and sulfone was obtained after storage for two months at room temperature. The following decomposition mechanisms were suggested:



or

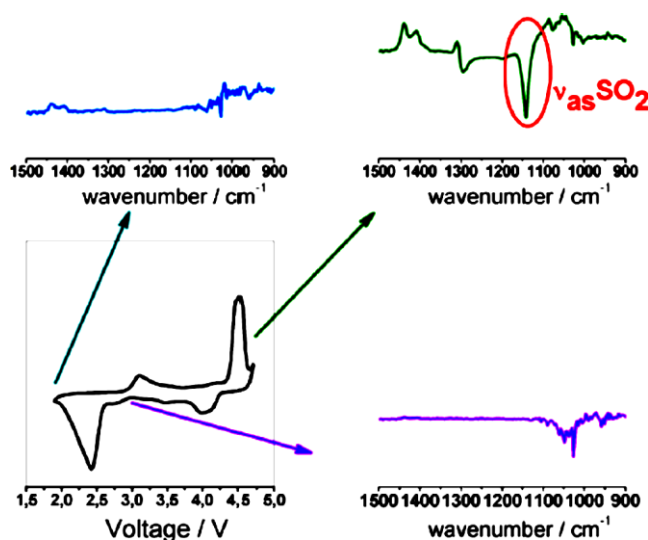


In 1995, the anodic oxidation of DMSO in lithium perchlorate, fluoroborate, and potassium tetrafluorophosphate on Pt and glassy carbon electrodes were studied with in situ Fourier transform infrared (FTIR) spectroscopy in the presence of traces of water (strong absorption band in the (1100–1000  $\text{cm}^{-1}$ ))(182).



In this chapter, in situ infrared spectroscopy experiments were performed simultaneously with electrochemical experiments to investigate the DMSO-based electrolyte stability versus two Li–air cell discharge products, soluble superoxide anion and insoluble lithium peroxide, as well as anodic oxidation of DMSO, using Au and Pt as the cathode material. We performed the experiments in solutions of DMSO containing  $\text{Li}^+$  salts and saturated in  $\text{O}_2$ , in solutions of tetrabutylammonium ( $\text{TBA}^+$ ) salts saturated in  $\text{O}_2$ , and in deoxygenated solutions.

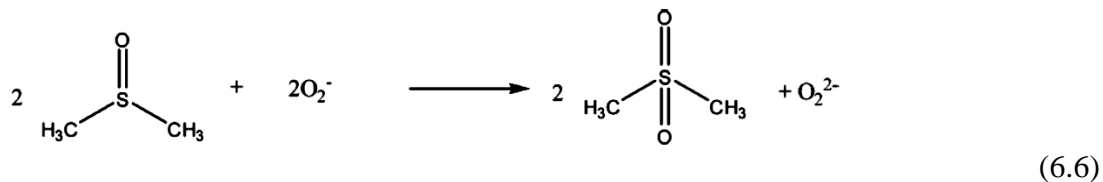
The schematic representation of in situ IR studies explained in this chapter is shown on the figure 6.1.



**Figure 6.1. Schematic representation of in situ IR studies for Li-air system.**

**IR Transmission Spectra of DMSO in the Presence of  $O_2^-$  and  $Li_2O_2$ .** A saturated solution of  $KO_2$  in DMSO and a suspension of  $Li_2O_2$  in DMSO (because lithium peroxide is insoluble in DMSO) were prepared. IR spectra of the prepared solutions were measured 24 h and two months after preparation. A spectrum of pure DMSO was also measured as a reference. The obtained spectra are shown in Figure 6.2. The spectrum of DMSO exhibits peaks at 1438, 1405, and 1310  $cm^{-1}$  and a broad peak at around 1075  $cm^{-1}$ . The peaks at wavenumber 1438 and 1405  $cm^{-1}$  correspond to the antisymmetric bending of  $CH_3$  ( $\delta_{as}CH_3$ ), and the peak at 1310  $cm^{-1}$  is identified as a symmetric deformation of  $CH_3$  ( $\delta_sCH_3$ ) group that is attached to the S atom. A broad peak around 1075  $cm^{-1}$  can be assigned as S=O stretching ( $\nu_{SO}$ ). The spectra of both solutions taken 24 h after the preparation are similar to the spectrum of pure DMSO. Furthermore, the spectrum of a mixture of DMSO and  $Li_2O_2$  remains without noticeable changes after 2 months. On the other hand, the solution containing DMSO and  $KO_2$ , after a two month period, exhibits an IR spectrum with new peaks at 1335, 1293, and 1142  $cm^{-1}$ . A peak at 1142  $cm^{-1}$  can be assigned to the symmetric stretching of  $SO_2$  ( $\nu_sSO_2$ ) and is a characteristic peak of dimethyl sulfone ( $DMSO_2$ ).<sup>(183, 184)</sup> The modes with wavelengths of 1293 and 1335  $cm^{-1}$  correspond to the asymmetric stretching of  $SO_2$  group ( $\nu_{as}SO_2$ ). Also, comparison of these spectra with standard spectra of DMSO and  $DMSO_2$  <sup>(185)</sup> makes it easy to identify that the obtained spectrum corresponds to a mixture of dimethyl sulfoxide and sulfone. Therefore, we conclude that no significant changes in the DMSO solvent occur on short time scales (24 h) in the presence of superoxide anion or in the presence of lithium peroxide precipitate. But on long time scales, DMSO undergoes decomposition in the presence of superoxide anion to form dimethyl sulfone. However, in the presence of  $Li_2O_2$ , no changes could be detected after a two month period.

It can be assumed that DMSO undergoes oxidation to  $DMSO_2$  according to the following reaction:



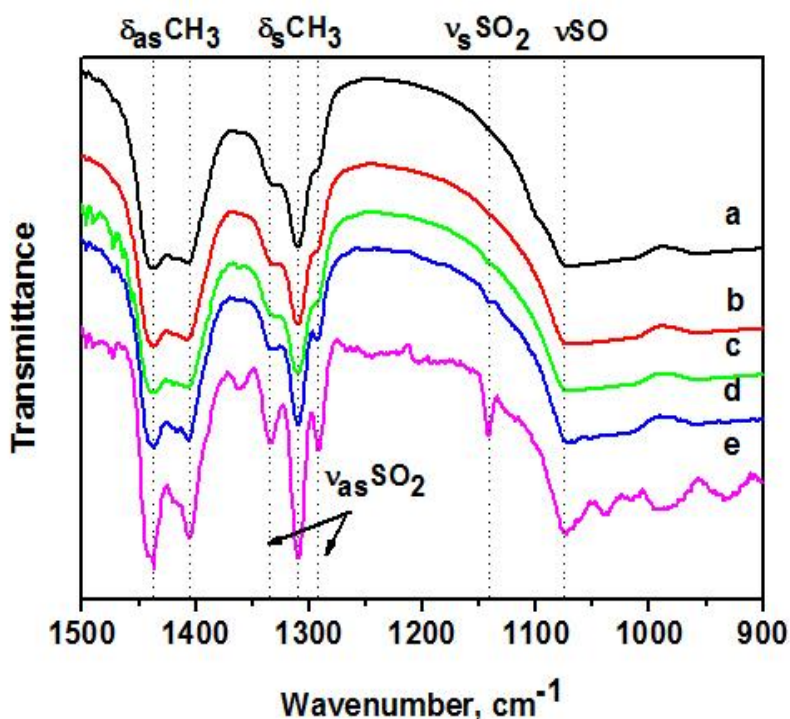


**Figure 6.2. IR spectra of solutions: (a) pure DMSO; (b) DMSO with  $\text{Li}_2\text{O}_2$ , measured 24 h after preparation; (c) DMSO with  $\text{KO}_2$ , measured 24 h after preparation; (d) DMSO with  $\text{Li}_2\text{O}_2$ , measured two months after preparation; (e) DMSO with  $\text{KO}_2$ , measured two months after preparation.**

It is hard to estimate the effect of this slow reaction on the rechargeability of the Li-air battery because the lifetime of superoxide anion is very short in the presence of  $\text{Li}^+$ . To investigate this issue, spectroelectrochemical in situ IR experiments were performed using Au and Pt working electrodes.

**In Situ IR Spectroscopy Results on Au.** For the in situ SNIFTIRS experiment, a set of fixed potentials were applied to the cathode and the IR spectra were collected at each chosen potential in order to evaluate changes produced in the electrolyte.

Potentials were chosen according to the cyclic voltammetry (CV) data, performed in the  $\text{O}_2$  saturated solutions of 0.1 M  $\text{LiPF}_6$  in DMSO (Figure 6.3). For in situ IR experiments we chose potentials between 3.2 and 1.9 V on the forward scan (discharge) and between 3.0 and 4.8 V on the reverse scan (recharge). A potential of 3.2 V is about the open circuit potential of the Li-air

battery where electrochemical reaction occurs according to the cyclic voltammetry results. At potentials between 2.8 and 1.9 V, reduction of  $O_2$  to superoxide anion(36) and its disproportionation to peroxide in the presence of Li occur.(186) In the potential range of the reverse CV scan, we have taken IR spectra at 3.0 and 3.8 V; those are potentials before and after the oxidation peak of surface  $O_2$  reduction product,  $LiO_2$  and/or  $Li_2O_2$ . At potentials between 4.2 and 4.8 V, the anodic oxidation of the solvent and possible oxidation of remaining surface  $O_2$  reduction products occur.

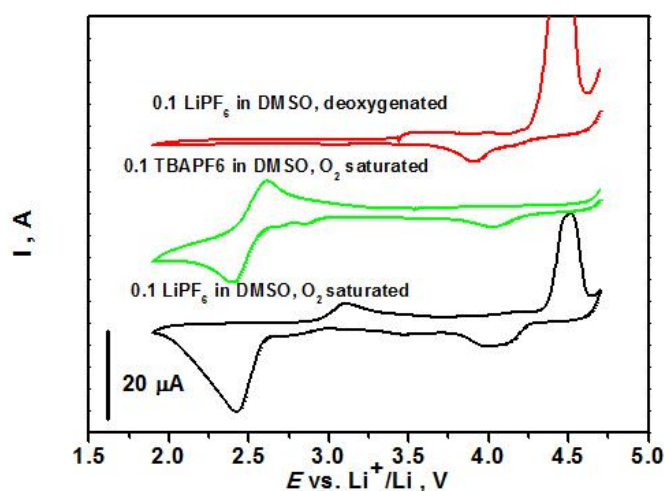


**Figure 6.3. CV performed on Au electrode in the solutions of 0.1 M  $LiPF_6$  in DMSO saturated in  $O_2$ , 0.1 M  $LiPF_6$  in DMSO deoxygenated, and 0.1 M TBAPF<sub>6</sub> in DMSO saturated in  $O_2$ .**

The resulting IR spectra of experiments performed in a 0.1 M  $LiPF_6$  solution in DMSO, saturated in  $O_2$  on a Au electrode are presented in Figure 6.4. In the SNIFTIR spectra, negative peaks (downward) correspond to the compounds that are formed. Positive peaks (upward) correspond to the modes that disappear. It is seen that on the forward scan at potentials between 3.2 and 1.9 V (discharge) and on the reverse scan at 3.0 and 3.8 V no changes in the IR spectrum, and thus in the composition of the solvent, occur near the electrode. However, during the recharge, application of potentials higher than 4.2 V results in clear detection of negative peaks at  $1142\text{ cm}^{-1}$  (symmetric stretching vibration of  $SO_2$  group) and  $1295\text{ cm}^{-1}$  (asymmetric stretching vibration of  $SO_2$  group). Note that the peak intensity increases with an increase in the anodic

potential. These modes may be identified as a DMSO<sub>2</sub> formation and correspond to potentials where a clear anodic current is observed (Figure 5.3). Positive peaks at 1310, 1408, and 1438 cm<sup>-1</sup> (Figure 6.4) are detected and can be assigned to the symmetric and asymmetric δ-CH<sub>3</sub> bending vibration, corresponding to DMSO that is being consumed in the anodic process. At higher wavenumbers, we detect two downward peaks at 2920 and 3010 cm<sup>-1</sup> and two upward peaks at 2910 and 2990 cm<sup>-1</sup>. Those might be attributed to the shifting of symmetric and asymmetric C–H stretching vibrations while oxidizing DMSO to DMSO<sub>2</sub>. This is in a good agreement with standard spectra of DMSO and DMSO<sub>2</sub>. Also at the potentials higher than 4.2 V, a positive peak at around 3500 cm<sup>-1</sup> is detected. That may be assigned to the O–H stretching and could be explained as depletion of trace water.

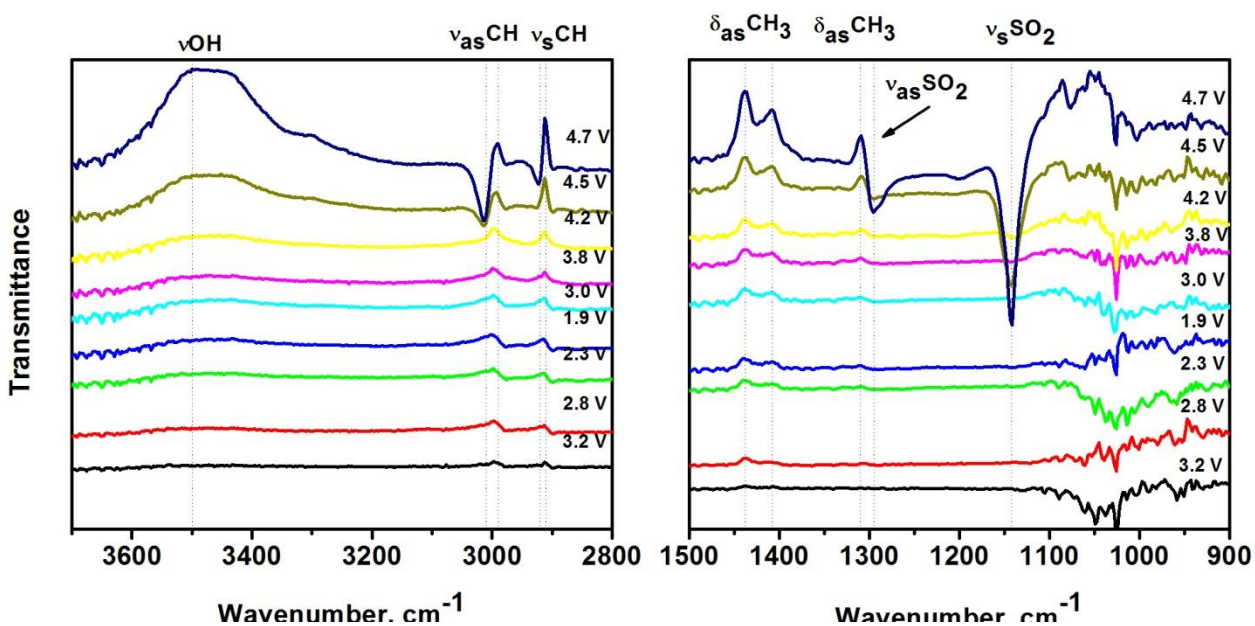


**Figure 6.4.** In situ IR spectra taken in a solution of 0.1 M LiPF<sub>6</sub> in DMSO, saturated in O<sub>2</sub> on a Au working electrode. Wavenumber ranges are 3700–2800 cm<sup>-1</sup> and 1500–900 cm<sup>-1</sup>.

The same set of potentials have been applied in the in situ SNIFTIRS experiments of 0.1 M TBAPF<sub>6</sub> solution in DMSO saturated with O<sub>2</sub> and also in a deoxygenated 0.1 M LiPF<sub>6</sub> solution in DMSO to evaluate the possible differences in electrolyte decomposition in the absence of Li<sup>+</sup> cations and O<sub>2</sub> molecules. Current-potential curves measured in these solutions are shown in Figure 6.3. SNIFTIRS results of a 0.1 M TBAPF<sub>6</sub> O<sub>2</sub> saturated solution in DMSO are depicted in

Figure 6.5. No considerable differences can be noticed when compared to the IR spectra results obtained in O<sub>2</sub> saturated 0.1 M LiPF<sub>6</sub> solution in DMSO as described above.

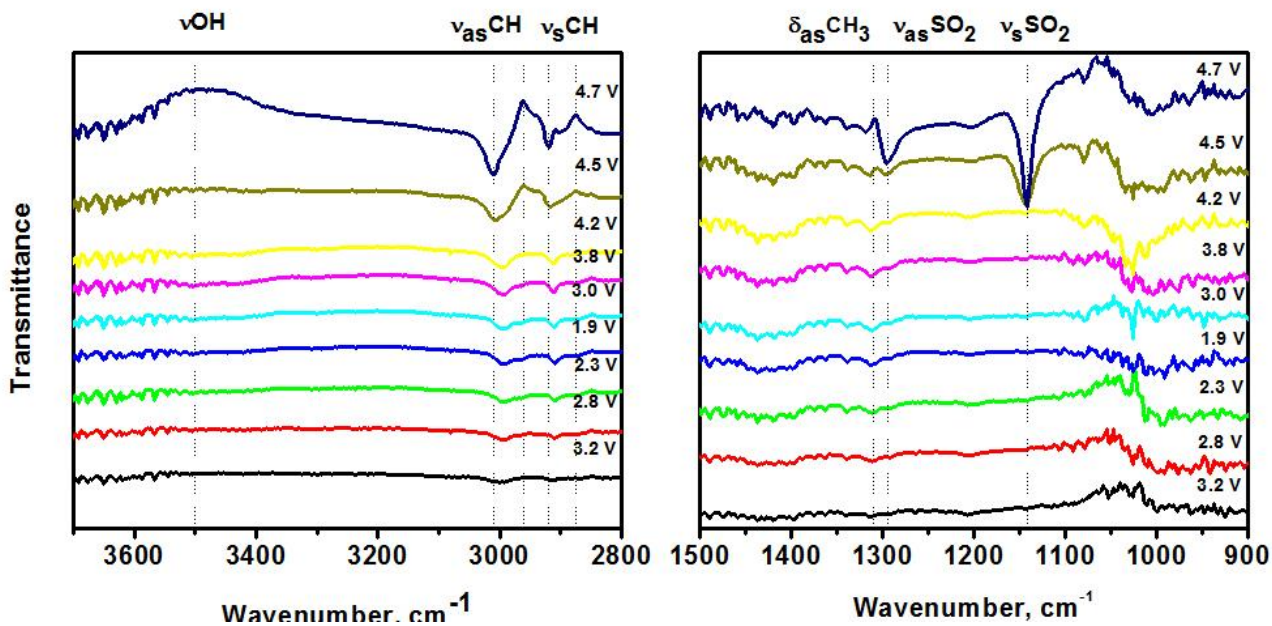


Figure 6.5. In situ IR spectra of a solution of 0.1 M TBAPF<sub>6</sub> in DMSO, saturated in O<sub>2</sub> on Au. Wavenumber ranges are 3700-2800 cm<sup>-1</sup> and 1500-900 cm<sup>-1</sup>.

Identical results have been observed in oxygen free electrolyte (Figure 6.6).

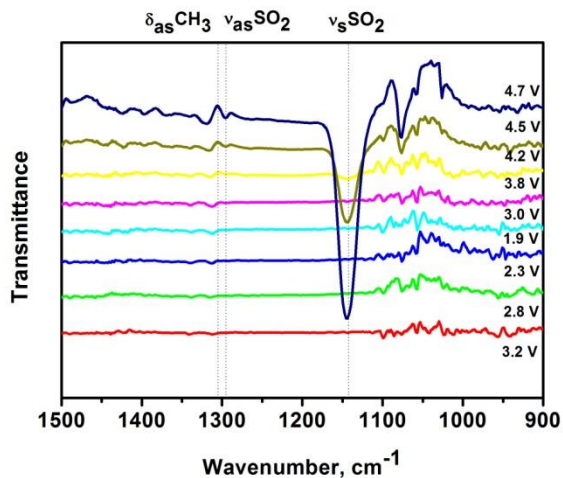
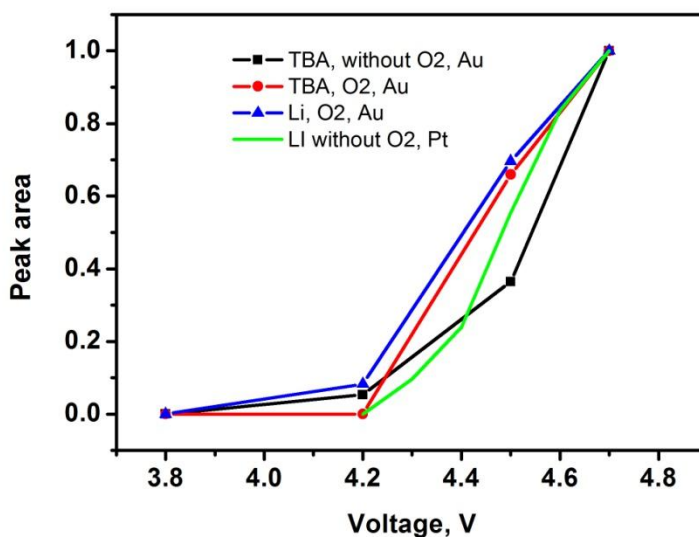


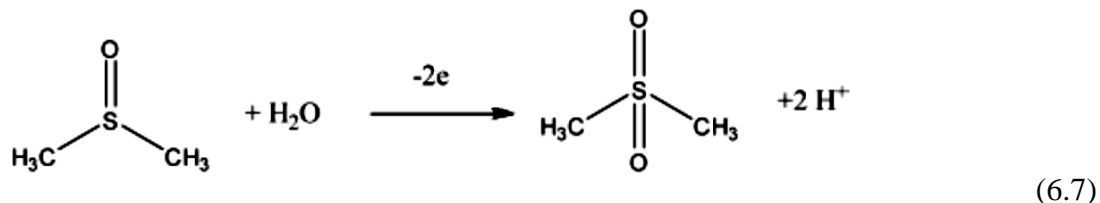
Figure 6.6. In situ IR spectra of a deoxygenated solution of 0.1 M TBAPF<sub>6</sub> in DMSO on Au.

The normalized integrated peak area of  $\text{SO}_2$  of dimethyl sulfone at  $1140\text{ cm}^{-1}$  versus applied potential is shown in Figure 6.7 for all three solutions. It can be seen that in all solutions decomposition of dimethyl sulfoxide to sulfone starts at around 4.2 V. We conclude that at the potentials where  $\text{O}_2^-$  is formed, no appreciable electrolyte decomposition occurs in any of the studied solutions. This is consistent with the results previously reported for DMSO decomposition by  $\text{O}_2^-$  with a very low bimolecular rate constant ( $\kappa \sim 2 \times 10^{-6}\text{ M}^{-1}\text{cm}^{-1}$ ). (181) Likewise, the solutions containing  $\text{Li}^+$  or  $\text{TBA}^+$  are stable in the presence of  $\text{O}_2^-$ . At potentials higher than 4.2 V, an anodic oxidation of DMSO is detected and the oxidation product can be easily determined as dimethyl sulfone. The same decomposition reaction was found to occur in both oxygenated and deoxygenated solutions. Therefore, we conclude that formation of dimethyl sulfone at high potentials is not a result of the presence of oxygen species in the solvent.



**Figure 6.7.  $\text{SO}_2$  peak ( $1140\text{ cm}^{-1}$ ) integrated area versus applied potential of solution of 0.1 M  $\text{LiPF}_6$  in DMSO,  $\text{O}_2$  saturated, 0.1 M  $\text{TBAPF}_6$  in DMSO, saturated in  $\text{O}_2$  and deoxygenated, on a Au working electrode.**

At the same potential where  $\text{DMSO}_2$  is formed, depletion of traces of water has been detected, which indicates that DMSO oxidizes to  $\text{DMSO}_2$  by reacting with traces of water. The suggested reaction is:



**In Situ IR Spectroscopy Results on Pt.** Cyclic voltammetry in O<sub>2</sub> saturated 0.1 LiPF<sub>6</sub> DMSO solution on Au and Pt working electrodes are shown in Figure 6.8. An increase of the oxidation current is observed on the Pt electrode starting around 3.5 V; therefore, Pt catalyzes the parasitic reaction occurring during the oxidation (charging) reaction.

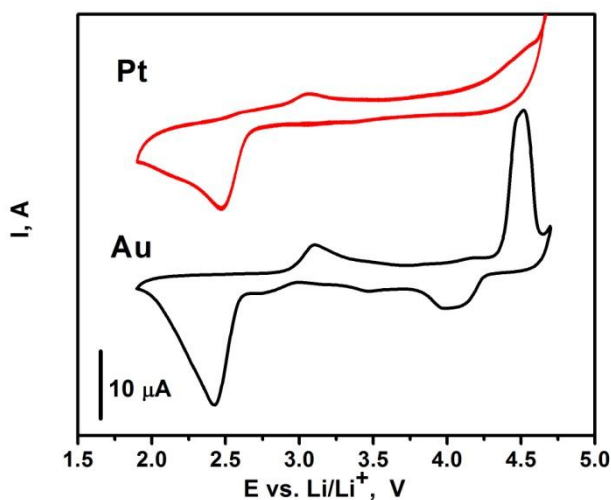
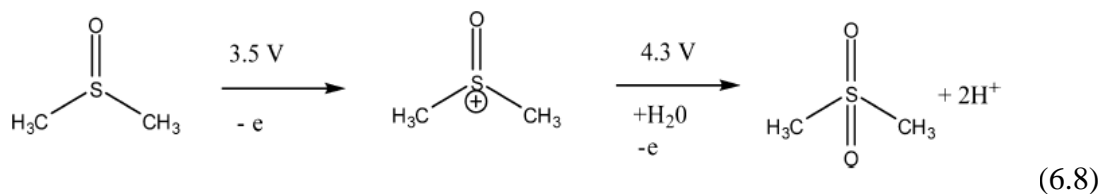


**Figure 6.8. CV scans in a solution of O<sub>2</sub> saturated 0.1 M LiPF<sub>6</sub> in DMSO, on Pt and Au.**

In situ IR spectra have been recorded on the Pt electrode at potentials between 3.1 and 4.7 V (figure 6.9). At 3.5 V, a peak at 1050 cm<sup>-1</sup> (S=O stretching) appears and increases in intensity with increasing potential; at 4.3 V, this peak starts to decrease, which coincides with the appearance of the 1150 cm<sup>-1</sup> mode characteristic of sulfone (similar to the evidence on the Au electrode). Unlike what occurred on Au, it is suggested that an intermediary of DMSO decomposition is formed on Pt which is subsequently oxidized above 4.3 V to form dimethyl sulfone, as shown by the 1150 cm<sup>-1</sup> mode. We speculate with the following mechanism:



This result implies that Pt catalyzes DMSO decomposition at lower potentials than Au, that is, from 3.5 V. Therefore platinum would not be a suitable catalyst to recharge a cell above .5 V for the DMSO-based Li-air cells.

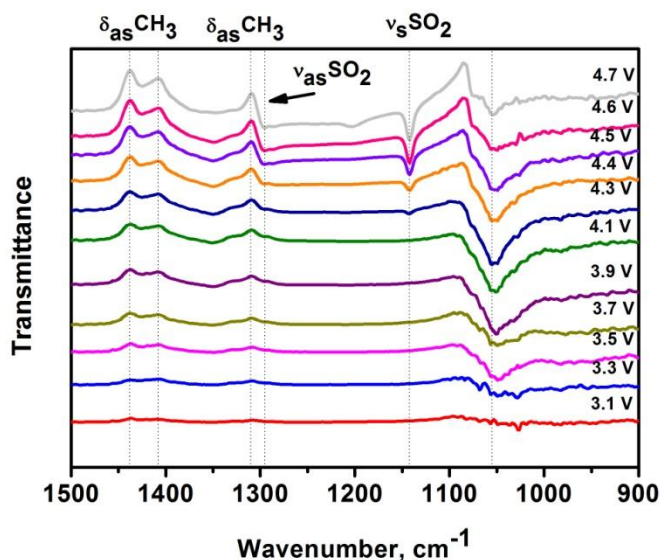


**Figure 6.9.** In situ IR spectra of a deoxygenated solution of 0.1 M LiPF<sub>6</sub> in DMSO, on Pt.

**Understanding carbon dioxide evolution.** Here we report a new insight on the decomposition of DMSO-based solvent for Li-O<sub>2</sub> system evidenced by in-situ analytical tools (SNIFTIRS, EQCM, DEMS and XPS) coupled to the electrochemical cell. We have also used the TBA<sup>+</sup> cation along with Li<sup>+</sup> in order to distinguish separately the effects on solvent decomposition from different reactive species and reaction components: O<sub>2</sub>, O<sub>2</sub><sup>-</sup>, Li<sup>+</sup>, Li<sub>2</sub>O<sub>2</sub>, etc.

For the in situ SNIFTIRS experiment, a set of fixed potentials was chosen according to CV in DMSO and was applied to the cathode. The IR spectra were collected at each potential applied in order to evaluate changes produced on the electrode surface. Potentials were chosen in order to follow the cyclic voltammetry and to observe ORR first and then OER.

The resulting spectra for the solutions of  $\text{LiPF}_6$  and  $\text{TBAPF}_6$  in oxygenated DMSO are shown in the figure 6.10. Notably, from an oxidizing potential of 4.2 V and above a downward peak is detected at  $2340\text{ cm}^{-1}$  and corresponds to antisymmetric stretching of  $\text{CO}_2$  at the vicinity of the electrode surface. The  $\text{CO}_2$  evolution has been detected in the oxygenated solutions of DMSO at high potentials, either with or without  $\text{Li}^+$ . However, practically no  $\text{CO}_2$  evolution from the deoxygenated DMSO has been detected (data not shown). This is an evidence of an important role of molecular oxygen for the solvent decomposition consistent with the DEMS results demonstrating oxygen depletion during  $\text{CO}_2$  evolution and gold porous electrode (187).

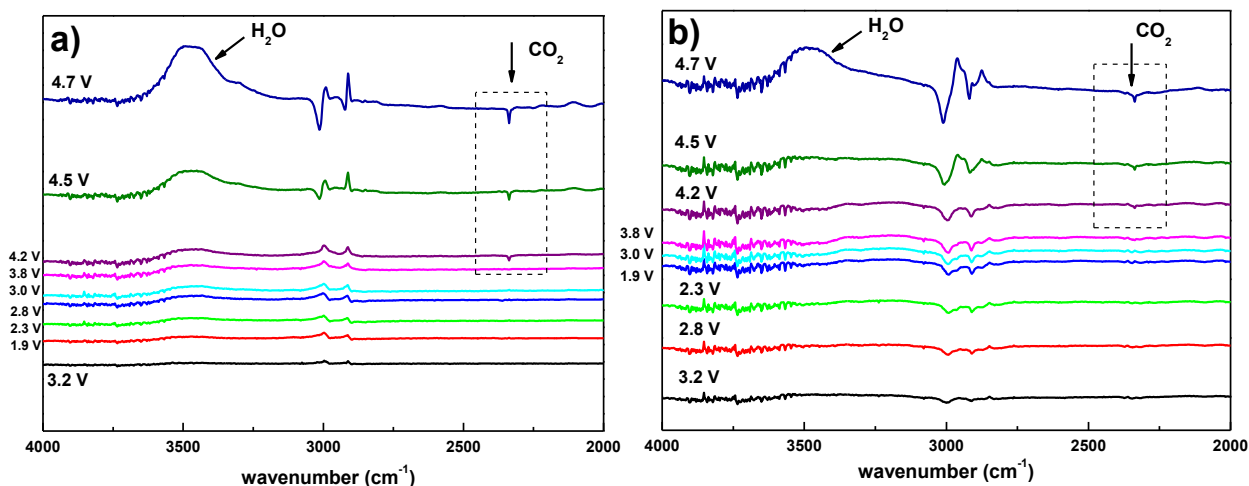


**Fig 6.10. In situ IR spectra of solutions a) 0.1 M  $\text{LiPF}_6$ , DMSO,  $\text{O}_2$  saturated and b) 0.1 M  $\text{TBAPF}_6$ , DMSO,  $\text{O}_2$  saturated.**

The normalized integrated peak area of carbon dioxide peak at  $2340\text{ cm}^{-1}$  versus applied potential is shown in Figure 6.11 for the oxygenated DMSO solutions with and without  $\text{Li}^+$ . It can be seen that in both solutions  $\text{CO}_2$  evolution starts at around 4.2 V and it is notable that the  $\text{CO}_2$  evolution pattern is almost identical in the solution containing  $\text{Li}^+$  and  $\text{TBA}^+$ .

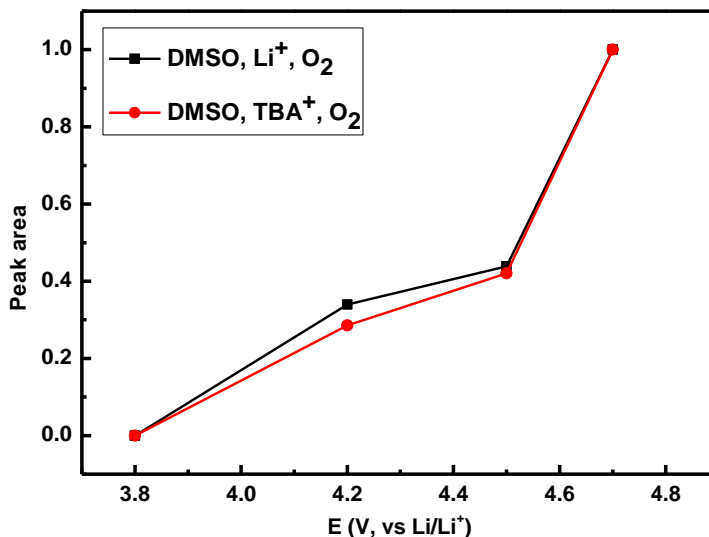


**Figure 6.10. CO<sub>2</sub> peak integrated area versus applied potential of solution of 0.1 M LiPF<sub>6</sub> in DMSO 0.1 M TBAPF<sub>6</sub> in DMSO, saturated in O<sub>2</sub> on a Au working electrode.**

In the potentiostatic experiments coupled to the quartz crystal microbalance and mass spectroscopy, three different potentials: 1.9 V, 3.1 and 4.5 V, were applied for two minutes to the gold working electrode and the responses of EQCM and DEMS were measured accordingly. The results are depicted simultaneously on the figure 6.11.

When 1.90 V was applied to the cell, the EQCM showed a mass increase up to 5.5  $\mu\text{g}$ , and at the same time DEMS signal for ionic current  $m/q = 32$  (O<sub>2</sub>) decreased. When the potential of cell was switched to 3.1 V, the mass in EQCM remained unaffected, but O<sub>2</sub> signal showed a peak, that decreased gradually with time. Finally, when the cell potential was set to 4.5 V, the mass measured by EQCM decayed completely until reaching the initial experimental value. At the same time the signal of CO<sub>2</sub> in DEMS increased considerably, while the O<sub>2</sub> signal remained constant. To conclude, during the potential of 1.9 V, we evidenced a mass increase simultaneous to the oxygen consumption that corresponds the ORR. At 3.1 V the oxygen was evolved, while the mass remained the same, thus we suggest that only soluble species (superoxide anion) are oxidized at this potential. At 4.5 V we saw disappearance of mass in EQCM, however only CO<sub>2</sub> was evolved at this potential and no O<sub>2</sub> evolution occurred, suggesting that other than lithium peroxide species are oxidized at this potential.

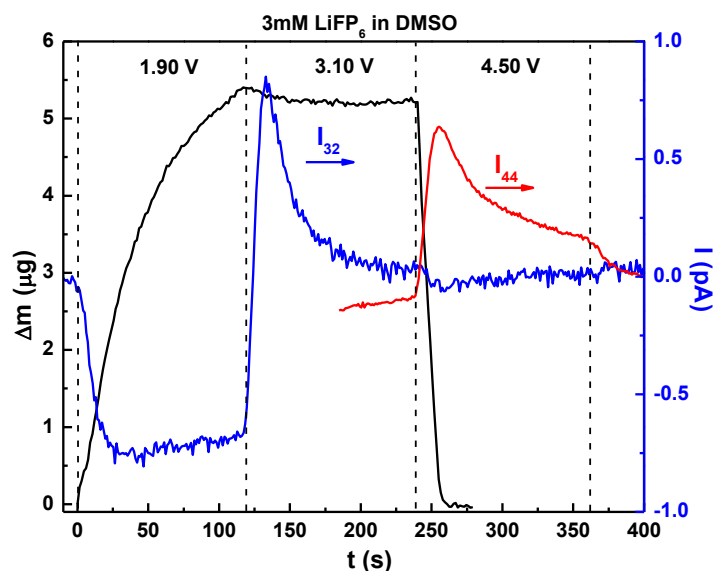


**Figure 6.11. EQCM and DEMS recorded simultaneously on gold electrode during three potential transients to 1.9, 3.1 and 4.5 V in 3 mM LiPF<sub>6</sub> DMSO. Experiment was performed by W. Torres and A. Tesio, graph taken from reference (188)**

To identify the nature of the deposit detected by EQCM, we have also performed XPS measurements on a clean gold electrode and after polarization at the selected potentials of 2.05 V, 3.35 V and 4.50 V, which correspond to ORR potential, the thermodynamic redox potential of Li/Li<sub>2</sub>O<sub>2</sub> couple and OER potential respectively. The XPS signals of the C 1s region are presented in the figure 6.12. Whereas no carbon was initially present on the surface of the electrode, two broad peaks centered at 285.4 eV and 290.5 eV appeared after performing the ORR at 2.05V. The peak at 285.4 eV is a complex signal which can be attributed to a number of R-O species, while the signal at 290.5 eV is typical from carbonate anion.

As for the attempts to restore the surface through anodic polarizations, electrochemical oxidation at 4.50 eV only succeeded to remove lithium carbonate, whereas the other carbon species remained on the surface. Those results are in agreement with SNIFTIRS and DEMS results that detect CO<sub>2</sub> formation at the same potential.

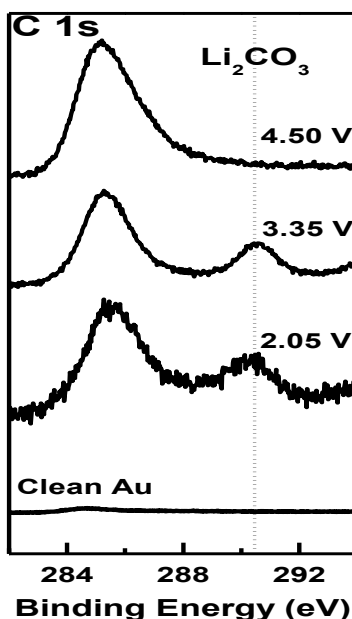


**Figure 6.12.** C1s region of XPS spectra performed on a clean gold electrode and after polarization at 2.05 V, 3.35 V and 4.40 V in a DMSO/LiPF<sub>6</sub> O<sub>2</sub> saturated electrolyte.

Experiment was performed by F. Marchini, graph taken from reference (188)

As the only carbon containing compound of the system was the solvent, these results support the idea that DMSO undergoes further chemical decomposition after reacting with ORR products and no full recharge is possible owing to the remaining species on the surface of the electrode even after highly oxidizing polarization. The observed spectroscopic S2p, Li1s and O1s regions strongly complements this hypothesis(187). The finding is in agreement with work published by Younesi et.al.,(189) who reported the decomposition of DMSO in direct contact with Li<sub>2</sub>O<sub>2</sub> powder by XPS.

While the exact mechanism for the degradation of the solvent DMSO has not been completely unraveled, at this point in time we have clear evidence of carbonate and other oxygenated carbonaceous mater formation on the surface during ORR and direct electrochemical oxidation to dimethyl sulphone at high overpotential. Furthermore both IR and DEMS have revealed two sources of CO<sub>2</sub>, from carbonate decomposition and from solvent oxidation at high overvoltage. Also XPS has shown formation of sulfur species on the surface(187).

### 6.3. In Situ Infrared Spectroscopy Study of PYR<sub>14</sub>TFSI Ionic Liquid Stability for Li–O<sub>2</sub> Battery

While the majority of research effort has focused on organic solvents (initially alkyl carbonates, and later ethers, acetonitrile and dimethyl sulfoxide), there has been also some interest in the use of ionic liquids as electrolyte for the Li-oxygen system.

Herranz et al. have used the Rotating Ring Disc Electrode (RRDE) experiments to quantify the stability of PYR<sub>14</sub>TFSI in the presence of superoxide anion and estimated the rate constant of the reaction to be three orders of magnitudes less than that for propylene carbonate (PC) (140). Fritz and co-workers used in-situ Raman spectroscopy to detect the products of oxygen reduction in 1-ethyl-3-methylimidazolium bis(trifluoromethylsulfonyl)imide C<sub>2</sub>mimTFSI and PYR<sub>14</sub>TFSI(142). They reported that C<sub>2</sub>mimTFSI degrades during the reduction of oxygen, while PYR<sub>14</sub>TFSI was found to be resistant to degradation in 10 mM LiTFSI being superoxide the first reaction product and Li<sub>2</sub>O<sub>2</sub> further formed.

Up to date there are a handful of publications that report testing of some ionic liquids, mostly PYR<sub>14</sub>TFSI in Li-air charge-discharge experiments. In 2005 Kuboki et al. reported a Li-air battery using ionic liquid electrolyte, however only the first discharge cycle was reported without recharging cycle (190). In 2014 Elia et al. reported an advanced Li-air battery based of PYR<sub>14</sub>TFSI-LiTFSI electrolyte; they claimed the battery to have a stable electrode-electrolyte interface, highly reversible charge–discharge cycling behavior and low charge overpotential (106). On the other hand, Piana et al. have investigated three different setups for a Li-O<sub>2</sub> battery with PYR<sub>14</sub>TFSI based electrolyte: one-compartment Li-O<sub>2</sub> cell with Li metal as anode, two-compartment cell with propylene carbonate (PC) as anode electrolyte with Li-ion conducting solid separator, and one-compartment cell with lithiated Li<sub>4</sub>Ti<sub>5</sub>O<sub>12</sub> (LTO) as anode. For the first configuration it was found that pyrrolidinium ion is reduced on lithium metal, producing substantial amounts of alkenes and amines. The cell with lithiated LTO did solve the problem observed with lithium metal, however it showed poor cycleability, therefore the authors suggested that PYR<sub>14</sub>TFSI might not have enough long-term stability against ORR products(105).

In this chapter, in situ infrared spectroscopy experiments were performed simultaneously with electrochemical experiments and complemented by differential electrochemical mass spectrometry (DEMS), to investigate the  $\text{PYR}_{14}\text{TFSI}$ -based electrolyte stability under conditions relevant to the Li–air cell operation. While DEMS detects electrolyte decomposition products in the gas phase, in-situ SNIFTIRS allows detection of the decomposition products in the solvent phase, adjacent to the electrode surface.

Cyclic voltammetry of oxygen saturated ionic liquid  $\text{PYR}_{14}\text{TFSI}$  containing 25 mM  $\text{LiTFSI}$  is depicted on the figure 6.13. Two reduction peaks are observed at 2.15 and 1.9 V, that could be assigned to oxygen reduction to superoxide involving  $\text{Li}^+$  and  $\text{PYR}_{14}^+$  respectively. On the reverse scan, the first oxidation peak corresponds to the oxygen evolution from superoxide stabilized by ionic liquid cation ( $\text{PYR}_{14}^+ \text{O}_2^-$ ), while oxidation of lithium peroxide formed by  $\text{LiO}_2$  disproportionation is observed at much higher potentials above 3.5 V, in agreement with previous studies(98, 139).

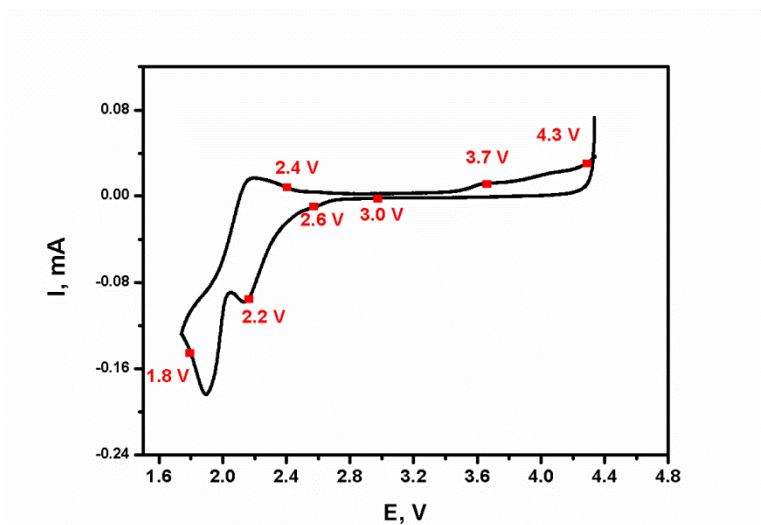


**Figure 6.13. Cyclic voltammetry of  $0.2 \text{ cm}^2$  Au electrode in 25 mM  $\text{LiTFSI}$  in  $\text{O}_2$  saturated  $\text{PYR}_{14}\text{TFSI}$ , scan rate 50 mV/s.**

Results of differential electrochemical mass spectrometry (DEMS) performed simultaneous to the ORR (1.8 V) and OER (2.4-4.5 V) in pure ionic liquid and 25 mM  $\text{LiTFSI}$  in  $\text{PYR}_{14}\text{TFSI}$  are shown in Figure 6.14.

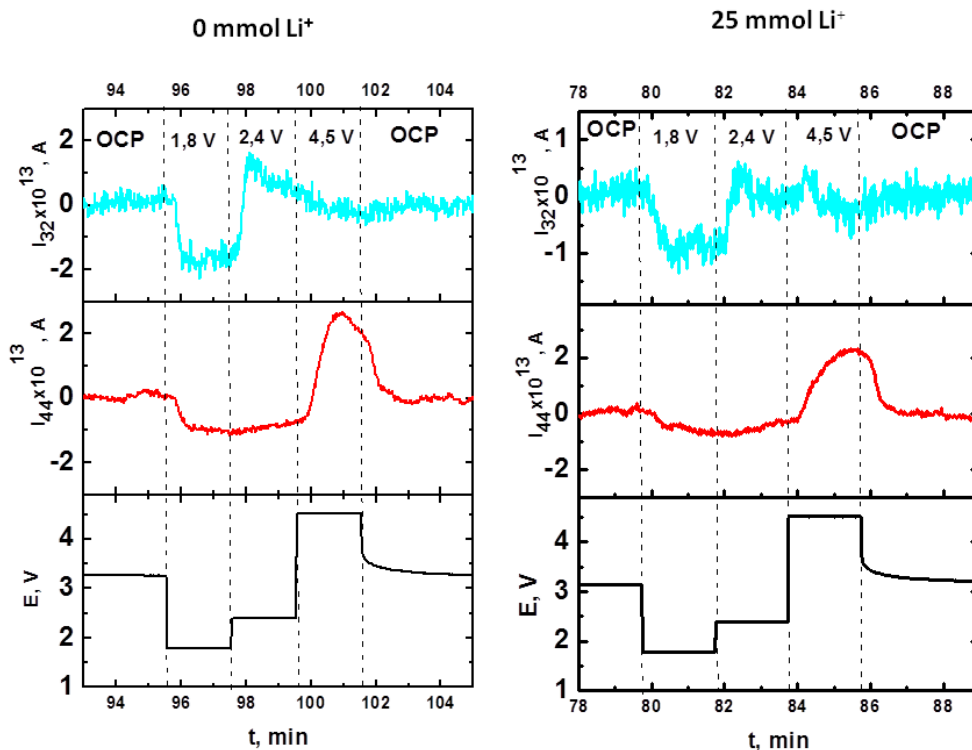


**Figure 6.14. DEMS ionic currents for mass 32 and 44 respectively in O<sub>2</sub> saturated solution of 25 mM LiTFSI in PYR<sub>14</sub>TFSI at different potentials: OCP, 1.8, 2.4, 4.5 V and OCP.**

In both systems oxygen consumption is observed at 1.8 V. However oxygen evolution for pure ionic liquid occurs at 2.4 V, while for the 25 mM Li<sup>+</sup> salt in the ionic liquid, oxygen evolution takes place at two distinct potentials: 2.4 and 4.5 V respectively. Those results are in agreement with a previous research and confirm oxygen evolution from the superoxide in the case of pure ionic liquid, and oxygen evolution partly from superoxide and lithium peroxide in the case of Li<sup>+</sup> salt containing ionic liquid. Ionic currents for mass 44 at potential of 4.5 V demonstrate the formation of carbon dioxide by decomposition of the ionic liquid in both electrolytes.

The IR spectrum of the ionic liquid under study exhibits several peaks in the 4000-900 cm<sup>-1</sup> interval. The spectrum and molecular structure of pure PYR<sub>14</sub>TFSI is shown in Figure 6.15 and the assignment of the peaks is summarized in table 6.1. Both the spectrum and assignments are in perfect agreement with previously reported IR data for similar systems(191-193)

**Table 6.1. Peak assignments for the ionic liquid PYR<sub>14</sub>TFSI**

Wavenumber, cm <sup>-1</sup>	Assignment	
2970	CH <sub>3</sub> antisymmetric C-H stretching ( $\nu_{\text{as}}\text{CH}_3$ )(194)	cation
2943	CH <sub>2</sub> antisymmetric stretching( $\nu_{\text{as}}\text{CH}_2$ )(194)	cation
2882	CH <sub>3</sub> symmetric C-H stretching ( $\nu_{\text{s}}\text{CH}_3$ )(194)	cation
1467	CH <sub>2</sub> scissoring bending ( $\delta_{\text{s}}\text{CH}_2$ )(194)	cation
1433	CH <sub>3</sub> antisymmetric bending ( $\delta_{\text{as}}\text{CH}_3$ )(194)	cation
1353	SO <sub>2</sub> antisymmetric stretching ( $\nu_{\text{as}}\text{SO}_2$ )(194)	anion
1195 broad peak 1225 shoulder	CF <sub>3</sub> antisymmetric stretching ( $\nu_{\text{as}}\text{CF}_3$ )(194, 195)	anion
1138	SO <sub>2</sub> symmetric stretching ( $\nu_{\text{s}}\text{SO}_2$ )(194)	anion
1056	SNS asymmetric stretching ( $\nu_{\text{as}}\text{SNS}$ )(195)	anion

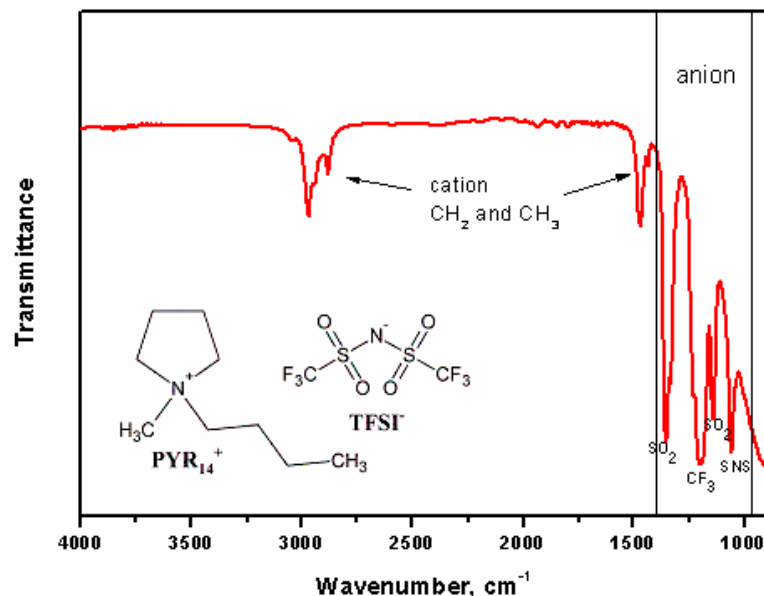


**Figure 6.15.** IR Spectrum and structure of PYR<sub>14</sub>TFSI ionic liquid.

In order to evaluate the stability of the ionic liquids under conditions relevant to the Li-air battery operation, a set of fixed potentials has been applied to the Au cathode and the IR spectra have been collected at each potential. The potentials applied were chosen as indicated in the cyclic voltammetry of oxygen saturated 25 mM LiTFSI in PYR<sub>14</sub>TFSI solution depicted in Figure 6.13, as well as previously reported data on charge-discharge experiments in similar systems.

We first analyzed the system at near open circuit potential (about 3.0 V), then during ORR (2.2 V), back near open circuit potential (3.0 V), during OER (3.7, 4.3 and 4.9 V respectively), and then back to reducing potential of 2.2 V.

In the SNIFTIR spectra, negative peaks (downward) correspond to the compounds that are formed, while positive peaks (upward) correspond to the modes that disappear.

The spectra obtained in the oxygen saturated 25 mM LiTFSI solution in PYR<sub>14</sub>TFSI are shown on the Figure 6.16. Almost in all spectra positive peaks at 2970, 2943, 2882, 1467 and 1433 cm<sup>-1</sup> are detected with higher intensity at 3.7, 4.3 and 4.9 V. Those are attributed to CH<sub>2</sub> and CH<sub>3</sub> groups of ionic liquid cation PYR<sub>14</sub><sup>+</sup>, thus suggesting slow decomposition of ionic liquid cation during ORR and more pronounced decomposition during the OER at higher oxidizing potentials.

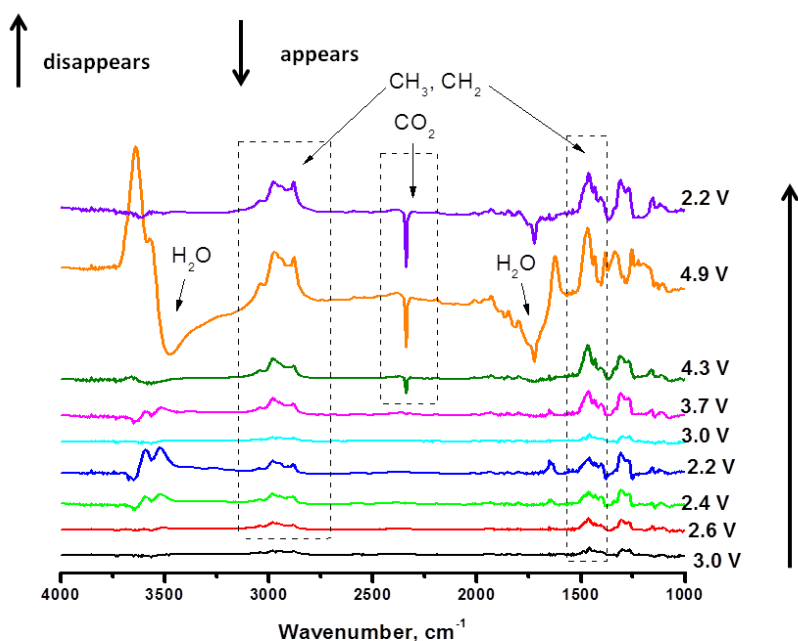


**Figure 6.16. In situ IR spectra taken in O<sub>2</sub> saturated 25 mM LiTFSI in PYR<sub>14</sub>TFSI solution on Au working electrode.**

Notably, at the high oxidizing potential of 4.3 and 4.9 V a downward peak is detected at 2340 cm<sup>-1</sup> that corresponds to the formation of CO<sub>2</sub> at the electrode surface(196). Those results are consistent with data obtained from DEMS, showing CO<sub>2</sub> evolution at 4.5 V. An important result is that by switching back to 2.2 V, the peak intensity seems unchanged. Thus we suggest that the CO<sub>2</sub> is formed during the recharge starting at 4.3 V which cannot be reduced neither undergoes reaction with lithium peroxide deposit during the following discharge.

Also at 4.9 V two broad negative peaks appear approximately at 3470 and 1720 cm<sup>-1</sup>. They may be assigned to the formation of water at the interface (the shift of one of the peaks to more positive wave numbers could be explained in terms of water environment and high positive potential). Interestingly, in the following discharge (step to 2.2 V), those two peaks disappear.

We can conclude that during the recharge, the ionic liquid cation undergoes decomposition forming carbon dioxide and water, and water formed during ionic liquid decomposition, is consumed during the following battery discharge, probably reacting with lithium peroxide to form lithium hydroxide and hydrogen peroxide.



To discover, whether the presence of lithium superoxide or peroxide promoted the decomposition of the  $\text{PYR}_{14}^+$  cation, we have repeated the experiment, but avoiding the ORR excursion (2.6, 2.4 and 2.2 V). The resulting spectra are plotted in Figure 6.17 and differ very slightly from those reported previously.

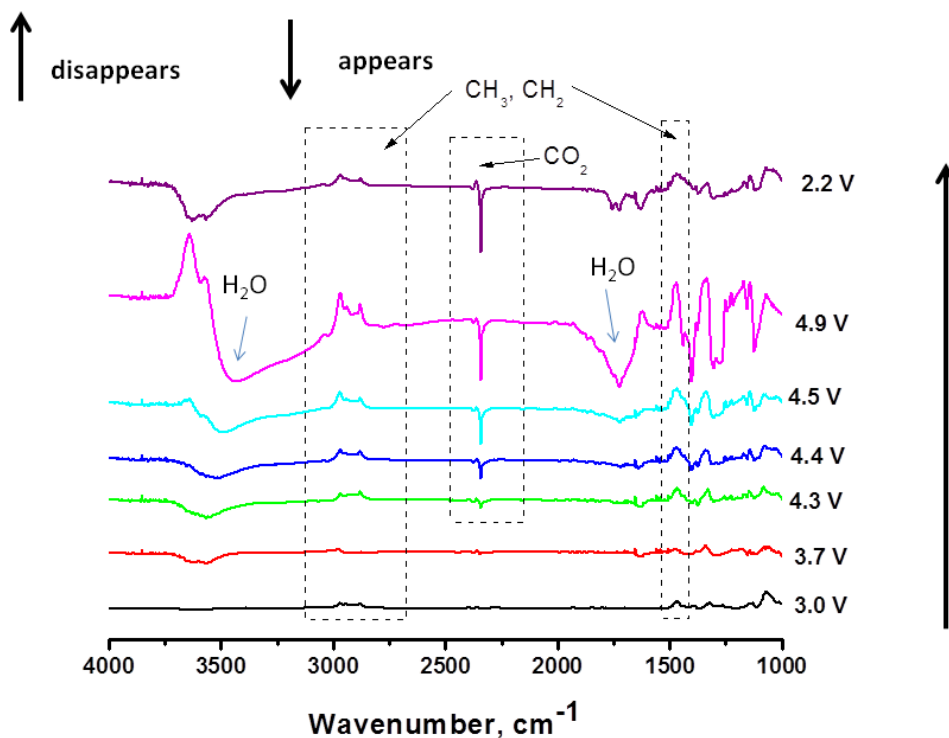


**Figure 6.17** In situ IR spectra taken in  $\text{O}_2$  saturated 25 mM LiTFSI solution in  $\text{PYR}_{14}\text{TFSI}$  on Au working electrode, at potentials above 3.0 V.

From 4.3 V, a negative peak at  $2340\text{ cm}^{-1}$  is observed which corresponds to carbon dioxide formation. At 4.5 V broad negative peaks at  $3470$  and  $1720\text{ cm}^{-1}$  indicate formation of water. Therefore, we can conclude that with or without ORR, the ionic liquid decomposition proceeds in a similar way.

To fully elucidate the mechanism for  $\text{PYR}_{14}^+$  decomposition and  $\text{CO}_2$  formation, analogous experiments were performed on the deoxygenated  $\text{PYR}_{14}\text{TFSI}$  in the presence of  $\text{Li}^+$  ion (figure 5.18) and in the pure deoxygenated ionic liquid without  $\text{Li}^+$  (figure 6.19).

Figure 6.18 shows positive peaks at 2970, 2943, 2882, 1467 and 1433  $\text{cm}^{-1}$  independently of the applied potential. These features are to be attributed to the ionic liquid  $\text{PYR}_{14}^+$  cation decomposition as described previously and this decomposition process in the presence of  $\text{Li}^+$  ion is independent of the applied potential.

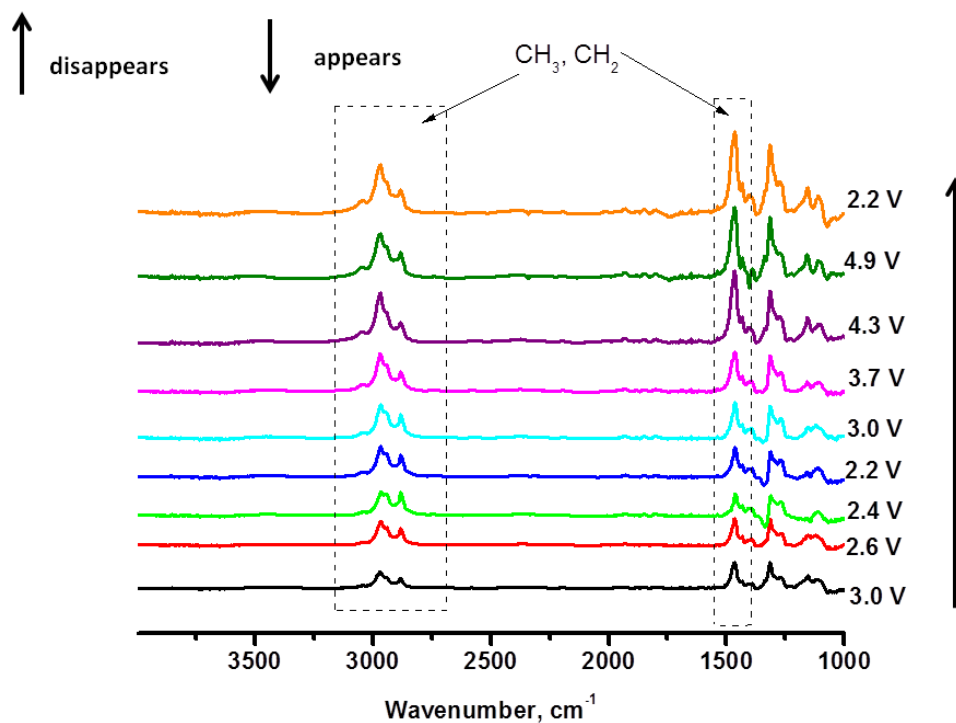


**Figure 6.18** In situ IR spectra taken in deoxygenated 25 mM LiTFSI solution in  $\text{PYR}_{14}\text{TFSI}$  on Au working electrode.

The results obtained from pure deoxygenated ionic liquid (Figure 6.19) do not show any peaks corresponding to  $\text{PYR}_{14}^+$  decomposition, thus corroborating our assumption that the Lewis acid  $\text{Li}^+$  alone is responsible for the slow ionic liquid decomposition. However, at potentials of 4.3 V and 4.4 V downward peaks at near 1400  $\text{cm}^{-1}$  and 1375  $\text{cm}^{-1}$ , respectively, appear. Those peaks

grow while increasing the applied potential, and decrease while switching back to 3.0 V with complete disappearance at 2.2 V. Considering the reversibility of this phenomena, we assume that those peaks represent changes in the electrical double layer due to the adsorption of the ionic liquid anion species, probably by SO<sub>2</sub> groups, at high positive potential(197).

Notably, in Figures 6.18 and 6.19 no peak appears at 2340 cm<sup>-1</sup> wave number, as well as no peaks are seen at 3470 and 1720 cm<sup>-1</sup>. Those results imply that no carbon dioxide, neither water were formed under those anaerobic conditions in the absence of lithium ions. It is fair to conclude that the presence of O<sub>2</sub> in the solution is necessary to produce in CO<sub>2</sub> and H<sub>2</sub>O.

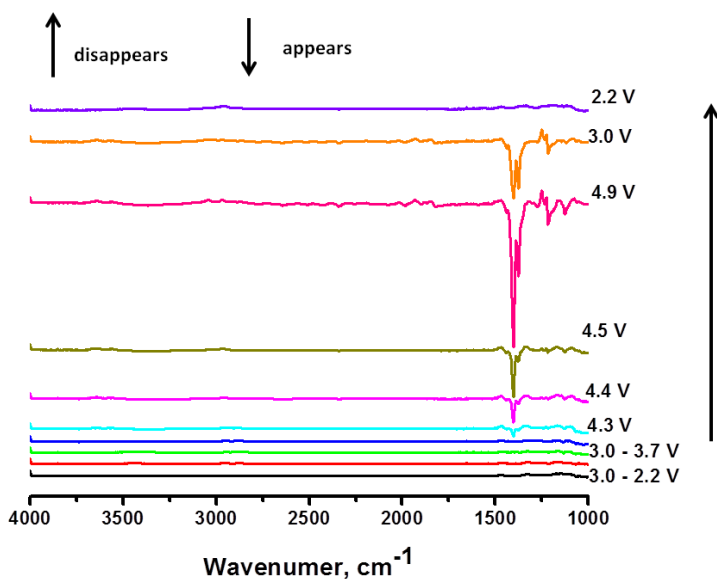


**Figure 6.19.** In situ IR spectra taken in O<sub>2</sub> free PYR<sub>14</sub>TFSI ionic liquid on Au working electrode.

## 6.4. Conclusions.

In this chapter the stability of two potential electrolyte systems: DMSO and the ionic liquid  $\text{PYR}_{14}\text{TFSI}$  has been evaluated under conditions relevant for the Li-air battery operation.

It has been found that in long time scales (two months period), dimethyl sulfoxide undergoes chemical decomposition to dimethyl sulfone in the presence of superoxide anion, but no appreciable decomposition occurs in the presence of insoluble lithium peroxide. In situ SNIFTIRS experiments, however, have shown that DMSO is stable during electrochemical reduction of oxygen, but it undergoes electrochemical oxidation to dimethyl sulfone at high potential during charging of the battery. We have detected formation of dimethyl sulfone starting at 4.2 V on the gold electrode in  $\text{O}_2$ -saturated and deoxygenated  $\text{LiPF}_6$  and  $\text{TBAPF}_6$  solutions in DMSO. The Li-air cell should not be charged above 4.2 V with Au cathodes because of anodic electrolyte decomposition.

Concurrent with the formation of dimethyl sulfone, we have detected consumption of trace water from the solvent; thus, we conclude that water molecules react with DMSO to form  $\text{DMSO}_2$  at high potentials. Therefore, water content in the electrolyte has to be carefully controlled.

Similar studies performed on Pt electrodes have shown electrolyte decomposition at a potential lower than that on Au electrodes. DMSO undergoes decomposition on Pt starting at 3.5 V with formation of an intermediate compound which then oxidizes further to dimethyl sulfone above 4.3 V.

We also have combined several analytical in situ tools in order to get a deeper insight into the decomposition of DMSO in conditions relevant to the Li-air battery operation. During the ORR we have evidenced the mass increase by EQCM simultaneous to the oxygen consumption evidenced by DEMS. However by XPS we have shown that this deposit was not only the desired  $\text{Li}_2\text{O}_2$  but also carbonates and a number of R-O species were formed. At a potential of 3.1 V we detected the oxygen evolution in the solutions of 3 mM of  $\text{Li}^+$  in DMSO, however the mass remained the same and the XPS has shown that carbonates and R-O species remained in the surface. However when applying a high oxidative potential of 4.5 V the mass decreases simultaneously to the disappearance of carbonates and the  $\text{CO}_2$  evolves as evidenced both by DEMS and SNIFTIRS. However interestingly enough, infrared spectroscopy studies have shown

the formation of CO<sub>2</sub> also in the absence of Li<sup>+</sup> ion, while the presence of oxygen was necessary to result in CO<sub>2</sub> evolution. All this evidence leads to suggest that lithium peroxide undergoes decomposition reaction with DMSO forming lithium carbonate that can only be oxidized at high potential of 4.5 V resulting in evolution of carbon dioxide; however other parasitic reaction of solvent with molecular oxygen also can occur resulting in CO<sub>2</sub> evolution.

As for the case of ionic liquid PYR<sub>14</sub>TFSI, In situ SNIFTIRS experiments have indicated relative stability of the ionic liquid anion, while the cation PYR<sub>14</sub><sup>+</sup> showed several possible decomposition reactions under the studied conditions.

We showed carbon dioxide and water formation starting at 4.3 V in oxygen saturated LiTFSI containing ionic liquid, which is in agreement with results obtained by DEMS, indicating carbon dioxide evolution at 4.5 V. Importantly, carbon dioxide and water were formed regardless of oxygen reduction reaction was occurring or not. Interestingly, oxygen free solutions have shown neither water nor carbon dioxide formation, suggesting that the presence of oxygen is crucial for those parasitic reactions to take place, which is very similar to the results obtained in DMSO.

The present results are of importance to estimate solvent's stability for its possible use in Li-air battery cathodes.

## 6.5. Resumen en castellano del capítulo 6. Estudios de la inestabilidad del solvente en la batería de Litio-aire.

Se ha demostrado que distintos electrolitos, incluyendo aquellos basados en carbonatos y éteres orgánicos, se descomponen luego de varios ciclos de carga-descarga. Varios trabajos han explorado las celdas de Li-aire con electrolitos basados en otros sistemas no acuosos, como dimetil sulfóxido (36, 49) y el líquido iónico  $\text{PYR}_{14}\text{TFSI}$  (105, 106). En este capítulo, hemos estudiado la estabilidad de dichos electrolitos en condiciones relevantes para el funcionamiento de la batería de litio-aire.

Se mostró que a largo plazo (2 meses), el dimetil sulfóxido se descompone químicamente a dimetil sulfona ( $\text{DMSO}_2$ ) en presencia del anión superóxido, pero no se detecta la descomposición del solvente en presencia de peróxido de litio (insoluble en DMSO).

Por otro lado, los experimentos de SNIFTIRS (Espectroscopía infrarroja por transformada de Fourier diferencial normalizada) in-situ han mostrado que el DMSO es estable durante la reducción electroquímica de oxígeno. Sin embargo el DMSO se oxida electroquímicamente a dimetil sulfona a potenciales altos durante la recarga de la batería. Se detectó la formación de  $\text{DMSO}_2$  a 4.2 V en un electrodo de oro en soluciones de  $\text{LiPF}_6$  y  $\text{TBAPF}_6$  en DMSO, saturados en oxígeno y también en solvente libre de oxígeno. Como conclusión, la batería de Litio-aire no debe ser cargada a potenciales mayores de 4.2 V con electrodos de oro debido a la descomposición anódica del electrolito. Simultáneamente a la formación de  $\text{DMSO}_2$ , se encontró la desaparición de trazas de agua del solvente. Así concluimos que las moléculas de agua reaccionan con el DMSO para formar  $\text{DMSO}_2$  a potenciales altos. Por lo tanto, el contenido del agua en el electrolito debe ser cuidadosamente controlado.

Estudios similares realizados en electrodos de Pt han mostrado la descomposición del electrolito a un potencial más bajo que en el electrodo de oro. El DMSO se descompone en estas condiciones a 3.5 V con la formación de un producto intermediario, que luego se oxida a dimetil sulfona a 4.3 V.

También hemos combinado varias técnicas analíticas in situ para estudiar en detalle el mecanismo de descomposición de DMSO en condiciones de funcionamiento de una batería de Litio-aire. Durante la reducción de oxígeno se evidenció el aumento de masa por EQCM

simultáneamente al consumo de oxígeno, detectado por DEMS. Sin embargo, con el uso de XPS se demostró que el depósito formado fue no solamente el esperado, peróxido de litio, sino también carbonatos y otras especies intermediarias de reacciones parásitas entre los productos de la reducción de oxígeno y el electrolito. A 3.1. V se detectó la evolución de oxígeno en soluciones de 3 mM de  $\text{Li}^+$  en DMSO, pero al mismo tiempo no se detectó el cambio de masa del depósito y el XPS mostró que los carbonatos y especies R-O formadas, pasivaron la superficie. Pero cuando se aplicó un potencial elevado de 4.5 V, la masa del depósito disminuyó en simultáneo con la desaparición de los carbonatos y la evolución del dióxido de carbono, evidenciado por DEMS y SNIFTIRS.

Cabe destacar que los estudios mediante espectroscopia infrarroja han mostrado la formación de  $\text{CO}_2$  incluso en ausencia de iones de  $\text{Li}^+$ , mientras que el  $\text{CO}_2$  sólo se forma cuando la solución se encuentra saturada en oxígeno.

Toda esta evidencia sugiere que el peróxido de litio participaría en la reacción de descomposición del DMSO formando carbonato de litio que puede ser oxidado únicamente a potenciales elevados tales como 4.5 V que resulta en la evolución de dióxido de carbono, pero también dan lugar a otras reacciones parásitas del solvente con el oxígeno molecular que también producen la evolución del  $\text{CO}_2$ .

Para investigar la estabilidad del electrolito basado en  $\text{PYR}_{14}\text{TFSI}$  en condiciones relevantes para la operación de la batería de litio-aire, hemos empleado espectroscopía infrarroja in situ acoplada a la celda electroquímica, complementando estos estudios con los de espectrometría de masas (DEMS). Se encontró que el anión de líquido iónico fue estable, mientras el cation se descomponía. En soluciones de  $\text{PYR}_{14}\text{TFSI}$  saturado en oxígeno y en presencia de  $\text{Li}^+$ , se observó la formación del dióxido de carbono y agua a partir de 4.3 V, mientras que en el sistema desoxigenado no se observó ni formación de  $\text{CO}_2$  ni  $\text{H}_2\text{O}$ , concluyendo que la presencia de oxígeno es crucial para la formación de dióxido de carbono.

Estos estudios son de gran importancia para estimar la estabilidad del solvente, para su posible aplicación en baterías de Litio-aire.

# Chapter 7. Conclusions and final remarks.

## 7.1. Thesis summary and conclusions.

Undoubtedly the Li-air battery has attracted an enormous interest in the scientific community during the last decade. This was of course generated by its extremely high theoretic energy density and its promise to replace the fossil fuels in the vehicles, which was further intensified by the advertising. As mentioned, the research into the Li-air battery was started with over-hyped expectations. However during the following few years, it became clear that a deeper understanding of the basic electrochemistry was necessary in order to progress in the area. This need of a deeper understanding of the fundamental chemistry coincided with the beginning of this doctoral thesis. In this thesis a deeper insight into the oxygen reduction and oxygen electroreduction reaction in the non-aqueous solvents has been gained. This investigation also took place while new ideas of the Li-oxygen electrochemistry in non aqueous electrolytes were deeply changing and new models were developed in the period 2012-2017. With the better understanding of the fundamental chemistry, the community has also appreciated realistically the challenges that have to be overcome in order to bring the Li-air technology to the market. However now, when the illusions about the Li-air battery are gone and the better understanding has been gained, we can judge more realistically and objectively its potential and the obstacles on the way of its realization.

In the chapter 3 we have discussed the need of the lithium metal anode protection/replacement and have explored the use of LTO/LLTO anode for the Li-air system studies. The Li-air cells built with LLTO anode and porous carbon cathode were found to have very low cycle retention which is in agreement with the most reported literature. The low cycle retention can be explained by the electrolyte and cathode instabilities and to the cathode occlusion by discharge species, therefore we justified the need to perform further deeper studies on the cathode-side reactions.

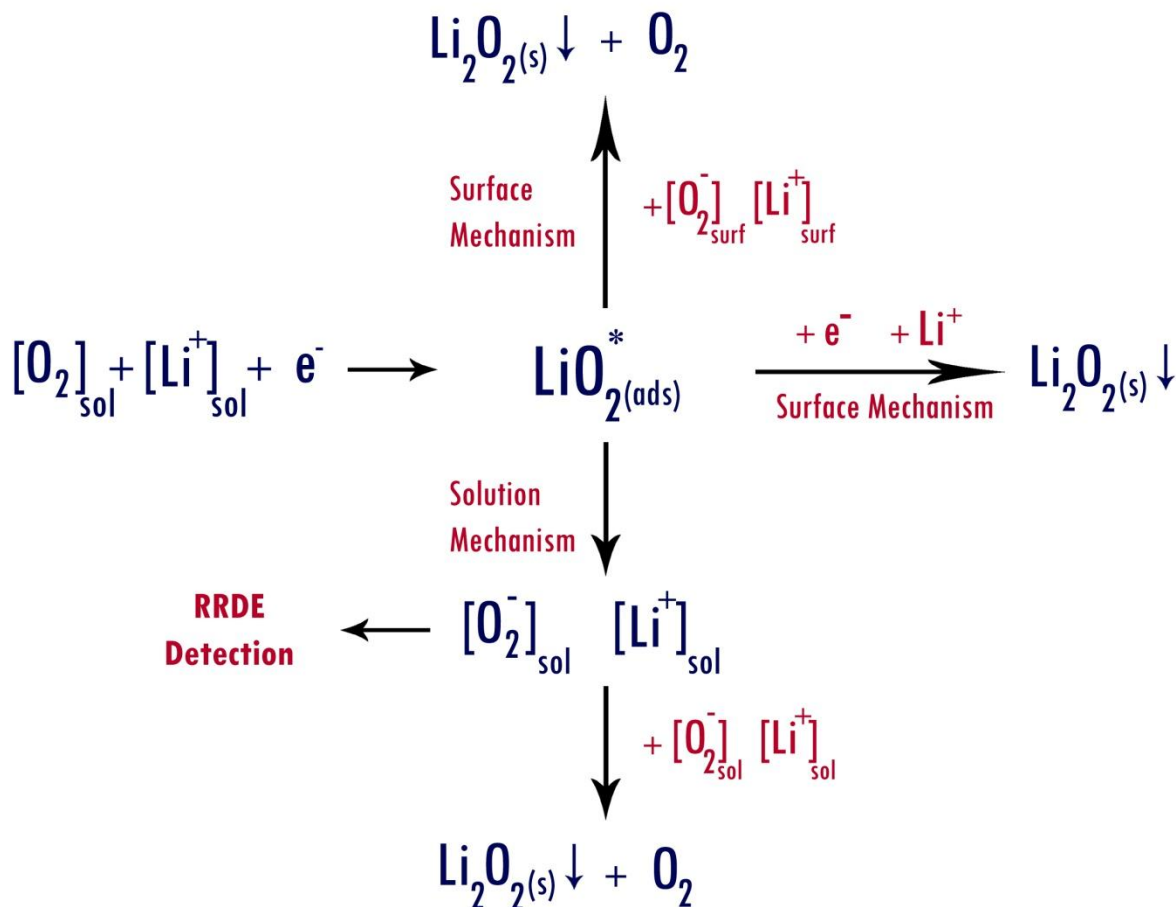
One of the important breakthroughs was the formulation of unified ORR mechanism based on the solubility and stability of lithium superoxide intermediate. This very important model was elaborated and formulated by our research group and almost simultaneously by several other research groups independently and is explained in the chapter 4 of the thesis. We have contributed to the understanding of this mechanism with the RRDE technique which allowed us

to distinguish between soluble and not soluble superoxide intermediate. The importance of this surface vs. solution mechanism cannot be overestimated because it allowed explaining previously very diverse results with the one unified model.

On the other hand, in chapter 5 of the thesis, we have explored the mixed electrolyte systems with the model system consisting of two solvents with opposite ORR mechanisms: via solution (DMSO) and via surface (ACN). This system showed very interesting properties such as preferential solvation of reactants: lithium ion  $\text{Li}^+$  and oxygen molecule  $\text{O}_2$ . The solvation of the reactants and intermediates is very important for the ORR and determines the shape and properties of the discharge products and therefore the cell capacity.

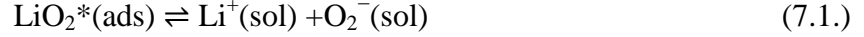
It is now clear that the solvent instability towards reduced oxygen species is one of the main reasons behind the Li-air battery fading performance. Up to now, the “perfect” solvent, that would be stable at both anode and cathode side and posses satisfactory  $\text{Li}^+$  and oxygen transport properties and low volatility, was not found, however it is important to compromise and use some solvents that were found to be relatively stable. In the chapter 6 we have employed various in-situ spectroelectrochemical techniques, mainly in-situ SNIFTIRS in order to characterize some promising systems, namely organic solvent DMSO and ionic liquid  $\text{PYR}_{14}\text{TFSI}$ : With these techniques we could unravel the parasitic reactions occurring in both electrolytes and those studies are not only useful as for the Li-air battery, but could be of interest for the other systems as well, Li-ion for example.

The new experimental evidence produced in the Thesis work can be summarized in the following scheme 7.1.



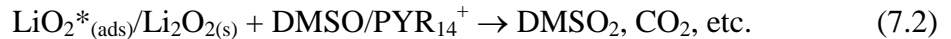
**Scheme 7.1. Schematics of the mechanism of ORR in aprotic solvents in presence of  $\text{Li}^+$ : solution vs. surface.**

1. The one electron reduction of molecular  $\text{O}_2$  in lithium containing electrolyte results in the adsorbed  $\text{LiO}_2^*$ , which has been characterized on porous Au electrodes by Peng et. al. by the Raman shift at  $1110 \text{ cm}^{-1}$  (36, 160).  $\text{LiO}_2$  and  $\text{Li}_2\text{O}_2$  have been detected on the surface of  $\text{O}_2$  cathodes by Raman spectroscopy. The Raman shifts for  $\text{O}_2^-$  and  $\text{LiO}_2$  are  $1110 \text{ cm}^{-1}$  and  $1132 \text{ cm}^{-1}$ , respectively, while the Raman shift for and  $\text{Li}_2\text{O}_2$  is  $\sim 800 \text{ cm}^{-1}$ .
2. The interaction of acetonitrile, DMSO and  $\text{PYR}_{14}\text{TFSI}$  with  $\text{Li}^+$  ions is very different as shown by the  $\text{Li}/\text{Li}^+$  electrode potential dependence on the composition of mixed solutions ACN-DMSO, and DMSO- $\text{PYR}_{14}\text{TFSI}$  and also by the conductivity data.
3. Stabilization of the  $\text{Li}^+$  by solvent or ionic liquid results in the detection of soluble superoxide ion with the RRDE. Therefore, the reaction:



becomes important when lithium ions and superoxide are well solvated or electrostatically stabilized by the ionic liquid ions.

4. The electrochemical quartz crystal microbalance (EQCM) has shown the formation of solid intermediate reaction products beyond  $\text{Li}_2\text{O}_2$  that can only be removed by high overpotential which in turn is detrimental for the solvent or ionic liquid cation stability.
5. The desorption of stable  $(\text{Li}^+)_{\text{SOL}}(\text{O}_2^-)_{\text{SOL}}$  ion pairs brings about a possible solution phase mechanism competing with the surface mechanism.
6. The formation of highly reactive  $\text{LiO}_2$  and  $\text{Li}_2\text{O}_2$  species on the surface may decompose the DMSO solvent and the cation  $\text{PYR}^+$  of the ionic liquid as shown by infrared spectroscopy, DEMS mass 44  $\text{CO}_2$  signal, EQCM and XPS, that can be summarized by the following scheme:



To summarize, while Li-air seems to be an extremely attractive technology, much more dedicated research effort is necessary for its possible commercialization. But on the other hand, the scientific community had a great benefit from studying the Li-air battery, with many sophisticated experimental set-ups, simulation models and theoretical explanations produced in order to study this complex three-phase systems.

Lithium air battery technology enabled a revival of fundamental electrochemistry and materials chemistry which is the real challenge of the sustainable energy storage future.

## 7.2. Future work

Over the last decade, we have gained a quite deep understanding of the fundamental chemistry occurring in the Li-air cells. It is still unclear whether or not the Li-air battery will become a commercial reality, however now, based on the gained knowledge it is possible to highlight the important future work directions:

**1. Distinguish between anode and cathode side parasitic chemistry.** Most of the experiments performed in the field deal with complete Li-air battery cell containing both lithium metal anode and porous carbon cathode. For the sake of fundamental understanding of the battery's parasitic chemistry it is important to study the cell's components separately.

**2. Keep searching for the solvent with desired performance.** With the gained knowledge about the reasons underlying decomposition reactions and a deeper insight into the ORR and OER reactions, we have now a clearer criterion in order to search for the electrolyte with the most favorable performance. The new evidence also shows the importance of the singlet oxygen in decomposition reactions. This aspect was not taken into the account in this thesis because of its novelty; however it is imperative to take it into account for shaping the future research directions.

**3. Redox mediators.** The stable and efficient redox mediators are necessary in order to lower the recharge potential and improve the cell reversibility.

**4. Lithium metal protection or substitution.** The Li-air battery possesses such a high theoretic energy density partly because of the use of lithium metal as anode material, however up to date the employment of lithium metal as anode material has proved to be problematic, therefore its protection is of paramount importance, and even the idea of its substitution should not be neglected.

**5. Cathode architecture.** While, the cathode clogging with insoluble and insulating lithium peroxide prevent the recharge of Li-air battery, the advance cathode architecture for an efficient en encounter for lithium ions, oxygen molecules and electrons is very important.

### 7.3. Conclusiones de la tesis en castellano.

Sin dudas, la batería de Li-aire ha atraído el interés de la comunidad científica durante la última década. Eso se ha debido a su extremadamente alta densidad de energía teórica y su promesa de reemplazar los combustibles fósiles en los vehículos, que se intensificó aún más por la publicidad. Como se mencionó, la investigación sobre la batería de Li-aire comenzó con expectativas exageradas. Sin embargo, durante los siguientes años, se hizo evidente que era necesaria una comprensión más profunda de los mecanismos electroquímicos y químicos básicos para progresar en el área. Esta necesidad de una comprensión más profunda de la química fundamental coincidió con el comienzo de esta tesis doctoral. En esta tesis se obtuvo una visión más profunda de las reacciones de electrorreducción y evolución de oxígeno en solventes no acuosos, mientras que el conocimiento en el campo se desarrollaba y evolucionaba rápidamente. Con una mejor comprensión de estos procesos fisicoquímicos, la comunidad científica también ha apreciado de una manera más real los desafíos que deben superarse para llevar adelante la tecnología de Li-aire al mercado. Sin embargo, ahora, cuando las ilusiones sobre la batería de Li-aire se han ido y se ha adquirido la mejor comprensión de procesos químicos que ocurren en dicha batería, podemos juzgar de manera más realista y objetiva el potencial y los obstáculos en el camino de su realización.

El trabajo de Tesis Doctoral realizado constituye un aporte original en un campo de enorme interés científico y tecnológico a la vez que es de valor estratégico en Argentina y la región por las enormes reservas de litio.

El estudio fundamental de la reacción de electrorreducción de oxígeno en electrolitos no acuosos para el desarrollo de la tecnología de baterías de litio-aire comprendió la investigación de diversos solventes no acuosos y líquidos iónicos con sales de litio en relación a la concentración del ion litio, al solvente en mezclas de solventes y a la estabilidad de los solventes frente a los intermediarios de reacción de reducción de oxígeno. Además, se aplicó estos resultados al estudio de baterías modelo.

En cuanto a los mecanismos, se estudió las condiciones para las diferentes rutas por las cuales el oxígeno se reduce en solventes no acuosos, ya sea por superficie con formación de películas de  $\text{Li}_2\text{O}_2$  pasivantes de los cátodos de oro o por solución con estabilización del radical anión

superóxido y su dismutación favoreciendo la formación de partículas de mayor tamaño sin pasivación de la superficie.

Un estudio importante fue la solvatación preferencial del catión litio por solventes como acetonitrilo y dimetil sulfóxido debido a diferencias de su basicidad Lewis y al comportamiento frente a mezclas de solventes.

La estabilidad de solventes como el dimetil sulfóxido y el catión del líquido iónico estudiado por espectroscopia infrarroja de reflexión con control electroquímico (SNIFTIRS) mostraron inestabilidad frente al potencial en las condiciones experimentales, a la concentración de oxígeno, etc. Estos estudios fueron complementados en el laboratorio con técnicas de espectrometría de masas y espectroscopía fotoelectrónica de rayos X que resultaron en publicaciones en revistas de circulación internacional con referato que han tenido alto impacto.

El estudio de estos aspectos en baterías construidas en el laboratorio constituyen una prueba importante en un dispositivo de almacenamiento de energía.

Durante este trabajo doctoral se empleó diferentes técnicas electroquímicas, también se profundizó en el complejo manejo de soluciones no acuosas donde es crucial el control del contenido de trazas de agua y oxígeno, se han complementados los resultados con técnicas espectroscópicas y se ha demostrado una buena capacidad en el análisis crítico e interpretación de resultados en términos de modelos fisicoquímicos.

Cabe destacar que esta es la primera Tesis Doctoral en el grupo y quizás en el país sobre baterías avanzadas de litio-aire y que durante los 5 años de su ejecución la bibliografía internacional sobre el tema mostró avances significativos.

Del trabajo realizado han surgido 8 publicaciones internacionales con referato de pares y un artículo “Perspective” por invitación en el Journal of Electrochemical Society.

Todavía no está claro si la batería de Litio-aire va a convertirse en una realidad comercial, pero basados en el conocimiento adquirido, es posible resaltar las posibles direcciones de trabajo a futuro:

**1. Distinguir entre la química parásita en el ánodo y el cátodo.** La mayoría de los experimentos realizados en el campo emplearon una celda completa de Litio-aire que contiene tanto el ánodo de litio metálico como el cátodo de carbono poroso. Para una comprensión fundamental de la química parásita de la batería, es importante estudiar los componentes de la celda por separado.

**2. Seguir en la búsqueda de un solvente estable y eficiente.**

Con el conocimiento adquirido sobre los mecanismos de las reacciones de descomposición y una visión más profunda de las reacciones de ORR y OER, ahora tenemos un criterio más claro para buscar el electrolito con el mejor rendimiento. La nueva evidencia también muestra la importancia del oxígeno singlete en las reacciones de descomposición. Este aspecto no fue tomado en cuenta en esta tesis debido a su novedad; sin embargo, es imprescindible tenerlo en cuenta para dar forma a las futuras direcciones de investigación.

**3. Mediadores redox.** Los mediadores redox estables y eficientes son necesarios para reducir el sobrepotencial de recarga y mejorar la reversibilidad de la batería.

**4. Protección o sustitución del litio metálico.** La batería de Li-aire posee una densidad de energía teórica tan alta en parte debido al uso del metal litio como material de ánodo; sin embargo y hasta la fecha, el empleo del litio metálico como material del ánodo ha mostrado ser problemático, por lo tanto su protección es de suma importancia e incluso la idea de su sustitución puede ser considerada.

**5. Arquitectura del cátodo.** Mientras que la obstrucción del cátodo con peróxido de litio insoluble y aislante impide la recarga de la batería Li-aire, la arquitectura avanzada del cátodo para un encuentro eficiente entre los iones de litio, moléculas de oxígeno y electrones es muy importante.

## List of publications:

1. Calvo, E.J., Mozhzhukhina, N. A rotating ring disk electrode study of the oxygen reduction reaction in lithium containing non aqueous electrolyte (2013) *Electrochemistry Communications*, 31, pp. 56-58.
2. Mozhzhukhina, N., Méndez De Leo, L.P., Calvo, E.J. Infrared spectroscopy studies on stability of dimethyl sulfoxide for application in a Li-air battery (2013) *Journal of Physical Chemistry C*, 117 (36), pp. 18375-18380.
3. Torres, W., Mozhzhukhina, N., Tesio, A.Y., Calvo, E.J. A rotating ring disk electrode study of the oxygen reduction reaction in lithium containing dimethyl sulfoxide electrolyte: Role of superoxide (2014) *Journal of the Electrochemical Society*, 161 (14), pp. A2204-A2209.
4. Mozhzhukhina, N., Longinotti, M.P., Corti, H.R., Calvo, E.J. A conductivity study of preferential solvation of lithium ion in acetonitrile-dimethyl sulfoxide mixtures (2015) *Electrochimica Acta*, 154, pp. 456-461.
5. Mozhzhukhina, N., A. Y. Tesio, et al. (2017). "In Situ Infrared Spectroscopy Study of PYR<sub>14</sub>TFSI Ionic Liquid Stability for Li–O<sub>2</sub>Battery." *Journal of the Electrochemical Society* 164(2): A518-A523.
6. Mozhzhukhina, N., F. Marchini, et al. (2017). "Insights into dimethyl sulfoxide decomposition in Li-O<sub>2</sub> battery: Understanding carbon dioxide evolution." *Electrochemistry Communications* 80 (Supplement C): 16-19.
7. Mozhzhukhina, N. and E. J. Calvo (2017). "Perspective—The Correct Assessment of Standard Potentials of Reference Electrodes in Non-Aqueous Solution." *Journal of the Electrochemical Society* 164(12): A2295-A2297
8. Nataliia Mohzhukhina, Alvaro Y. Tesio, Maria del Pozo and Ernesto J. Calvo. Communication - Lithium Ion Concentration Effect in PYR<sub>14</sub>TFSI Ionic Liquid for Li-O<sub>2</sub> Battery Cathodes. *J. Electrochem. Soc.* 2017 volume 164, issue 8, H5277-H5279.

# References

1. K. Amine, R. Kanno, Y. Tzeng, Rechargeable lithium batteries and beyond: Progress, challenges, and future directions. *MRS Bulletin* **39**, 395 (2014).
2. P. G. Bruce, S. A. Freunberger, L. J. Hardwick, J. M. Tarascon, Li-O<sub>2</sub> and Li-S batteries with high energy storage. *Nature materials* **11**, 19 (Jan, 2012).
3. F. Cheng, J. Chen, Metal-air batteries: from oxygen reduction electrochemistry to cathode catalysts. *Chemical Society reviews* **41**, 2172 (Mar 21, 2012).
4. N. S. Choi *et al.*, Challenges facing lithium batteries and electrical double-layer capacitors. *Angew Chem Int Ed Engl* **51**, 9994 (Oct 1, 2012).
5. J. Christensen *et al.*, A Critical Review of Li/Air Batteries. *Journal of the Electrochemical Society* **159**, R1 (2012).
6. G. Girishkumar, B. McCloskey, A. C. Luntz, S. Swanson, W. Wilcke, Lithium-air battery: Promise and challenges. *Journal of Physical Chemistry Letters* **1**, 2193 (2010).
7. L. Grande *et al.*, The lithium/air battery: still an emerging system or a practical reality? *Adv Mater* **27**, 784 (Feb 4, 2015).
8. L. J. Hardwick, P. G. Bruce, The pursuit of rechargeable non-aqueous lithium–oxygen battery cathodes. *Current Opinion in Solid State and Materials Science* **16**, 178 (2012).
9. N. Imanishi, O. Yamamoto, Rechargeable lithium–air batteries: characteristics and prospects. *Materials Today* **17**, 24 (2014).
10. J. Lu *et al.*, Aprotic and aqueous Li-O(2) batteries. *Chemical reviews* **114**, 5611 (Jun 11, 2014).
11. A. C. Luntz, B. D. McCloskey, Nonaqueous Li-air batteries: a status report. *Chemical reviews* **114**, 11721 (Dec 10, 2014).
12. D. Sharon *et al.*, Lithium–Oxygen Electrochemistry in Non-Aqueous Solutions. *Israel Journal of Chemistry* **55**, 508 (2015).
13. D. Aurbach, B. D. McCloskey, L. F. Nazar, P. G. Bruce, Advances in understanding mechanisms underpinning lithium–air batteries. *Nature Energy* **1**, 16128 (2016).
14. X. Yao, Q. Dong, Q. Cheng, D. Wang, Why Do Lithium-Oxygen Batteries Fail: Parasitic Chemical Reactions and Their Synergistic Effect. *Angew Chem Int Ed Engl* **55**, 11344 (Sep 12, 2016).
15. N. Mahne, O. Fontaine, M. M. Ottakam Thotiyil, M. Wilkening, S. A. Freunberger, Mechanism and performance of lithium-oxygen batteries - a perspective. *Chemical Science*, (2017).
16. <http://www.worldometers.info/world-population/>.
17. <http://www.un.org/en/development/desa/population/>. (United Nations Population Division).
18. United States Census Bureau. (<http://www.census.gov/>).
19. <http://climate.nasa.gov/>.
20. <http://climate.nasa.gov/evidence/>.
21. <http://climate.nasa.gov/solutions/adaptation-mitigation/>.
22. Key World Energy Trends, Excerpt from : World energy balances (new release, 2016 edition). *International Energy Agency*  
<https://www.iea.org/publications/freepublications/publication/KeyWorldEnergyTrends.pdf>.
23. H. Ibrahim, A. Ilinca, J. Perron, Energy storage systems—Characteristics and comparisons. *Renewable and Sustainable Energy Reviews* **12**, 1221 (2008).
24. 1997 History of Electrochemistry calendar. *Bioanalytical Systems, Inc.*
25. B. Scrosati, CHAPTER 2. LITHIUM BATTERIES: FROM EARLY STAGES TO THE FUTURE. *in Lithium Batteries: Advanced Technologies and Applications Published 2013 by John Wiley & Sons, Inc.*

26. J.-G. Zhang, D. Wang, W. Xu, J. Xiao, R. E. Williford, Ambient operation of Li/Air batteries. *Journal of Power Sources* **195**, 4332 (2010).
27. T. Zhang, H. Zhou, A reversible long-life lithium-air battery in ambient air. *Nature communications* **4**, 1817 (2013).
28. H. K. Lim *et al.*, Toward a lithium-"air" battery: the effect of CO<sub>2</sub> on the chemistry of a lithium-oxygen cell. *Journal of the American Chemical Society* **135**, 9733 (Jul 3, 2013).
29. S. J. Visco, Nimon, Yevgeniy S. (PolyPlus Battery Company (Berkeley, CA, US), United States, 2012).
30. Y. Wang, H. Zhou, A lithium-air battery with a potential to continuously reduce O<sub>2</sub> from air for delivering energy. *Journal of Power Sources* **195**, 358 (2010).
31. K. M. Abraham, A Polymer Electrolyte-Based Rechargeable Lithium/Oxygen Battery. *Journal of the Electrochemical Society* **143**, 1 (1996).
32. J. Hassoun, F. Croce, M. Armand, B. Scrosati, Investigation of the O<sub>2</sub> electrochemistry in a polymer electrolyte solid-state cell. *Angew Chem Int Ed Engl* **50**, 2999 (Mar 21, 2011).
33. S. D. Beattie, D. M. Manolescu, S. L. Blair, High-Capacity Lithium–Air Cathodes. *Journal of The Electrochemical Society* **156**, A44 (2009).
34. B. D. McCloskey, D. S. Bethune, R. M. Shelby, G. Girishkumar, A. C. Luntz, Solvents' Critical Role in Nonaqueous Lithium–Oxygen Battery Electrochemistry. *The Journal of Physical Chemistry Letters* **2**, 1161 (2011).
35. T. Ogasawara, A. Débart, M. Holzapfel, P. Novák, P. G. Bruce, Rechargeable Li<sub>2</sub>O<sub>2</sub> Electrode for Lithium Batteries. *Journal of the American Chemical Society* **128**, 1390 (2006/02/01, 2006).
36. Z. Peng, S. A. Freunberger, Y. Chen, P. G. Bruce, A reversible and higher-rate Li-O<sub>2</sub> battery. *Science* **337**, 563 (Aug 3, 2012).
37. K. M. Abraham, in *ECS Transactions*. (2008), vol. 3, pp. 67-71.
38. J. Read, Characterization of the Lithium/Oxygen Organic Electrolyte Battery. *Journal of The Electrochemical Society* **149**, A1190 (2002).
39. J. Read *et al.*, Oxygen Transport Properties of Organic Electrolytes and Performance of Lithium/Oxygen Battery. *Journal of The Electrochemical Society* **150**, A1351 (2003).
40. J. Read, Ether-Based Electrolytes for the Lithium/Oxygen Organic Electrolyte Battery. *Journal of The Electrochemical Society* **153**, A96 (2006).
41. C. Tran, X.-Q. Yang, D. Qu, Investigation of the gas-diffusion-electrode used as lithium/air cathode in non-aqueous electrolyte and the importance of carbon material porosity. *Journal of Power Sources* **195**, 2057 (2010).
42. G. Q. Zhang *et al.*, Lithium–Air Batteries Using SWNT/CNF Buckypapers as Air Electrodes. *Journal of The Electrochemical Society* **157**, A953 (2010).
43. A. Débart, J. Bao, G. Armstrong, P. G. Bruce, An O<sub>2</sub> cathode for rechargeable lithium batteries: The effect of a catalyst. *Journal of Power Sources* **174**, 1177 (2007).
44. A. Debart, A. J. Paterson, J. Bao, P. G. Bruce, Alpha-MnO<sub>2</sub> nanowires: a catalyst for the O<sub>2</sub> electrode in rechargeable lithium batteries. *Angew Chem Int Ed Engl* **47**, 4521 (2008).
45. J. A. Read. (US, 2009), vol. US7585579 B1.
46. S. S. Zhang, D. Foster, J. Read, Discharge characteristic of a non-aqueous electrolyte Li/O<sub>2</sub> battery. *Journal of Power Sources* **195**, 1235 (2010).
47. S. A. Freunberger *et al.*, Reactions in the rechargeable lithium-O<sub>2</sub> battery with alkyl carbonate electrolytes. *Journal of the American Chemical Society* **133**, 8040 (May 25, 2011).
48. C. O. Laoire, S. Mukerjee, E. J. Plichta, M. A. Hendrickson, K. M. Abraham, Rechargeable Lithium/TEGDME-LiPF<sub>6</sub>/O<sub>2</sub> Battery. *Journal of The Electrochemical Society* **158**, A302 (2011).

49. W. Xu *et al.*, The stability of organic solvents and carbon electrode in nonaqueous Li-O<sub>2</sub> batteries. *Journal of Power Sources* **215**, 240 (2012).
50. H.-G. Jung, J. Hassoun, J.-B. Park, Y.-K. Sun, B. Scrosati, An improved high-performance lithium-air battery. *Nat Chem* **4**, 579 (2012).
51. D. Sharon *et al.*, On the Challenge of Electrolyte Solutions for Li-Air Batteries: Monitoring Oxygen Reduction and Related Reactions in Polyether Solutions by Spectroscopy and EQCM. *J Phys Chem Lett* **4**, 127 (Jan 3, 2013).
52. B. D. Adams *et al.*, Towards a Stable Organic Electrolyte for the Lithium Oxygen Battery. *Advanced Energy Materials* **5**, n/a (2015).
53. M. J. Trahan, S. Mukerjee, E. J. Plichta, M. A. Hendrickson, K. M. Abraham, Studies of Li-Air Cells Utilizing Dimethyl Sulfoxide-Based Electrolyte. *Journal of the Electrochemical Society* **160**, A259 (2012).
54. D. Sharon *et al.*, Oxidation of Dimethyl Sulfoxide Solutions by Electrochemical Reduction of Oxygen. *J Phys Chem Lett* **4**, 3115 (2013).
55. D. G. Kwabi *et al.*, Chemical Instability of Dimethyl Sulfoxide in Lithium-Air Batteries. *J Phys Chem Lett* **5**, 2850 (Aug 21, 2014).
56. M. A. Schroeder *et al.*, DMSO-Li<sub>2</sub>O<sub>2</sub> Interface in the Rechargeable Li-O<sub>2</sub> Battery Cathode: Theoretical and Experimental Perspectives on Stability. *ACS applied materials & interfaces* **7**, 11402 (Jun 3, 2015).
57. N. Mozhzhukhina, L. P. Méndez De Leo, E. J. Calvo, Infrared Spectroscopy Studies on Stability of Dimethyl Sulfoxide for Application in a Li-Air Battery. *The Journal of Physical Chemistry C* **117**, 18375 (2013).
58. E. J. Calvo, N. Mozhzhukhina, A rotating ring disk electrode study of the oxygen reduction reaction in lithium containing non aqueous electrolyte. *Electrochemistry Communications* **31**, 56 (2013).
59. W. Torres, N. Mozhzhukhina, A. Y. Tesio, E. J. Calvo, A Rotating Ring Disk Electrode Study of the Oxygen Reduction Reaction in Lithium Containing Dimethyl Sulfoxide Electrolyte: Role of Superoxide. *Journal of the Electrochemical Society* **161**, A2204 (2014).
60. M. Kar, T. J. Simons, M. Forsyth, D. R. MacFarlane, Ionic liquid electrolytes as a platform for rechargeable metal-air batteries: a perspective. *Physical Chemistry Chemical Physics* **16**, 18658 (2014).
61. D. R. MacFarlane *et al.*, Ionic liquids and their solid-state analogues as materials for energy generation and storage. *Nature Reviews Materials* **1**, 15005 (2016).
62. V. S. Bryantsev *et al.*, Investigation of Fluorinated Amides for Solid-Electrolyte Interphase Stabilization in Li-O<sub>2</sub>Batteries Using Amide-Based Electrolytes. *The Journal of Physical Chemistry C* **117**, 11977 (2013).
63. V. Giordani *et al.*, N-methylacetamide as an Electrolyte Solvent for Rechargeable Li-O<sub>2</sub> Batteries: Unexpected Stability at the O<sub>2</sub> electrode. *ECS Electrochemistry Letters* **3**, A11 (2013).
64. V. Giordani, J. Uddin, V. S. Bryantsev, G. V. Chase, D. Addison, High Concentration Lithium Nitrate/Dimethylacetamide Electrolytes for Lithium/Oxygen Cells. *Journal of the Electrochemical Society* **163**, A2673 (2016).
65. W. Walker *et al.*, A rechargeable Li-O<sub>2</sub> battery using a lithium nitrate/N,N-dimethylacetamide electrolyte. *Journal of the American Chemical Society* **135**, 2076 (Feb 13, 2013).
66. B. D. McCloskey *et al.*, Twin Problems of Interfacial Carbonate Formation in Nonaqueous Li-O<sub>2</sub> Batteries. *J Phys Chem Lett* **3**, 997 (Apr 19, 2012).
67. B. D. McCloskey, C. M. Burke, J. E. Nichols, S. E. Renfrew, Mechanistic insights for the development of Li-O<sub>2</sub> battery materials: addressing Li<sub>2</sub>O<sub>2</sub> conductivity limitations and electrolyte and cathode instabilities. *Chemical Communications* **51**, 12701 (2015).

68. Z. Ma *et al.*, A review of cathode materials and structures for rechargeable lithium-air batteries. *Energy and Environmental Science* **8**, 2144 (2015).
69. B. D. McCloskey *et al.*, On the efficacy of electrocatalysis in nonaqueous Li-O<sub>2</sub> batteries. *Journal of the American Chemical Society* **133**, 18038 (Nov 16, 2011).
70. V. Giordani *et al.*, Synergistic Effect of Oxygen and LiNO<sub>3</sub> on the Interfacial Stability of Lithium Metal in a Li/O<sub>2</sub> Battery. *Journal of the Electrochemical Society* **160**, A1544 (2013).
71. J. Uddin *et al.*, Lithium Nitrate As Regenerable SEI Stabilizing Agent for Rechargeable Li/O<sub>2</sub>Batteries. *The Journal of Physical Chemistry Letters* **4**, 3760 (2013).
72. S. Meini, M. Piana, N. Tsiouvaras, A. Garsuch, H. A. Gasteiger, The Effect of Water on the Discharge Capacity of a Non-Catalyzed Carbon Cathode for Li-O<sub>2</sub> Batteries. *Electrochemical and Solid-State Letters* **15**, A45 (2012).
73. N. B. Aetukuri *et al.*, Solvating additives drive solution-mediated electrochemistry and enhance toroid growth in non-aqueous Li-O(2) batteries. *Nat Chem* **7**, 50 (Jan, 2015).
74. G. V. Chase *et al.* (Google Patents, 2012).
75. Y. Chen, S. A. Freunberger, Z. Peng, O. Fontaine, P. G. Bruce, Charging a Li-O<sub>2</sub> battery using a redox mediator. *Nat Chem* **5**, 489 (2013).
76. M. J. Lacey, J. T. Frith, J. R. Owen, A redox shuttle to facilitate oxygen reduction in the lithium air battery. *Electrochemistry Communications* **26**, 74 (2013).
77. S. Schaltin, G. Vanhoutte, M. Wu, F. Barde, J. Fransaer, A QCM study of ORR-OER and an in situ study of a redox mediator in DMSO for Li-O<sub>2</sub> batteries. *Physical chemistry chemical physics : PCCP* **17**, 12575 (May 21, 2015).
78. W. R. Torres, S. E. Herrera, A. Y. Tesio, M. d. Pozo, E. J. Calvo, Soluble TTF catalyst for the oxidation of cathode products in Li-Oxygen battery: A chemical scavenger. *Electrochimica Acta* **182**, 1118 (2015).
79. D. Kundu, R. Black, B. Adams, L. F. Nazar, A Highly Active Low Voltage Redox Mediator for Enhanced Rechargeability of Lithium-Oxygen Batteries. *ACS Central Science* **1**, 510 (2015/12/23, 2015).
80. B. J. Bergner, A. Schürmann, K. Peppler, A. Garsuch, J. Janek, TEMPO: A Mobile Catalyst for Rechargeable Li-O<sub>2</sub> Batteries. *Journal of the American Chemical Society* **136**, 15054 (2014/10/22, 2014).
81. W.-J. Kwak *et al.*, Understanding the behavior of Li-oxygen cells containing LiI. *Journal of Materials Chemistry A* **3**, 8855 (2015).
82. C. K. Lee, Y. J. Park, CsI as Multifunctional Redox Mediator for Enhanced Li-Air Batteries. *ACS applied materials & interfaces* **8**, 8561 (2016/04/06, 2016).
83. H.-D. Lim *et al.*, Rational design of redox mediators for advanced Li-O<sub>2</sub> batteries. *Nature Energy* **1**, 16066 (2016).
84. N. Mozhzhukhina, M. P. Longinotti, H. R. Corti, E. J. Calvo, A conductivity study of preferential solvation of lithium ion in acetonitrile-dimethyl sulfoxide mixtures. *Electrochimica Acta* **154**, 456 (2015).
85. C. O. Laoire, S. Mukerjee, K. M. Abraham, E. J. Plichta, M. A. Hendrickson, Elucidating the Mechanism of Oxygen Reduction for Lithium-Air Battery Applications. *The Journal of Physical Chemistry C* **113**, 20127 (2009/11/19, 2009).
86. C. O. Laoire, S. Mukerjee, K. M. Abraham, E. J. Plichta, M. A. Hendrickson, Influence of Nonaqueous Solvents on the Electrochemistry of Oxygen in the Rechargeable Lithium-Air Battery. *The Journal of Physical Chemistry C* **114**, 9178 (2010/05/20, 2010).
87. C. J. Allen, S. Mukerjee, E. J. Plichta, M. A. Hendrickson, K. M. Abraham, Oxygen Electrode Rechargeability in an Ionic Liquid for the Li-Air Battery. *The Journal of Physical Chemistry Letters* **2**, 2420 (2011).

88. C. J. Bondue, A. A. Abd-El-Latif, P. Hegemann, H. Baltruschat, Quantitative study for oxygen reduction and evolution in aprotic organic electrolytes at gas diffusion electrodes by DEMS. *Journal of the Electrochemical Society* **162**, A479 (2015).
89. C. J. Bondue, P. Reinsberg, A. A. Abd-El-Latif, H. Baltruschat, Oxygen reduction and oxygen evolution in DMSO based electrolytes: The role of the electrocatalyst. *Physical Chemistry Chemical Physics* **17**, 25593 (2015).
90. L. Johnson *et al.*, The role of LiO<sub>2</sub> solubility in O<sub>2</sub> reduction in aprotic solvents and its consequences for Li-O<sub>2</sub> batteries. *Nature Chemistry* **6**, 1091 (2014).
91. K. U. Schwenke, J. Herranz, H. A. Gasteiger, M. Piana, Reactivity of the ionic liquid Pyr<sup>+</sup><sub>14</sub>TFSI with superoxide radicals generated from KO<sup>-</sup><sub>2</sub> or by contact of O<sup>-</sup><sub>2</sub> with Li<sup>+</sup><sub>7</sub>Ti<sup>5</sup>O<sup>-</sup><sub>12</sub>. *Journal of the Electrochemical Society* **162**, A905 (2015).
92. D. L. Goldfarb, M. P. Longinotti, H. R. Corti, Electrical Conductances of Tetrabutylammonium and Decamethylferrocenium Hexafluorophosphate in Organic Solvents. *Journal of Solution Chemistry* **30**, 307 (2001).
93. J. Barthel, L. Iberl, J. Rossmair, H. J. Gores, B. Kaukal, Conductance of 1,1-electrolytes in acetonitrile solutions from -40° to 35°C. *Journal of Solution Chemistry* **19**, 321 (1990).
94. M. N. Roy, R. Chanda, P. Chakraborti, A. Das, Conductivity is a contrivance to explore ion-pair and triple-ion structure of ethanoates in tetrahydrofuran, dimethyl sulfoxide and their binaries. *Fluid Phase Equilibria* **322–323**, 159 (2012).
95. J. H. Exner, E. C. Steiner, Solvation and ion pairing of alkali-metal alkoxides in dimethyl sulfoxide. Conductometric studies. *Journal of the American Chemical Society* **96**, 1782 (1974/03/01, 1974).
96. M. D. Archer, R. P. H. Gasser, Electrolyte solutions in dimethyl sulphoxide. Part 2.-Caesium iodide. *Transactions of the Faraday Society* **62**, 3451 (1966).
97. M. H. J. W. Albery, Rotating Ring Disc Electrodes. *Oxford University Press, Oxford*, (1971).
98. C. J. Allen *et al.*, Oxygen Reduction Reactions in Ionic Liquids and the Formulation of a General ORR Mechanism for Li-Air Batteries. *The Journal of Physical Chemistry C* **116**, 20755 (2012).
99. T. Iwasita, F. C. Nart, In situ infrared spectroscopy at electrochemical interfaces. *Progress in Surface Science* **55**, 271 (1997).
100. M. d. C. Grande, M. García, C. M. Marschoff, Density and Viscosity of Anhydrous Mixtures of Dimethylsulfoxide with Acetonitrile in the Range (298.15 to 318.15) K. *Journal of Chemical & Engineering Data* **54**, 652 (2009/02/12, 2009).
101. D. S. Gill, D. S. Rana, S. P. Jauhar, Transport Studies of Some 1:1 Copper(I) Perchlorate Complexes in Acetonitrile-Dimethylsulphoxide Mixtures. *Zeitschrift für Physikalische Chemie* **225**, 69 (2011).
102. Y. C. Wu, W. F. Koch, W. J. Hamer, R. L. Kay, Review of electrolytic conductance standards. *Journal of Solution Chemistry* **16**, 985 (1987//, 1987).
103. M. S. R. Fernandez Prini, Conductance and transference numbers in organic solvents. *in: A.K. Covington, T. Dickinson (Eds.), Physical Chemistry of Organic Solvents Systems, Part 3, Chapter 5, Plenum Press, New York, , (1973).*
104. G. Z. Sauerbrey, *Z. Phys.* **155**, 206 (1959).
105. M. Piana *et al.*, Stability of a Pyrrolidinium-Based Ionic Liquid in Li-O<sub>2</sub> Cells. *Journal of the Electrochemical Society* **161**, A1992 (2014).
106. G. A. Elia *et al.*, An advanced lithium-air battery exploiting an ionic liquid-based electrolyte. *Nano letters* **14**, 6572 (Nov 12, 2014).
107. R. S. Assary *et al.*, The effect of oxygen crossover on the anode of a Li-O(2) battery using an ether-based solvent: insights from experimental and computational studies. *ChemSusChem* **6**, 51 (Jan, 2013).

108. J. L. Shui *et al.*, Reversibility of anodic lithium in rechargeable lithium-oxygen batteries. *Nature communications* **4**, 2255 (2013).
109. G. Zheng *et al.*, Interconnected hollow carbon nanospheres for stable lithium metal anodes. *Nat Nano* **9**, 618 (2014).
110. W.-J. Kwak, H.-G. Jung, D. Aurbach, Y.-K. Sun, Optimized Bicompartement Two Solution Cells for Effective and Stable Operation of Li-O<sub>2</sub> Batteries. *Advanced Energy Materials*, 1701232 (2017).
111. D. Hirshberg *et al.*, Feasibility of Full (Li-Ion)-O<sub>2</sub> Cells Comprised of Hard Carbon Anodes. *ACS applied materials & interfaces* **9**, 4352 (Feb 08, 2017).
112. K. U. Schwenke, J. Herranz, H. A. Gasteiger, M. Piana, Reactivity of the Ionic Liquid Pyr14TFSI with Superoxide Radicals Generated from KO<sub>2</sub> or by Contact of O<sub>2</sub> with Li<sub>7</sub>Ti<sub>5</sub>O<sub>12</sub>. *Journal of the Electrochemical Society* **162**, A905 (2015).
113. E. Ferg, R. J. Gummow, A. de Kock, M. M. Thackeray, Spinel Anodes for Lithium-Ion Batteries. *Journal of the Electrochemical Society* **141**, L147 (November 1, 1994, 1994).
114. T. Ohzuku, Zero-Strain Insertion Material of Li[Li<sub>1/3</sub>Ti<sub>5/3</sub>]O<sub>4</sub> for Rechargeable Lithium Cells. *Journal of the Electrochemical Society* **142**, 1431 (1995).
115. A. N. Jansen *et al.*, Development of a high-power lithium-ion battery. *Journal of Power Sources* **81**, 902 (1999/09/01/, 1999).
116. J. Christensen, V. Srinivasan, J. Newman, Optimization of Lithium Titanate Electrodes for High-Power Cells. *Journal of the Electrochemical Society* **153**, A560 (2006).
117. V. Borgel, G. Gershinshy, T. Hu, M. G. Theivanayagam, D. Aurbach, LiMn<sub>0.8</sub>Fe<sub>0.2</sub>PO<sub>4</sub>/Li<sub>4</sub>Ti<sub>5</sub>O<sub>12</sub>, a Possible Li-Ion Battery System for Load-Leveling Application. *Journal of the Electrochemical Society* **160**, A650 (2013).
118. S. Chauque *et al.*, Lithium titanate as anode material for lithium ion batteries: Synthesis, post-treatment and its electrochemical response. *Journal of Electroanalytical Chemistry* **799**, 142 (2017).
119. T. Nordh, R. Younesi, D. Brandell, K. Edström, Depth profiling the solid electrolyte interphase on lithium titanate (Li<sub>4</sub>Ti<sub>5</sub>O<sub>12</sub>) using synchrotron-based photoelectron spectroscopy. *Journal of Power Sources* **294**, 173 (2015).
120. E. Markevich *et al.*, In situ FTIR study of the decomposition of N-butyl-N-methylpyrrolidinium bis(trifluoromethanesulfonyl)amide ionic liquid during cathodic polarization of lithium and graphite electrodes. *Electrochimica Acta* **55**, 2687 (2010).
121. L. Grande, E. Paillard, G. T. Kim, S. Monaco, S. Passerini, Ionic liquid electrolytes for Li-air batteries: lithium metal cycling. *International journal of molecular sciences* **15**, 8122 (May 08, 2014).
122. D. T. Sawyer, G. Chiericato, C. T. Angelis, E. J. Nanni, T. Tsuchiya, Effects of media and electrode materials on the electrochemical reduction of dioxygen. *Analytical Chemistry* **54**, 1720 (1982/09/01, 1982).
123. L. Johnson *et al.*, The role of LiO<sub>2</sub> solubility in O<sub>2</sub> reduction in aprotic solvents and its consequences for Li-O<sub>2</sub> batteries. *Nat Chem* **6**, 1091 (2014).
124. B. D. McCloskey, D. S. Bethune, R. M. Shelby, G. Girishkumar, A. C. Luntz, Solvents critical role in nonaqueous Lithium-Oxygen battery electrochemistry. *Journal of Physical Chemistry Letters* **2**, 1161.
125. B. D. McCloskey, R. Scheffler, A. Speidel, G. Girishkumar, A. C. Luntz, On the Mechanism of Nonaqueous Li-O<sub>2</sub> Electrochemistry on C and Its Kinetic Overpotentials: Some Implications for Li-Air Batteries. *The Journal of Physical Chemistry C* **116**, 23897 (2012).
126. A. J. Bard, L. R. Faulkner, *Electrochemical Methods: Fundamentals and Applications*, (1980).

127. E. J. Calvo, International Symposium on Lithium Air Batteries. *Buenos Aires*, (2012).
128. Y. Katayama, H. Onodera, M. Yamagata, T. Miura, Electrochemical reduction of oxygen in some hydrophobic room-temperature molten salt systems. *Journal of the Electrochemical Society* **151**, (2004).
129. Y. Katayama, K. Sekiguchi, M. Yamagata, T. Miura, Electrochemical behavior of oxygen/superoxide ion couple in 1-butyl-1-methylpyrrolidinium bis(trifluoromethylsulfonyl)imide room-temperature molten salt. *Journal of the Electrochemical Society* **152**, (2005).
130. C. Pozo-Gonzalo, P. C. Howlett, D. R. MacFarlane, M. Forsyth, Highly reversible oxygen to superoxide redox reaction in a sodium-containing ionic liquid. *Electrochemistry Communications* **74**, 14 (2017).
131. Y. Katayama, K. Sekiguchi, M. Yamagata, T. Miura, Electrochemical behavior of oxygen/superoxide ion couple in 1-butyl-1-methylpyrrolidinium bis(trifluoromethylsulfonyl)imide room-temperature molten salt. *Journal of the Electrochemical Society* **152**, E247 (2005).
132. I. M. AlNashef, M. L. Leonard, M. A. Matthews, J. W. Weidner, Superoxide electrochemistry in an ionic liquid. *Industrial and Engineering Chemistry Research* **41**, 4475 (2002).
133. M. T. Carter, C. L. Hussey, S. K. D. Strubinger, R. A. Osteryoung, Electrochemical reduction of dioxygen in room-temperature imidazolium chloride-aluminum chloride molten salts. *Inorganic Chemistry* **30**, 1149 (1991).
134. X. J. Huang, E. I. Rogers, C. Hardacre, R. G. Compton, The reduction of oxygen in various room temperature ionic liquids in the temperature range 293-318 K: Exploring the applicability of the Stokes-Einstein relationship in room temperature ionic liquids. *Journal of Physical Chemistry B* **113**, 8953 (2009).
135. R. G. Evans, O. V. Klymenko, S. A. Saddoughi, C. Hardacre, R. G. Compton, Electroreduction of oxygen in a series of room temperature ionic liquids composed of group 15-centered cations and anions. *Journal of Physical Chemistry B* **108**, 7878 (2004).
136. Y. Katayama, H. Onodera, M. Yamagata, T. Miura, Electrochemical reduction of oxygen in some hydrophobic room-temperature molten salt systems. *Journal of the Electrochemical Society* **151**, A59 (2004).
137. S. Monaco *et al.*, An electrochemical study of oxygen reduction in pyrrolidinium-based ionic liquids for lithium/oxygen batteries. *Electrochimica Acta* **83**, 94 (2012).
138. F. De Giorgio, F. Soavi, M. Mastragostino, Effect of lithium ions on oxygen reduction in ionic liquid-based electrolytes. *Electrochemistry Communications* **13**, 1090 (2011).
139. A. W. Lodge, M. J. Lacey, M. Fitt, N. Garcia-Araez, J. R. Owen, Critical appraisal on the role of catalysts for the oxygen reduction reaction in lithium-oxygen batteries. *Electrochimica Acta* **140**, 168 (2014).
140. J. Herranz, A. Garsuch, H. A. Gasteiger, Using Rotating Ring Disc Electrode Voltammetry to Quantify the Superoxide Radical Stability of Aprotic Li-Air Battery Electrolytes. *The Journal of Physical Chemistry C* **116**, 19084 (2012).
141. D. G. Kwabi *et al.*, Experimental and Computational Analysis of the Solvent-Dependent  $O_2/Li-O_2$  Redox Couple: Standard Potentials, Coupling Strength, and Implications for Lithium-Oxygen Batteries. *Angewandte Chemie - International Edition* **55**, 3129 (2016).
142. J. T. Frith, A. E. Russell, N. Garcia-Araez, J. R. Owen, An in-situ Raman study of the oxygen reduction reaction in ionic liquids. *Electrochemistry Communications* **46**, 33 (2014).
143. F. Soavi, S. Monaco, M. Mastragostino, Catalyst-free porous carbon cathode and ionic liquid for high efficiency, rechargeable Li/O<sub>2</sub> battery. *Journal of Power Sources* **224**, 115 (2013).

144. N. Mozhzhukhina, A. Y. Tesio, M. D. L. , L. , , E. J. Calvo, In Situ Infrared Spectroscopy Study of PYR14TFSI Ionic Liquid Stability for Li–O<sub>2</sub> Battery. *Journal of The Electrochemical Society* **164**, A518 (2017).
145. D. G. Kwabi *et al.*, Experimental and Computational Analysis of the Solvent-Dependent O<sub>2</sub>/Li(+)-O<sub>2</sub>(-) Redox Couple: Standard Potentials, Coupling Strength, and Implications for Lithium-Oxygen Batteries. *Angew Chem Int Ed Engl* **55**, 3129 (Feb 24, 2016).
146. C. M. Burke, V. Pande, A. Khetan, V. Viswanathan, B. D. McCloskey, Enhancing electrochemical intermediate solvation through electrolyte anion selection to increase nonaqueous Li-O<sub>2</sub> battery capacity. *Proceedings of the National Academy of Sciences of the United States of America* **112**, 9293 (Jul 28, 2015).
147. D. Sharon *et al.*, Mechanistic Role of Li(+) Dissociation Level in Aprotic Li-O(2) Battery. *ACS applied materials & interfaces* **8**, 5300 (Mar 02, 2016).
148. I. Gunasekara, S. Mukerjee, E. J. Plichta, M. A. Hendrickson, K. M. Abraham, A Study of the Influence of Lithium Salt Anions on Oxygen Reduction Reactions in Li-Air Batteries. *Journal of the Electrochemical Society* **162**, A1055 (2015).
149. X. Gao, Y. Chen, L. Johnson, P. G. Bruce, Promoting solution phase discharge in Li-O<sub>2</sub> batteries containing weakly solvating electrolyte solutions. *Nature materials* **15**, 882 (2016).
150. B. D. Adams *et al.*, Current density dependence of peroxide formation in the Li–O<sub>2</sub> battery and its effect on charge. *Energy & Environmental Science* **6**, 1772 (2013).
151. B. Horstmann *et al.*, Rate-Dependent Morphology of Li<sub>2</sub>O<sub>2</sub> Growth in Li-O<sub>2</sub> Batteries. *J Phys Chem Lett* **4**, 4217 (Dec 19, 2013).
152. N. Mozhzhukhina, E. J. Calvo, Perspective—The Correct Assessment of Standard Potentials of Reference Electrodes in Non-Aqueous Solution. *Journal of the Electrochemical Society* **164**, A2295 (2017).
153. G. Gritzner, J. Kůta, Recommendations on reporting electrode potentials in nonaqueous solvents. *Electrochimica Acta* **29**, 869 (1984/06/01, 1984).
154. R. Semino, G. Zaldivar, E. J. Calvo, D. Laria, Lithium solvation in dimethyl sulfoxide-acetonitrile mixtures. *The Journal of chemical physics* **141**, 214509 (Dec 07, 2014).
155. R. Semino, G. Zaldivar, E. J. Calvo, D. Laria, Lithium solvation in dimethyl sulfoxide-acetonitrile mixtures. *Journal of Chemical Physics* **141**, (2014).
156. K. Xu, Nonaqueous liquid electrolytes for lithium-based rechargeable batteries. *Chemical reviews* **104**, 4303 (2004).
157. H. Han *et al.*, Lithium (fluorosulfonyl)(nonafluorobutanesulfonyl)imide (LiFNFSI) as conducting salt to improve the high-temperature resilience of lithium-ion cells. *Electrochemistry Communications* **13**, 265 (2011).
158. H. B. Han *et al.*, Lithium bis(fluorosulfonyl)imide (LiFSI) as conducting salt for nonaqueous liquid electrolytes for lithium-ion batteries: Physicochemical and electrochemical properties. *Journal of Power Sources* **196**, 3623 (2011).
159. S. A. Freunberger *et al.*, The lithium-oxygen battery with ether-based electrolytes. *Angew Chem Int Ed Engl* **50**, 8609 (Sep 5, 2011).
160. Z. Peng *et al.*, Oxygen reactions in a non-aqueous Li<sup>+</sup> electrolyte. *Angewandte Chemie - International Edition* **50**, 6351 (2011).
161. H. Wang, K. Xie, Investigation of oxygen reduction chemistry in ether and carbonate based electrolytes for Li–O<sub>2</sub> batteries. *Electrochimica Acta* **64**, 29 (2012).
162. W. Xu *et al.*, Reaction mechanisms for the limited reversibility of Li–O<sub>2</sub> chemistry in organic carbonate electrolytes. *Journal of Power Sources* **196**, 9631 (2011).

163. R. Younesi, M. Hahlin, K. Edström, Surface characterization of the carbon cathode and the lithium anode of Li-O<sub>2</sub> batteries using LiClO<sub>4</sub> or LiBOB salts. *ACS Applied Materials and Interfaces* **5**, 1333 (2013).
164. C. J. Barile, A. A. Gewirth, Investigating the Li-O<sub>2</sub> battery in an ether-based electrolyte using differential electrochemical mass spectrometry. *Journal of the Electrochemical Society* **160**, A549 (2013).
165. R. Fernandez Prini, M. Spiro, Conductance and transference numbers in organic solvents. *Physical Chemistry of Organic Solvents Systems, Part 3, Chapter 5*, (1973).
166. N. G. Tsierkezos, A. I. Philippopoulos, Studies of ion solvation and ion association of n-tetrabutylammonium hexafluorophosphate and n-tetrabutylammonium tetraphenylborate in various solvents. *Fluid Phase Equilibria* **277**, 20 (2009).
167. R. Zwanzig, Dielectric friction on a moving ion. II. Revised theory. *The Journal of chemical physics* **52**, 3625 (1970).
168. J. Hubbard, L. Onsager, Dielectric dispersion and dielectric friction in electrolyte solutions. I. *The Journal of chemical physics* **67**, 4850 (1977).
169. P. G. Wolynes, Dynamics of electrolyte solutions. *Annu. Rev. Phys. Chem.* **31**, 345 (1980).
170. D. Vasudevan, H. Wendt, Electroreduction of oxygen in aprotic media. *J Electroanal Chem* **392**, 69 (1995).
171. Q. Li, C. Batchelor-McAuley, N. S. Lawrence, R. S. Hartshorne, R. G. Compton, Anomalous solubility of oxygen in acetonitrile/water mixture containing tetra-n-butylammonium perchlorate supporting electrolyte; the solubility and diffusion coefficient of oxygen in anhydrous acetonitrile and aqueous mixtures. *Journal of Electroanalytical Chemistry* **688**, 328 (2013).
172. J. D. Wadhawan, P. J. Welford, H. B. McPeak, C. E. W. Hahn, R. G. Compton, The simultaneous voltammetric determination and detection of oxygen and carbon dioxide: A study of the kinetics of the reaction between superoxide and carbon dioxide in non-aqueous media using membrane-free gold disc microelectrodes. *Sensors and Actuators B: Chemical* **88**, 40 (2003/01/01/, 2003).
173. A. D. Goolsby, The electrochemical reduction of superoxide ion and oxidation of hydroxide ion in dimethyl sulfoxide. *Analytical Chemistry* **40**, 83 (1968).
174. I. Gunasekara, S. Mukerjee, E. J. Plichta, M. A. Hendrickson, K. M. Abraham, Microelectrode Diagnostics of Lithium-Air Batteries. *Journal of the Electrochemical Society* **161**, A381 (2014).
175. I. P. Vladimir Tanasković, Slavko Mentus, Polycrystalline Platinum Rotating Disc Electrode Study of the Liquid System 0.2 M LiClO<sub>4</sub> -H<sub>2</sub>O-DMSO in Nitrogen and Oxygen Atmosphere. *International Journal of Electrochemical Science* **8**, 6243 (2013).
176. C. M. Collins, C. Sotiriou-Leventis, M. T. Canalias, N. Leventis, A cyclic voltammetric study of the proton abstraction from selected aromatic ketones by superoxide. *Electrochimica Acta* **45**, 2049 (2000/03/01/, 2000).
177. Y. Wang, E. I. Rogers, R. G. Compton, The measurement of the diffusion coefficients of ferrocene and ferrocenium and their temperature dependence in acetonitrile using double potential step microdisk electrode chronoamperometry. *Journal of Electroanalytical Chemistry* **648**, 15 (2010).
178. D. Shoup, A. Szabo, Chronoamperometric current at finite disk electrodes. *Journal of Electroanalytical Chemistry and Interfacial Electrochemistry* **140**, 237 (1982/11/23/, 1982).
179. D. Xu, Z. L. Wang, J. J. Xu, L. L. Zhang, X. B. Zhang, Novel DMSO-based electrolyte for high performance rechargeable Li-O<sub>2</sub> batteries. *Chem Commun (Camb)* **48**, 6948 (Jul 14, 2012).
180. A. D. Goolsby, D. T. Sawyer, Electrochemical reduction of superoxide ion and oxidation of hydroxide ion in dimethyl sulfoxide. *Analytical Chemistry* **40**, 83 (1968/01/01, 1968).
181. H. Gampp, S. J. Lippard, Reinvestigation of 18-crown-6 ether/potassium superoxide solutions in Me<sub>2</sub>SO. *Inorganic Chemistry* **22**, 357 (1983/01/01, 1983).

182. P. Krtil, L. Kavan, I. Hoskovicová, K. Kratochvilová, Anodic oxidation of dimethyl sulfoxide based electrolyte solutions: An in situ FTIR study. *Journal of Applied Electrochemistry* **26**, 523 (1996//, 1996).
183. L. J. Bellamy, *The Infrared Spectra of Complex Molecules*, (1975).
184. D. Lin-Vien, N. B. Colthup, W. G. Fateley, J. G. Grasselli, *The Handbook of Infrared and Raman Characteristic Frequencies of Organic Molecules*, (1991).
185. NIST Chemistry WebBook: NIST Standard Reference Database Number 69. **National Institute of Standards and Technology** <http://webbook.nist.gov/chemistry/>.
186. Z. Peng *et al.*, Oxygen reactions in a non-aqueous Li<sup>+</sup> electrolyte. *Angew Chem Int Ed Engl* **50**, 6351 (Jul 4, 2011).
187. F. Marchini *et al.*, Surface Study of Lithium-Air Battery Oxygen Cathodes in Different Solvent-Electrolyte pairs. *Langmuir : the ACS journal of surfaces and colloids* **31**, 9236 (Aug 25, 2015).
188. N. Mozzhukhina *et al.*, Insights into dimethyl sulfoxide decomposition in Li-O<sub>2</sub> battery: Understanding carbon dioxide evolution. *Electrochemistry Communications* **80**, 16 (2017/07/01/, 2017).
189. R. Younesi, P. Norby, T. Vegge, A New Look at the Stability of Dimethyl Sulfoxide and Acetonitrile in Li-O<sub>2</sub> Batteries. *ECS Electrochemistry Letters* **3**, A15 (2014).
190. T. Kuboki, T. Okuyama, T. Ohsaki, N. Takami, Lithium-air batteries using hydrophobic room temperature ionic liquid electrolyte. *Journal of Power Sources* **146**, 766 (2005).
191. P. C. Howlett, N. Brack, A. F. Hollenkamp, M. Forsyth, D. R. MacFarlane, Characterization of the Lithium Surface in N-Methyl-N-alkylpyrrolidinium Bis(trifluoromethanesulfonyl)amide Room-Temperature Ionic Liquid Electrolytes. *Journal of the Electrochemical Society* **153**, A595 (2006).
192. K. Hanke *et al.*, Understanding the ionic liquid [NC4111][NTf<sub>2</sub>] from individual building blocks: an IR-spectroscopic study. *Physical Chemistry Chemical Physics* **17**, 8518 (2015).
193. A. Lahiri, N. Borisenko, A. Borodin, M. Olschewski, F. Endres, Characterisation of the solid electrolyte interface during lithiation/delithiation of germanium in an ionic liquid. *Physical Chemistry Chemical Physics* **18**, 5630 (2016).
194. D. Lin-Vien, Colthup, N.B., Fateley, W.G., Grasselli, J.G, in *Academic Press, Inc. San Diego, CA*. (1991).
195. I. Rey *et al.*, Spectroscopic and Theoretical Study of (CF<sub>3</sub>SO<sub>2</sub>)<sub>2</sub>N<sup>-</sup> (TFSI<sup>-</sup>) and (CF<sub>3</sub>SO<sub>2</sub>)<sub>2</sub>NH<sup>+</sup> (HTFSI). *The Journal of Physical Chemistry A* **102**, 3249 (1998/05/01, 1998).
196. O. Cheung, Z. Bacsik, Q. Liu, A. Mace, N. Hedin, Adsorption kinetics for CO<sub>2</sub> on highly selective zeolites NaKA and nano-NaKA. *Applied Energy* **112**, 1326 (2013).
197. F. Nart, T. Iwasita, in *Encyclopedia of Electrochemistry* Wiley-VCH, Ed. (2007).